MICROSTRUCTURE-MECHANICAL PROPERTY RELATIONSHIPS IN CARBON NANOFIBERS

A Dissertation

by

SNEHA ANIL CHAWLA

Submitted to the Office of Graduate and Professional Studies of
Texas A&M University
in partial fulfillment of the requirements for the degree of

DOCTOR OF PHILOSOPHY

Chair of Committee,	Mohammad Naraghi
Committee Members,	Amine Benzerga
	James Boyd
	Lin Shao
	Ramesh Talreja
Head of Department,	Ibrahim Karaman

May 2017

Major Subject: Material Science and Engineering

ABSTRACT

Carbon nanofibers, though radially more homogeneous compared to carbon fibers, currently do not possess mechanical properties as high as carbon fibers. By principles of size effect, carbon nanofibers are expected to possess considerably higher strengths than carbon fibers. Theoretically, CNFs are expected to have strengths as high as 14GPa. However, at present, CNFs possess strengths much lower than expected. The gap in theoretical and experimental work points to three main reasons: graphitic alignment in the nanofiber, radial structure of the nanofiber and presence of surface defects. The work presented in this dissertation aims at closing the gap via relating the microstructure and mechanical properties of carbon nanofibers. Graphitic alignment in carbon nanofibers imparts high modulus and strength to the fibers. This alignment of graphitic domains arises from the induced molecular alignment in precursor fiber. The precursor is polyacrylonitrile (PAN) fiber obtained from electrospinning of PAN in Dimethylformamide (DMF) solution. Limited molecular alignment is achievable with electrospinning, which creates the need to use other methods to improve molecular alignment. The research uses a method for hot drawing, which takes place at temperatures above the T_g of the polymer. The temperature aids chain mobility in the fiber, allowing it to stretch. The molecular alignment obtained in the hot drawing process facilitates the improvement in graphitic alignment in the carbon nanofiber formed. The effect of this enhanced alignment on single carbon nanofibers is studied via mechanical tests performed on single carbon nanofibers, with diameters of 250nm-700nm, using a microelectromechanical system (MEMS) device in conjunction with digital image correlation (DIC). It has been observed that improvement in the molecular alignment of the precursor fiber leads to improvement in strength and modulus of carbon nanofibers. This increase can be related to improvement in graphitic orientation and size of crystallites in the CNF.

In summary, it has been observed that molecular alignment in the PAN fiber prior to the stabilization stage is crucial in the evolution of graphitic domains, which was achieved via hot drawing. This effort presents a systematic study of molecular alignment and its effect on the mechanical properties of CNFs. Qualitative assessment of the morphology of the fibers is accomplished using Fourier Transform Infrared (FTIR), X-Ray diffraction (XRD), Selected Area Electron Diffraction (SAED), and Transmission Electron Microscopy (TEM).

ACKNOWLEDGMENTS

Foremost, I would like to thank my advisor, Dr. Mohammad Naraghi, for this continuous support and patience throughout my PhD. I have enjoyed working with him immensely; our engaging and open discussions about research have enabled me to be a better researcher than I imagined. My journey to complete my PhD has been enjoyable, with its challenges and rewards alike.

I would also like to thank my husband, Dr. Yogesh Babbar for this continuous support during my PhD. My parents, Anil Chawla and Veena Chawla have played an important role in my success. Without their support and sacrifices, this would not have been possible. I would also like to thank my aunt, Dr. Shobha Dadlani, for her constant support and encouraging words, enabling me to realize that even though there are tough times, the hard work is worth it. Lastly, I would like to thank my sister, Shweta Chawla, for her constantly supporting me during my PhD.

CONTRIBUTORS AND FUNDING SOURCES

The authors acknowledge the support from Air Force Office of Scientific Research, under the award number FA9550-15-1-0170, and Qatar National Science Funds, under the award number 8-2048-2-804. The FE-SEM acquisition was supported by the NSF grant DBI-0116835, the VP for Research Office, and the TX Eng. Exp. Station.

The authors would like to acknowledge the Microscopy and Imaging Center (MIC) at Texas A&M University for the use of SEM and TEM. The use of the TAMU Materials Characterization Facility (MCF) in Texas A&M University is acknowledged for the use of FIB, Raman, FTIR.

NOMENCLATURE

α	Ratio of von Mises stress and σ_{11}
λ_{XRD}	X-ray wavelength
λ	Draw Ratio
ρ	Density of PAN (g/cm^3)
2θ	Scattering angle (Bragg angle) in XRD, in degrees(°)
θ_{max}	Maximum orientation of turbostratic particles in the model
σ	Tensile strength of CNF obtained from experiments
σ_{11} (S_{11})	Tensile strength of CNF calculated from model
A_{am}	Area of amorphous region in XRD
A_{cr}	Area under crystalline peak at $2\theta = 17°$ in XRD
A_f	CNF cross section area
a_r	Aspect ratio of turbostratic particles
A_{true}	True cross sectional area of nanofiber
d_{hkl}	Lattice spacing
f	Hermann's orientation factor

$FWHM_{2D\,pattern}$	Full width at half max of the X-ray intensity as a function of the azimuthal angle ϕ
$FWHM_{Powder}$	Full width at half max of the X-ray intensity as a function of scattering angle θ
$I_{C\equiv N}$	Intensity of C≡N peak in FTIR
$I_{C=N}$	Intensity of C=N peak in FTIR
K	Shape Factor
k_l	Loadcell stiffness of MEMS device
l_0	Initial length of CNF
L_a	Out-of-plane dimension of crystallite of PAN
L_c	Crystallite size of PAN
phi	Orientation of PAN molecules w.r.t.fiber axis
u_f	Fiber displacement
u_l	Load cell displacement
v_f	Volume fraction of turbostratic particles
1xU	Carbon nanofibers prepared from PAN precursor nanofibers that were stabilized without gripped ends
1x	Carbon nanofibers prepared from as-electrospun ($\lambda = 1$) precursor nanofibers, stabilized with ends gripped

2x	Carbon nanofibers prepared from 2x hot drawn ($\lambda = 2$) precursor nanofibers, stabilized with ends gripped
4x	Carbon nanofibers prepared from 4x hot drawn ($\lambda = 4$) precursor nanofibers, stabilized with ends gripped
CF	Carbon fiber
CNF	Carbon nanofiber
CNT	Carbon nanotube
DIC	Digital image correlation
DMF	Dimethylformamide
DP	Diffraction pattern
DSC	Differential scanning calorimeter
ES	Electrospun
FTIR	Fourier Transform Infrared Spectroscopy
IA	Itaconic acid
MA	Methylacrylate
MEMS	Microelectromechanical systems
NF	Nanofiber
PAN	Polyacrylonitrile

RCI	Relative Cyclization Index
RF	Reaction force at nodes in model
SEM	Scanning electron microscope
TB	Turbostratic particle
TEM	Transmission electron microscope
tex	Unit of measurement of density (1tex=1g/km)
VMS	von Mises stress
XRD	X-Ray Diffraction

TABLE OF CONTENTS

Page

ABSTRACT ii

ACKNOWLEDGMENTS iv

CONTRIBUTORS AND FUNDING SOURCES v

NOMENCLATURE vi

TABLE OF CONTENTS x

LIST OF FIGURES xiii

LIST OF TABLES xix

1. INTRODUCTION AND SIGNIFICANCE 1

    1.1 Introduction 1
        1.1.1 Intrinsic Strength of Carbon Fibers 3
    1.2 Microstructure and Defects of Carbon Fibers 4
    1.3 Carbonized Materials with No Skin Core Inhomogeneity 11
    1.4 Potential Scalability of Graphitic Nanoparticles 15
    1.5 Goal and Objectives 16

2. MODIFYING THE MICROSTRUCTURE OF ELECTROSPUN POLYACRYLONITRILE NANOFIBERS 18

    2.1 Introduction 18
        2.1.1 Electrospinning 19
        2.1.2 Hot Drawing 29
    2.2 Experimental Work 34
        2.2.1 Effect of Electrospinning Parameters on Fiber Morphology 36
        2.2.2 Hot Drawing 43
        2.2.3 Mechanical Characterization 58
    2.3 Conclusion 61

3. HEAT TREATMENT: CONVERSION OF POLYMER NANOFIBERS TO CARBON NANOFIBERS 63

3.1 Introduction 63
3.2 Literature Review 64
  3.2.1 Chemical Changes in PAN Nanofibers during Stabilization 64
  3.2.2 Length Scale Dependence 68
  3.2.3 Fiber Shrinkage during Stabilization 69
  3.2.4 Effect of Stabilization Temperature and Duration on Morphology of CNFs 70
  3.2.5 Chemical Reactions during Carbonization 71
  3.2.6 Effect of Heat Treatment Parameters on Microstructure and Mechanical Properties of Carbon Fibers Prepared from PAN Precursors 73
3.3 Experimental Work 77
  3.3.1 Effect of Stabilization Temperature on Cyclization of PAN 77
  3.3.2 Carbonization of Stabilized PAN Precursor Nanofibers 95
3.4 Conclusion 103

4. MECHANICAL TESTING OF SINGLE CARBON NANOFIBER 105

4.1 Introduction 105
4.2 Experimental Method 107
  4.2.1 Testing Method 109
4.3 Results and Discussion 111
  4.3.1 Mechanical Properties of Single Carbon Nanofibers 112
  4.3.2 Failure Mode of CNF 119
4.4 Conclusion 121

5. FINITE ELEMENT MODELING OF MECHANICAL BEHAVIOR OF SINGLE CARBON NANOFIBER 123

5.1 Introduction 123
5.2 Model Development 124
  5.2.1 Material Properties 126
  5.2.2 Boundary Conditions 128
  5.2.3 Failure Criteria 128
  5.2.4 Mesh Convergence 130
  5.2.5 Effect of Orientation of Turbostratic Particles on Mechanical Properties of CNFs 132
5.3 Results and Discussion 133
  5.3.1 Overall Stress Distribution as a Function of θ_{max} 134
  5.3.2 Variation of Elastic Modulus with Particle Alignment 139
  5.3.3 Variation of Axial Strength on Particle Alignment 140
5.4 Conclusion 143

6. SUMMARY AND FUTURE DIRECTIONS 145

6.1 Summary 145
6.2 Future Directions 148
    6.2.1 Use of Copolymers 149
    6.2.2 Controlling Surface Defects 150
    6.2.3 Addition of Carbon Nanotubes (CNT's) 152

REFERENCES 154

LIST OF FIGURES

FIGURE Page

1.1 Chemical reactions during pyrolysis of PAN [1] 2

1.2 Proposed structure of carbon fiber: onion-structure [2] 5

1.3 Schematic representation of carbon fiber structures proposed by Knibbs [3] (a) ‘isotropic center’ with an outside skin of oriented crystalline material, (b) ‘double cross’ with the outside showing a different orientation to that of the center, (c) ‘single cross’ where the complete fiber shows one type of preferred orientation, also referred to as onion-skin structure by LaMaistre [2] 6

1.4 (a) Model of carbon fibers comprising tetragonal crystals and sharp edged voids [4], (b) structure of carbon fibers as proposed by Bennett and Johnson [5], (c) ribbon model of carbon fibers suggested by Perret and Ruland [6], (d) model of carbon fibers suggested by Diefendorf and Tokarsky [7] . 7

1.5 Schematic of carbon fiber structure [8] 8

1.6 Schematic representation of carbon fibers showing flaws [9] 9

1.7 Dependency of fracture stress on length and diameter of carbon fiber [10] 10

1.8 Microstructure of PAN-based carbon fiber proposed by Johnson [11] . . . 10

1.9 (a) Fiber with removal of surface layers, (b) raman spectra for locations a-e on the fiber, (c) c/s of the fiber, (d) ratio of G:D peak for location on fibers seen in (c)[12] 12

2.1 (a) Schematic of electrospinning, (b) bending instabilities during electrospinning, (c) typical SEM image of electrospun PAN nanofibers 21

2.2 Schematic illustration of taylor cone formation (a) surface charges on the solution droplet, (b) viscous drag exerted on the core deformed droplet, (c) taylor cone formed due to continuous viscous drag [13] 22

2.3 General effect of voltage on fiber diameter and number of jets formed [14] 23

2.4 Types of collectors (a) rotating drum, (b) split electrode [15], (c) rotating wire drum [16], (d) rotating disc [17] 26

2.5 Schematic showing chain orientation in fiber with fiber diameter [18] . . . 28

2.6 (a) Change in diameter with take up velocity of disc collector, (b) strength dependence of PAN, stabilized-PAN and carbon nanofibers with take up velocity of disc collector [19] 28

2.7 Schematic of hot drawing process 32

2.8 Effect of molecular weight on hot drawability at elevated temperature [20] 33

2.9 Electrospinning setup with a rotating drum collector 34

2.10 Electrospinning setup with a rotating disc collector 35

2.11 Breakup of jet during electrospinning leading to formation of nanofibers . 36

2.12 SEM Images of PAN nanofibers electrospun at different concentrations of PAN in DMF 37

2.13 Average diameters of PAN nanofibers electrospun using different concentrations of PAN in DMF 38

2.14 Schematic of molecular orientation in PAN 40

2.15 FTIR curve showing measurement of $A_{||}$ and $A_{\perp}$ 41

2.16 (a) Polarized FTIR for PAN nanofibers electrospun at disc speeds of 50 rpm, 500 rpm, 1000 rpm ($0.5 m/s$, $5.3 m/s$ and $10.6 m/s$, respectively), (b) Herman's orientation factor f as a function of disc speed 42

2.17 Experimental method to hot draw PAN ribbons 44

2.18 DSC of electrospun PAN nanofiber ribbon 45

2.19 Experimental method to hot draw PAN ribbons 46

2.20 (a) Polarized FTIR for PAN nanofibers at hot draw ratios 1x, 2x, 4x, (b) orientation factor f as a function of draw ratio 48

2.21 Schematic of crystalline and amorphous regions in a polymer 49

2.22 Powder X-Ray diffraction of 1x, 2x and 4x hot drawn PAN nanofibers . . 49

2.23 Crystallinity calculation for 4x hot drawn nanofibers 51

2.24 Hexagonal structure of PAN 53

2.25 2D Diffraction patterns for (a) 1x, (b) 2x, (c) 4x, (d-e): measurement method for FWHM calculation from diffraction patterns 55

2.26 Normalized powder diffraction curves used to calculate FWHM 57

2.27 (a) Schematic of sample holder, (b) Gatan Microtester, (c) Tested PAN nanofiber specimen 59

2.28 Tensile test of PAN nanofiber ribbons, hot drawn to 1x, 2x and 4x 60

3.1 Proposed model of fully aromatic cyclized ring structure [21] 65

3.2 Proposed chemistry for conversion of PAN during pyrolysis [22] 67

3.3 (a) Proposed model of fully aromatic cyclized ring structure [21], (b) proposed ladder structure [23] 67

3.4 Proposed chemistries for conversion of PAN to CNF (a) during stabilization [21], (b) release of H_2O [24], (c) release of N_2 and H_2 [25], (d) formation of turbostratic layers 72

3.5 Structure of (a) turbostratic carbon, (b) graphitic carbon [26] 73

3.6 Mechanical Strength of C-fibers formed by different stabilization temperatures and time [27] 74

3.7 Inter-molecular and intra-molecular reactions during stabilization of PAN [28] 74

3.8 Schematic of turbostratic domain showing L_a and L_c [29] 75

3.9 (a) TEM image showing crystallites of turbostratic carbon in nanofibers carbonized at 1400°C, (b) average fiber strength vs carbonization temperature, (c) fiber modulus vs carbonization temperature [30] 77

3.10 FTIR spectra of as-spun PAN nanofiber ribbon before stabilization 78

3.11 FTIR spectra for as-spun 1x PAN nanofibers stabilized at various temperatures 79

3.12 Relative cyclization index calculated for 'as-spun' (1x) PAN fibers stabilized at different temperatures 80

3.13 FTIR spectrum of PAN fibers stabilized at 295°C, showing the bonds present in the fiber 81

3.14 Color change in heat treated of PAN nanofiber ribbon. The associated ring cyclization index (RCI) is shown underneath each figure. The ring cyclization below ≈200°C is insignificant. 82

3.15 Carbon fiber obtained from PAN precursor stabilized at 295°C showing evidence of skin core structure 85

3.16 FTIR spectra for 2x hot drawn PAN nanofibers stabilized at various temperatures 87

3.17 FTIR spectra for 4x hot drawn PAN nanofibers stabilized at various temperatures 88

3.18 Relative cyclization index (RCI) for 1x, 2x and 4x hot drawn nanofibers . 89

3.19 DSC curves for 1x and 2x nanofibers 90

3.20 RCI for 1x, 2x, 4x nanofibers with step stabilization 92

3.21 Stabilization cycle used for (a) 1x, (b) 2x, (c) 4x nanofibers 93

3.22 SEM image of 4x carbon nanofibers stabilized using condition II showing uniform cross-section 94

3.23 Tube furnace used for carbonization 95

3.24 Carbonization cycle used for conversion of stabilized PAN nanofibers to carbon nanofibers 96

3.25 Proposed model of conversion of aligned PAN molecules forming turbostratic domains in CNF [31] 97

3.26 (a) Schematic of a CNF with turbostratic and amorphous domains, (b) TEM image of a typical CNF 98

3.27 TEM image of as-spun (1x) CNF carbonized at 1100°C at (a) 71kx, (b) 285kx, (c) 450kx 99

3.28 TEM image of 2x hot drawn CNF carbonized at 1100°C at (a) 5x, (b) 38kx, (c) 71kx, (d) 450kx 101

3.29 TEM image of 4x hot drawn CNF carbonized at 1100°C at magnification (a) 5x, (b) 38kx, (c) 97kx, (d) 450kx 102

3.30 Diffraction patterns of (a) 1x, (b) 2x, (c) 4x CNF, (d) intensity plot of diffraction pattern at 0.34nm (002) plane 103

4.1 (a) MEMS device used for testing single nanofibers, (b) schematic of test setup using MEMS device and picomotor 108

4.2 Top and side view of Pt blocks deposited using focused ion beam (FIB) . 108

4.3 Images at magnification 20x at three time steps during testing 109

4.4 Stress strain plots of 1xU, 1x, 2x and 4x single CNF 113

4.5 Strength and modulus of single CNF of 1xU, 1x, 2x and 4x 115

4.6 Average strength of 1xU, 1x, 2x and 4x single carbon nanofiber 116

4.7 Average modulus of 1xU, 1x, 2x and 4x single carbon nanofiber 117

4.8 Average strain to failure of 1xU, 1x, 2x and 4x single carbon nanofiber . . 118

4.9 SEM image of 1x CNF with surface pores and 2x and 4x CNF with improved surface 118

4.10 Single CNF failed in tension 119

4.11 TEM image of 4x CNF indicating failure surface 120

5.1 Schematic of model of carbon nanofiber 124

5.2 Schematic of turbostratic domain showing L_c and L_a 126

5.3 Schematic of turbostratic carbon depicting the 1, 2 and 3 directions 126

5.4 Boundary conditions applied to model of single CNF in ABAQUS 129

5.5 (a-d) show the seed size used to mesh the model of single CNF 130

5.6 Maximum von Mises stress in the amorphous region in the CNF model plotted with respect to strain, for various seed sizes 131

5.7 Distribution of von Mises stress seen in turbostratic particles and amorphous domain obtained from ABAQUS 134

5.8 Distribution of von Mises stress in the model of a single CNF using ABAQUS for orientation $\theta_{max} = 90°$ 136

5.9 Distribution of von Mises stress in the model of a single CNF using ABAQUS for orientation $\theta_{max} = 45°$ 136

5.10 Distribution of von Mises stress in the model of a single CNF using ABAQUS for orientation $\theta_{max} = 30°$ 137

5.11 Distribution of von Mises stress in the model of a single CNF using ABAQUS for orientation $\theta_{max} = 10°$ 137

5.12 Max von Mises stress in amorphous region plotted with respect to strain for cases of $\theta_{max} = 90°, 45°, 30°, 10°$ 138

5.13 Tensile strength plotted with respect to strain for cases of $\theta_{max} = 90°, 45°, 30°, 10°$ 139

5.14 Change in α with increase in misalignment of turbostratic particles 141

6.1 Effect of comonomers on structure stabilization [32] 150

LIST OF TABLES

TABLE Page

2.1 Comparison of polymer nanofiber fabrication methods [33] 20

2.2 Herman's orientation factor f and angle ϕ 43

2.3 Herman's orientation factor f and angle of backbone axis with fiber axis ϕ 47

2.4 Calculation of percent crystallinity 50

2.5 Calculation of interatomic spacing d using Bragg's law 54

2.6 Calculation of orientation index for crystalline phase 56

2.7 Calculation of crystallite size L_c 57

2.8 Summary of effect of hot drawing ratio on fiber properties 61

3.1 Diameter of CNF with corresponding fiber structure 85

3.2 Relative cyclization index (RCI) of final set of nanofiber ribbons that were carbonized 92

3.3 Orientation index of CNFs with hot drawing ratio 1x, 2x, 4x 100

4.1 Average values of modulus, strength and strain to failure obtained in tensile tests of 1xU, 1x, 2x and 4x single carbon nanofibers 112

4.2 Maximum values of modulus, strength and strain to failure obtained from tensile tests of 1xU, 1x, 2x and 4x single carbon nanofibers 114

5.1 Material properties of amorphous carbon (A) and turbostratic carbon (TB) used in ABAQUS 127

5.2 Average values of strength and modulus of 1xU, 1x, 2x and 4x single carbon nanofibers 140

5.3 Value of α with θ_{max} 141

1. INTRODUCTION AND SIGNIFICANCE

1.1 Introduction

Carbon fibers have received continually growing attention from industry since the 1950's. Initially carbon fibers were manufactured from cellulose-based materials. These were replaced by polyacrylonitrile (PAN) and pitch based fibers which, on pyrolysis, formed strands of carbon with strength exceeding 5GPa. This technology was quickly capitalized on by the United States Air Force and NASA and was used to replace metallic components with lighter and stronger carbon fiber reinforced composites. One of the most prominent success stories related to carbon fibers is the successful flight of the Boeing 787 Dreamliner which consists of 50% carbon fiber reinforced composite by weight.

Carbon fibers (CFs) are highly utilized for structural light-weighting because of their high specific strength and stiffness, reaching values as high as 4 GPa/g/cm^3 and 400 GPa/g/cm^3, respectively. In addition, carbon fibers have high electrical conductivity and thermal stability. Industrial scale carbon fibers are predominantly made from PAN precursor. To form the precursor fibers, the PAN precursor is dissolved in a highly polar solvent and then filtered and extruded into a coagulation bath. The extrusion process exerts elongational strains on the forming fibers, enabling alignment of the polymer chains. The fibers are then stretched in steam or dry air to improve the molecular orientation. After stretching, the fibers are heat treated in air at 200°C-300°C, in an oxidizing environment. This process is known as thermal stabilization. During this process PAN loses its nitrile - carbon triple bonds to form a ladder-like structure, which thermally stabilizes the fiber to prevent it from melting during the subsequent heat treatment. After stabilization, the fibers are heated in an inert atmosphere at temperatures $>$800°C to remove hydrogen, nitrogen and other non-carbon elements. This step is called carbonization which results in fibers with approximately 92% or more carbon content depending on the temperature of the carbonization. In order to achieve up to 99% carbon content, the fibers need to be heated further above 2000°C in a process called graphitization. Formation of enhanced molecular alignment in PAN leads to higher graphitic structure in CFs which is responsible for higher modulus in the fiber direction. Chemical reactions that take place during the conversion of PAN nanofibers to CNF [1] are shown in Figure 1.1.

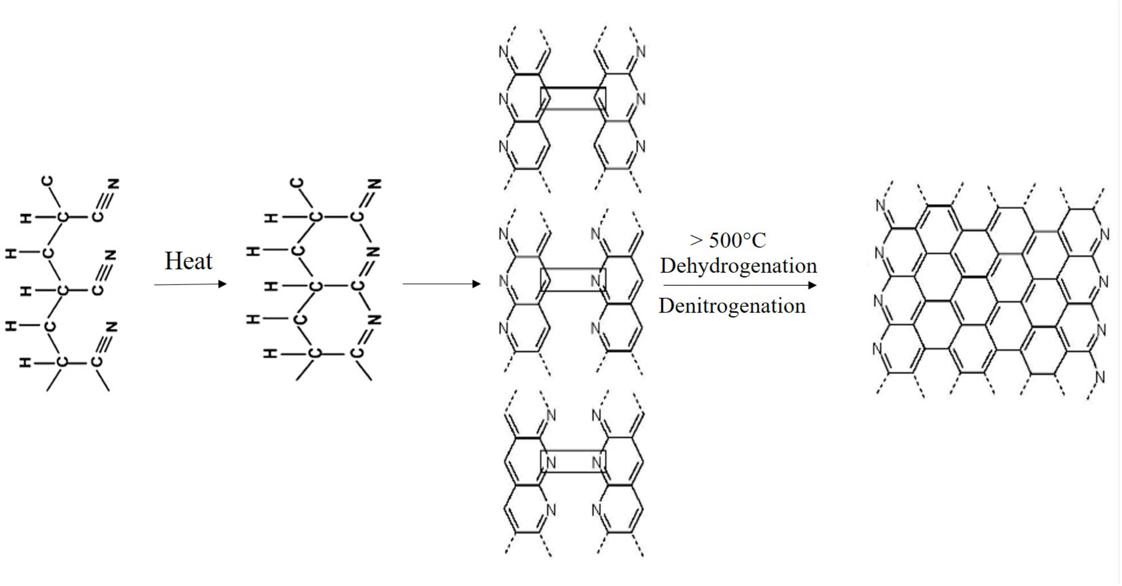

Figure 1.1: Chemical reactions during pyrolysis of PAN [1]

The first and critical step in conversion of PAN fibers to carbon fibers is thermal stabilization in air. The stabilization process enables the formation of a cyclic structure, thus preventing the chains from fusing to each other during the carbonization heat treatment. The stabilization process is an essential step to ensure the formation of mechanically strong carbon fibers. During this process, cyclization, dehydrogenation, aromatization, oxidation, and crosslinking reactions take place forming a ladder-like structure. The $C \equiv N$ bonds are converted into $C = N$ bonds during this process.

The next step in the process is carbonization. Carbonization is carried out in inert atmosphere at temperatures between 800°C-2000°C. At this temperature, the cyclic structures of neighboring PAN chains formed during stabilization, if aligned, combine to form turbostratic regions. Turbostratic regions can be thought of as defective graphitic structures, consisting of nearly parallel, mis-oriented graphene sheets stacked on each other. They are irregularly folded, tilted or split and may contain sp^3 hybridized carbon atoms. The irregular stacking and sp^3 bonding causes the d-spacing between sheets to increase from 0.335nm as in graphite to 0.344nm or more in turbostratic domains [34, 35]. As graphite and graphene have high in plane strength and modulus, alignment of the basal planes of the turbostratic domains with axis of CFs imparts these properties to the CF. Similarly, higher concentration of these regions causes increase in axial properties of the fibers. The concentration of the graphitic regions can be increased by carbonizing at higher temperatures. The processes to convert PAN fibers to carbon fibers can also be used to create carbon nanofibers (CNFs) from PAN nanofibers. That is, PAN nanofibers are stabilized in an oxidative environment at temperatures ranging from 180°C-300°C. There is currently little literature on the effect of stabilization conditions on fibers with diameters in the submicron range [36, 37, 38].

1.1.1 Intrinsic Strength of Carbon Fibers

Using the method described above, CFs and CNFs with moduli in the range of 100GPa - 700GPa [17, 30, 34] have been fabricated from polymeric precursors. The fibers formed at high carbonization temperatures (1400°C and above) have moduli that are comparable to those of carbon nanotubes (CNTs) and graphene when the latter is loaded along their basal plane (modulus of carbon fibers can be as high as 700GPa, compared to modulus of graphene of $\approx$1TPa) [17, 34, 39, 40, 41]. However, CFs have been unable to achieve the high strengths of their nanoscale graphitic counterparts, i.e., CNTs and graphene. For instance, the strength of CNTs can reach values of as high as 100GPa, compared to the strength of carbon fibers which does not exceed ≈6.3GPa (Toray Carbon fibers, Grade T1000G have tensile strength of 6.3GPa and Young's modulus of 295GPa) [42]. One explanation for the relatively low strength of carbon fibers is the mechanical size effect as seen in brittle materials. In other words, because of the difference in length scales, the possibility of the existence of defects bigger than a critical size is greater in CFs than in the nanoscale materials. Carbon fibers possess defects ranging from the atomic scale to the micro scale. Some of these include imperfect stacking in the graphene planes, dislocations, waviness of graphene layers and pores or pits on the fiber surface [4, 34].

The classical size effect can be evaluated by estimating the intrinsic strength of the carbon fibers. For this purpose, the strength of carbon fibers at different length scales is tested and is extrapolated to zero length, using Weibull distribution of tensile strength [34, 43]. Using this method, the intrinsic strength of carbon fibers is calculated to be 6-10GPa, which is still significantly lower than CNTs and graphene sheets ≈120GPa and 50GPa respectively [41, 43]. Moreover, despite numerous efforts to improve strength of carbon fibers for instance via surface treatments to remove surface defects, it is important to note that over the last 25-30 years, CFs have not seen significant improvement in properties. This suggests the presence of other factors causing strength deficiency in carbon fibers as discussed in the following sections.

1.2 Microstructure and Defects of Carbon Fibers

Carbon fiber properties largely depend on precursor type and pyrolysis temperature. Studies by LaMaistre and Diefendorf [2] of cross-sections of fully stabilized Courtelle fiber [93% PAN, 6% methyl acrylate (MA) and 1% itaconic acid (IA)] based carbon fibers viewed under the optical microscope with polarized light, showed an onion-skin type cross section of the fiber, with orientation parallel to the fiber surface (Figure 1.2).

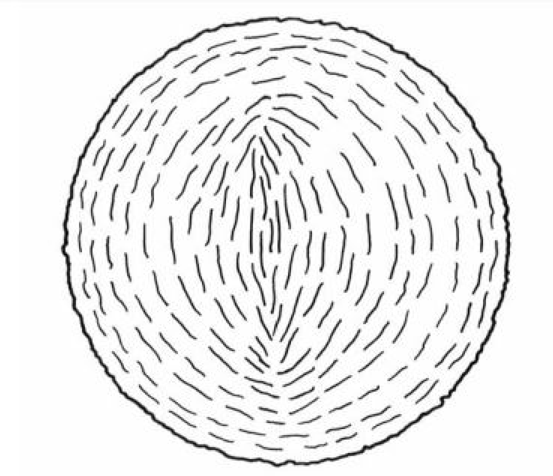

Figure 1.2: Proposed structure of carbon fiber: onion-structure [2]

In contrast, commercially produced carbon fiber, showed a radial texture in the core with circumferential orientation in the sheath. High modulus carbon fibers analyzed by Wicks and Coyle Wicks have shown at least four different types of layer plane arrangements in different filaments. Knibbs [3] claims that the texture of the fibers can be controlled and altered depending on the processing conditions, varying from a circumferential orientation throughout the fiber cross section to a circumferential sheath with a radial or isotropic core as seen in Figure 1.3. The presence of an isotropic core is the result of under-stabilization of the fiber center as will be discussed later in this section in detail.

To orient the domains such that the basal planes of the turbostratic domains are along the direction of the fiber axis, molecular chains in the precursor should be aligned and oriented with the fiber axis. To achieve that, various methods have been adopted by industry and researchers. Some of these methods include drawing the PAN fibers in boiling water or saturated steam [20, 44], drawing PAN fibers in a bath of diluted $CuCl_2$ [45] or

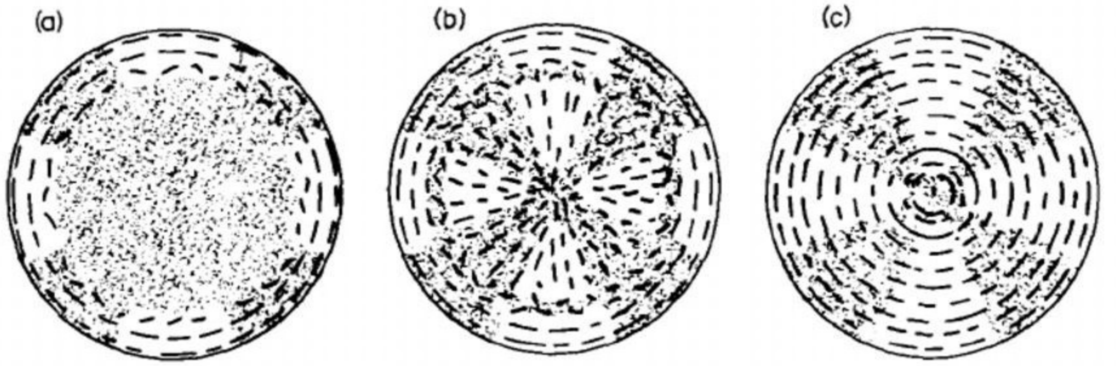

Figure 1.3: Schematic representation of carbon fiber structures proposed by Knibbs [3] (a) 'isotropic center' with an outside skin of oriented crystalline material, (b) 'double cross' with the outside showing a different orientation to that of the center, (c) 'single cross' where the complete fiber shows one type of preferred orientation, also referred to as onion-skin structure by LaMaistre [2]

DMF solutions [46], or dry stretching PAN fibers in nitrogen atmosphere or air at elevated temperatures [47, 48, 49].

Based on direct visualization of CFs via probe microscopy techniques and TEM imaging, various models have been proposed to describe the microstructure of CFs. Barnet and Norr [4] suggested a schematic of the carbon fibers as seen in Figure 1.4. In his proposed model, S_1 is a void, S_2 is a subgrain twist boundary, S_3 represents inter-crystalline boundary, L_c and L_a are the thickness and diameters of carbon layer stacks and D is the distance between them. Subgrain boundaries were suggested on the basis of microscopy results orthogonal to the crystal direction (Figure 1.4(b)). Model of carbon fibers from PAN based precursors by Perret and Ruland Perret proposed a ribbon like structure for carbon fibers, seen in Figure 1.4(c). The ribbon of carbon have sp^2 structure, 5nm to 7nm in width. The ribbons can contain straight regions of 6nm to 13nm length. Other researchers also observed parallel stacking of the ribbons [50, 51, 52, 53, 54]. The ribbons contain gaps (voids) between them. Models showing similar concepts have been proposed by Hugo

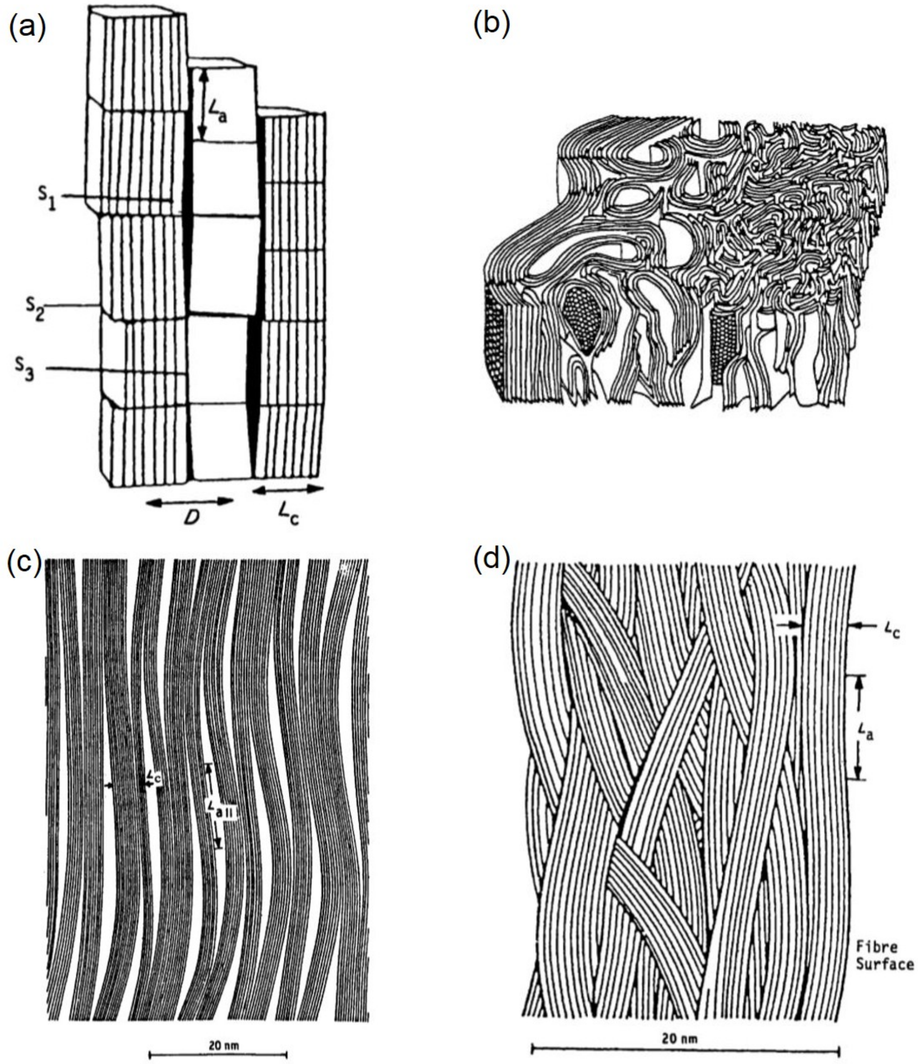

Figure 1.4: (a) Model of carbon fibers comprising tetragonal crystals and sharp edged voids [4], (b) structure of carbon fibers as proposed by Bennett and Johnson [5], (c) ribbon model of carbon fibers suggested by Perret and Ruland [6], (d) model of carbon fibers suggested by Diefendorf and Tokarsky [7]

[55]. Instead of ribbons, Diefendorf and Tokarsky [7] proposed microfibrils of 10 to 30 basal planes in ribbon, as seen in Figure 1.4(d). It has been seen that low modulus fibers have ribbons that are 13 layers thick and 4nm wide which increases to 30 layer thick and 9nm wide for high modulus fibers.

Another proposed structure of CF, similar to the one proposed by Bennett [5] is shown in Figure 1.5 [8]. The Figure 1.5 shows a less oriented core with twisted crystallites and amorphous regions. The outer skin is made up of graphitic planes with van der Waals (vdW) forces between them.

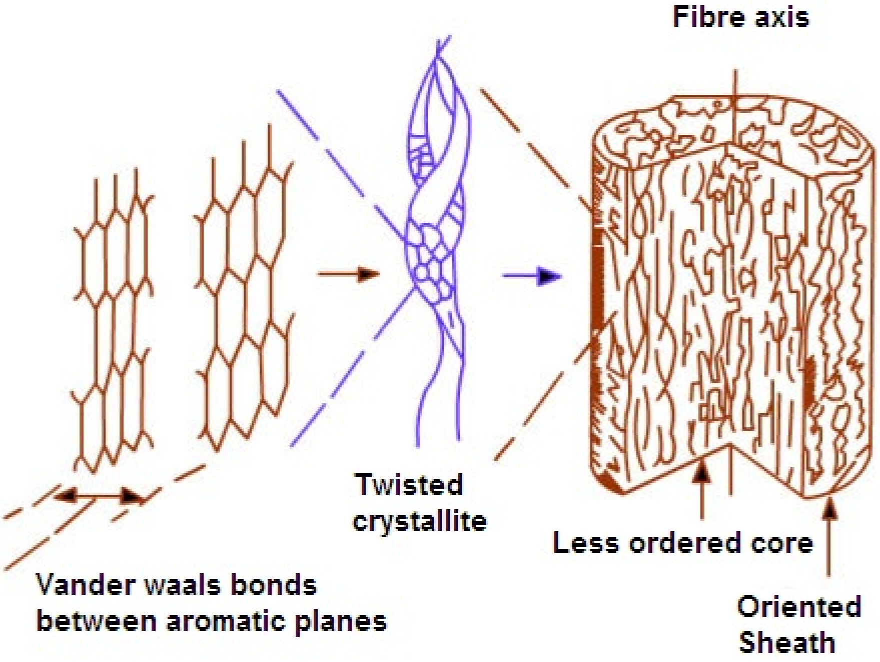

Figure 1.5: Schematic of carbon fiber structure [8]

Flaws can develop in carbon fibers during their fabrication. Liu [9] proposed a schematic showing different flaws that can be present in carbon fibers. For example, internal stresses developed during spinning or heat treatment of the fiber can be the cause of small cracks in the fiber. Morphology of the precursor can promote entanglements between chains, voids and disordered structures. In addition, radial inhomogeneity can form due to insufficient diffusion of oxygen to the core during stabilization of the precursor fiber as explained in the following paragraphs.

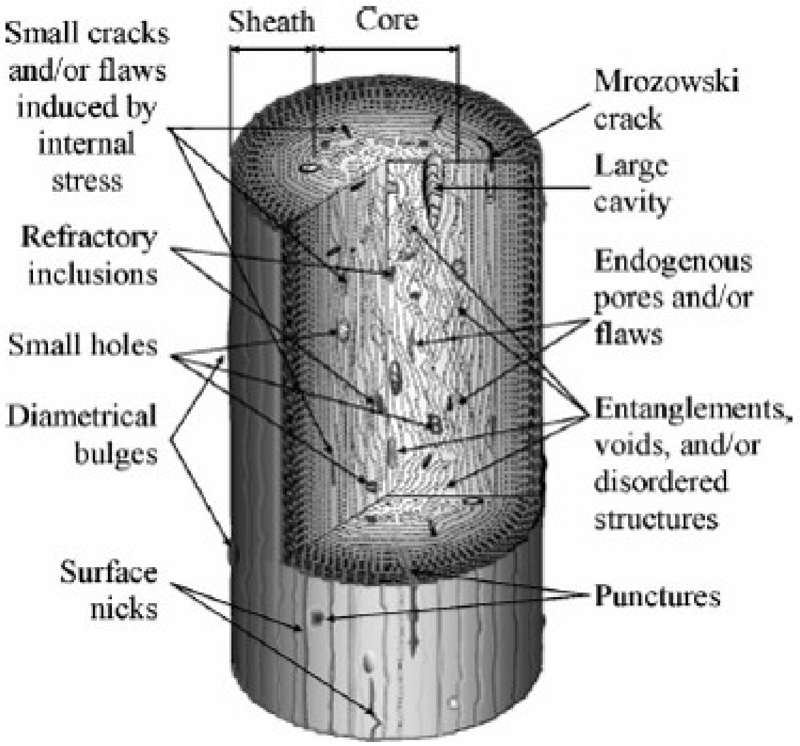

Figure 1.6: Schematic representation of carbon fibers showing flaws [9]

In the microstructure of PAN based CFs, a radial inhomogeneity is distinguishable which compromises strength. According to Tagawa et. al [10], the dependency of tensile strength of the fiber on radius is ten times more pronounced than length (Figure 1.7). This is a key finding, which can partly explain the low strength of the carbon fibers relative to graphitic structures such as CNTs.

The evidence in support of the radial inhomogeneity (Figure 1.8) [11, 56] are numerous, including scanning electron microscope (SEM) images of high modulus carbon fibers by many researchers [7, 8, 57, 58, 59].

While the outer skin has a large proportion of graphitic structure, the core is predominantly composed of amorphous carbon and/or randomly oriented turbostratic domains. A number of researchers have addressed the cause of radial inhomogeneities in carbon fibers

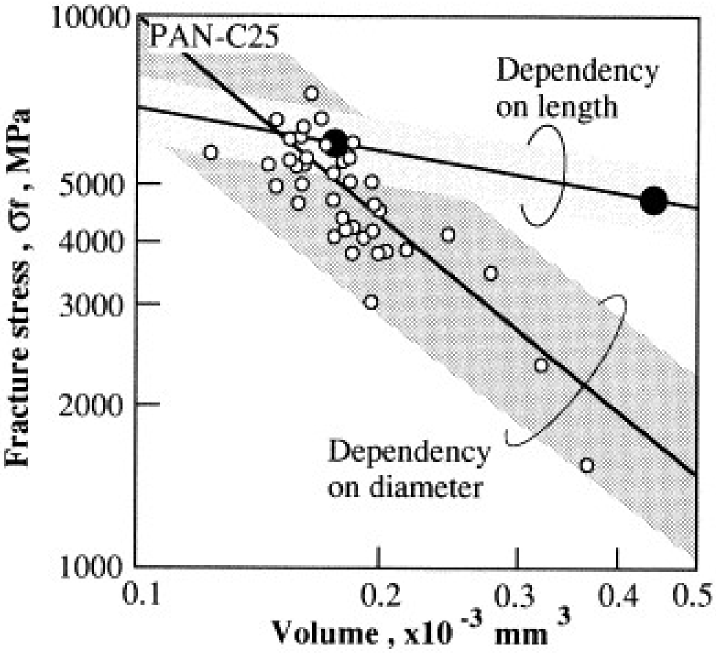

Figure 1.7: Dependency of fracture stress on length and diameter of carbon fiber [10]

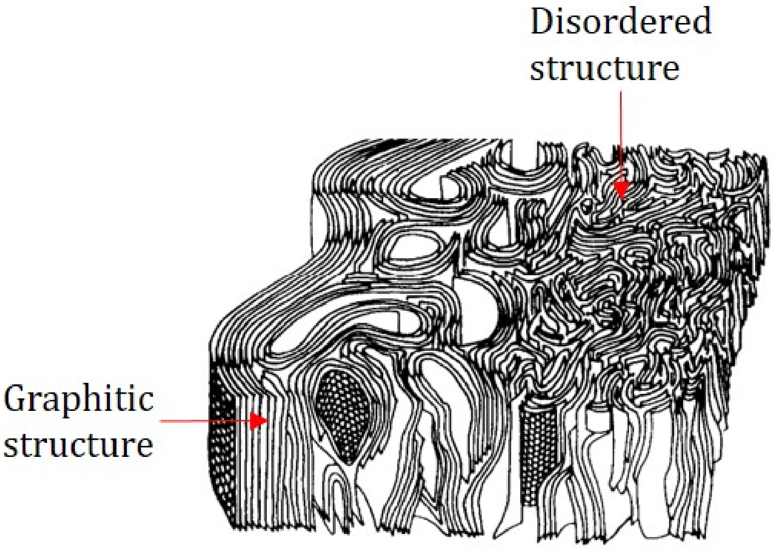

Figure 1.8: Microstructure of PAN-based carbon fiber proposed by Johnson [11]

[9, 12, 60, 61]. It is largely speculated that the existence of skin-core structure originates from the stabilization process. Stabilization of PAN is an exothermic process. Oxygen from the air diffuses into the fiber and volatile species and heat from the fiber diffuse outward. On the skin, oxygen diffuses inwards at a rate demanded by the stabilization reactions from the environment, while the heat evolved during the process diffuses outwards, forming a cyclized structure on the skin. With evolution of the stabilization process on the skin, the rate at which the oxygen diffuses into the fiber reduces. As a result, the rate at which the fiber stabilizes reduces over time. Moreover, carbon fibers are manufactured at very high temperatures, sometimes $>$2000°C, and subsequently cooled down to room temperature. When the fiber is cooled down to room temperature, it experiences a mismatch in the thermal expansion coefficients of the skin and core regions. On cooling, this mismatch can lead to significant defects in the fiber and create micro voids. Another source of lower strength in the fibers is orientation of graphitic regions particularly in the core, facilitated by the relatively poor state of stabilization. The graphitic regions in the fiber possess maximum strength in the in-plane direction and lower in the out-of-plane direction. As a result, the mis-orientation of these domains can lead to significantly lower strength in the fiber. It is however to be pointed out that since stabilization requires the diffusion of oxygen to the core of the fiber, it is dependent on the length of diffusion, i.e. the fiber diameter.

1.3 Carbonized Materials with No Skin Core Inhomogeneity

Radial inhomogeneities or skin-core structure of carbon fibers, as discussed before, depends on the diffusion of oxygen in the material from the environment, and as such it is dependent on the temperature and rate of stabilization. Stabilization performed in an oxidizing environment leads to dehydrogenation and cyclization of the fiber. Thus, stabilization is based on diffusion of oxygen into the fiber. Oxygen enters the fiber through the surface, modifying the structure along the way. Moreover, thermal stabilization is an exothermic process and during this process, heat and volatile species, such as NH_3 gas [62] are produced which need to be dissipated through the skin of the fiber. This dissipation of heat and volatile species is also a diffusion process starting from the core of the fiber, diffusing outward. As pointed out by Liu [9], diffusion of oxygen into the fiber and diffusion of byproducts exiting the fiber are important parameters controlling the rate of stabilization of the fibers. If the temperature of stabilization is too low, it leads to incomplete stabilization of the fiber. On the other hand, if the rate of stabilization is too high (for instance by stabilizing at rather high temperatures), it may cause the skin which is in direct contact with the environment (source of oxygen) to be fully stabilized before the core. Once the skin is fully stabilized, the volatiles from the core of the fiber may not be able to diffuse through the fiber skin, leading to incomplete stabilization or even inducing defects on the surface upon exiting.

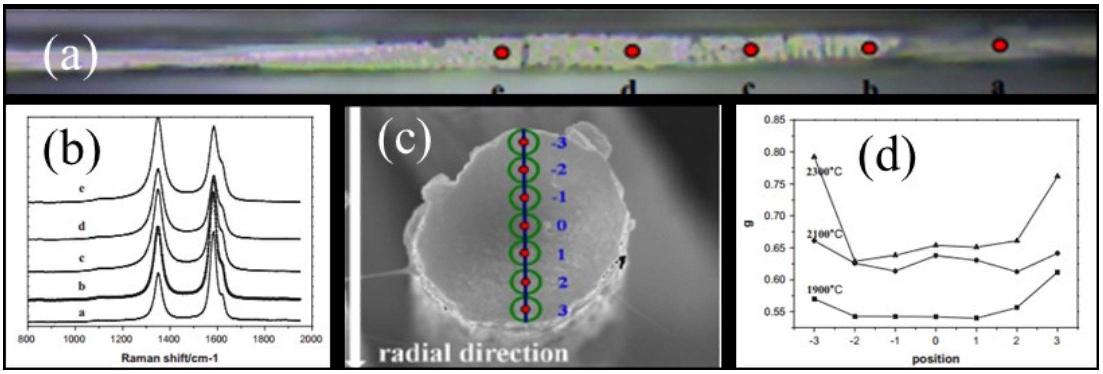

Figure 1.9: (a) Fiber with removal of surface layers, (b) raman spectra for locations a-e on the fiber, (c) c/s of the fiber, (d) ratio of G:D peak for location on fibers seen in (c)[12]

Direct observation of the microstructural variations between the core and skin of the fiber may be difficult by optical or scanning electron microscopy. However, in case of large radial homogeneities, transmission electron microscopy is able to show some differences in the fibers in the radial direction. On the other hand, Raman spectra of the carbon fiber can clearly demonstrate the variation of defect density in the cross section of carbon fibers. Wang et. al. [12], showed the change in microstructure of carbon fibers using Raman spectra. Figure 1.9(a) shows the fiber, with the skin removed progressively from location (a)-(e). Figure 1.9(b) shows the D and G peaks of the fiber at these locations. Analyzing the cross section of the fiber, Figure 1.9(d) shows the ratio of G/D peak, which increases as we go from the core to the skin. Thus, the skin is significantly more graphitic and less defective than the core.

Considering the mechanism of stabilization which is diffusion-based, it is evident that the skin-core inhomogeneity will be significantly reduced by reducing the diameter of the fibers to form carbon nanofibers. This is supported by the Raman spectra of the fiber in radial direction as seen in Figure 1.9(d). It is clear that the g value in G/D peak drops significantly from location 3 to location 2 on the fiber. This means that the fiber has been graphitized in this region of the fiber, referred to as the skin of the fiber. Hypothetically, if the fiber diameter was to be reduced to the thickness of the skin, a highly graphitic fiber would be obtained with lower radial inhomogeneities. This would lead to the formation of carbon nanofibers, with more uniform structure and higher strength.

To analyze the maximum strength achievable by carbon nanofibers, Naraghi and Chawla [63] developed an analytical model for CNFs consisting of amorphous and turbostratic domains. The proportion of each domain was varied to study the effect of increasing turbostratic regions in the fiber. In addition, alignment of the turbostratic domains was also studied. Using this model, the strength of carbon nanofibers with perfectly aligned crystallites was calculated to be 14GPa. Details of the model can be found in [63]. Another study by Penev et. al. [64] estimated a strength of approximately 21GPa using atomistic models of the graphitic/amorphous carbon nanofiber.

While a fair amount of research has been conducted on the fabrication of carbon nanofibers and the effects of scaling down from carbon fibers, a systematic investigation into the factors affecting microstructure and mechanics of nanoscale carbon fibers is missing. In addition, the significance of graphitic alignment in carbon nanofibers and methods to induce that in a scalable fashion remains to be addressed.

A common method to promote graphitization and graphitic alignment in CNFs is by embedding carbon nanotubes (CNTs) in the polymer nanofiber precursor, thus creating PAN/CNT composite nanofibers. The studies thus far have concentrated their efforts on the improvement in quantity of turbostratic/graphitic domains forming around the CNTs, or on the use of nanotubes to template graphitization in the fiber core [65, 66]. Moreover, during electrospinning, CNTs attain partial alignment along the direction of fiber axis due to electromechanical forces on the spinning jet, thus creating partially aligned graphitic domains in their subsequent nanofibers. Prilutsky et. al. [65] showed that the addition of CNTs to PAN nanofiber precursors led to an increase in the graphitic domains in the carbon nanofiber. Papkov et. al. [67] showed that the addition of a small amount of CNTs improved the graphitic structure and crystal orientation dramatically in CNFs. Their study revealed that the graphitic templating effect observed with the incorporation of 1.2wt% DWNTs was at par with that obtained at carbonization temperatures of 1850°C of pristine PAN nanofibers. In another study, Prilutsky [66] showed that while an increase in carbonization temperature from 750°C to 900°C lead to increase in the turbostratic domains in the nanofiber, carbonization time did not have a pronounced effect. Arshad et. al [30] carbonized PAN nanofiber ribbons at temperatures upto 1700°C and studied mechanical properties of individual CNFs. Their studies demonstrated that the increase in carbonization temperature in CNFs monotonically increases elastic modulus, while the highest strength of CNFs was observed at a carbonization temperature of 1400°C.

While work has been carried out to improve the turbostratic/graphitic domains in the

CNFs, there is no reported literature on improving the alignment of these graphitic domains in pure PAN-based CNFs. As can be seen from SEM images by Arshad [68], the carbon nanofibers do not show a pronounced skin-core formation, and have turbostratic domains present throughout the nanofiber. However, these domains show no preferred orientation in the direction of fiber axis. As turbostratic domains are mis-oriented graphene sheets stacked on each other, the turbostratic domains will be most effective in enhancing the strength and modulus of CNFs when the basal plane of the graphene sheets is lined up with the fiber axis. Hence, fabricating carbon nanofibers with turbostratic domains aligned in the direction of fiber axis is of prime importance.

1.4 Potential Scalability of Graphitic Nanoparticles

Given the remarkable axial (in-basal plane) strength and stiffness of graphitic particles, such as carbon nanotubes, graphene nanoparticles and carbon nanofibers, this class of particles seem to be part of the future of high strength reinforcements, as carbon fibers are the industry's best at the moment. In this regard, nearly defect-free CNTs are known for their high strength. However, the cost of producing defect-free CNTs is prohibitively high. In the US, the cost of purchasing low defect density CNT's is about \$100/g [69]. This extreme cost of producing the nanotubes is a major drawback in its application and scalability. In addition, graphene possesses extremely good mechanical properties. Unfortunately, graphene is currently fabricated on the laboratory scale as the issue of scalability of graphene remains unresolved. Another issue with the use of graphene and CNTs is that they are chemically inert in the out of plane direction. In order to incorporate them in a matrix, they need to be functionalized. Functionalization often breaks the sp^2 bonds to form covalent (sp^3) bonds with the CNT/graphene. This conversion of the bonds significantly lowers the strength of the CNTs and graphene.

In contrast to CNTs and graphene, the method proposed in this work to produce carbon nanofibers has immense potential for scalability. The stabilization and carbonization procedures for fabricating carbon nanofibers are the similar to those used for fabricating carbon fibers. Upon realization of the method and conditions to modify the microstructure of the CNFs, this method can directly be used in a carbon fiber manufacturing plant to manufacture nanofibers. The stage which will mainly require modification is the fabrication of the precursor material (PAN nanofibers) with proper molecular structure. Hence, with the current industrial practices in place, scalability of our proposed method is possible.

1.5 Goal and Objectives

As discussed in the previous sections, the inherent microstructural defects of carbon fibers, such as skin-core inhomogeneity, inhibits them from attaining the upper limit of properties of graphitic structures such as CNTs and graphene. The radial inhomogeneity that exists in carbon fibers has been one of the leading reasons for stagnation in the development of higher grade carbon fibers. In contrast, the graphitic structure of the state-of-the-art carbon nanofibers, due to their smaller diameters, do not show considerable radial dependence. On the other hand, CNFs often contain nearly randomly oriented turbostratic domains which leads to significant compromises in their strength and modulus.

To address the above challenges, the goal of this work is to study the processing-microstructure-mechanics relationships in carbon nanofibers with an emphasis on controlling the graphitic alignment and radial homogeneity. To this end, we have pursued the following objectives:

- *Objective 1 (Chapter 2):* Investigate processing microstructure relationships in PAN nano-fibers as the precursor for CNFs, and modify the microstructure of PAN to enhance chain alignment,

- *Objective 2 (Chapter 3):* Investigate the role of thermal stabilization on the cyclization of PAN nanofibers

- *Objective 3 (Chapter 4):* Investigate the effect of thermal stabilization conditions and the role of graphitic alignment on mechanical properties of CNFs,
- *Objective 4 (Chapter 5):* Develop continuum models to capture the mechanical behavior of individual CNFs and identify the most critical microstructural parameters affecting mechanics of CNFs.

The conclusion of all objectives and proposed future directions are discussed in Chapter 6.

2. MODIFYING THE MICROSTRUCTURE OF ELECTROSPUN POLYACRYLONITRILE NANOFIBERS

2.1 Introduction

This chapter focuses on fabrication and modification of the microstructure of polyacrylonitrile (PAN) as precursors for carbon nanofibers (CNFs). Although the polymer chains experience massive elongational forces during electrospinning, the fast solvent loss during electrospinning and the consequent loss in chain mobility often suppresses chain alignment. As a result, as-spun nanofibers often have very limited chain alignment. On the other hand, increasing the chain alignment in electrospun nanofibers can lead to higher crystallinity, while enhancing their mechanical properties such as strength and modulus. Moreover, chain alignment in precursor polymer fibers is a prerequisite for the formation of highly aligned turbostratic domains in subsequently formed CF, such that the precursor chain backbone is more or less parallel to the basal plane of the turbostratic domains.

In this chapter, we will first present a literature review on morphology-processing relationships in electrospinning. We will then present prior works on inducing polymer chain alignment via hot drawing of fibers. Following this we will present our results on fabrication of electrospun PAN nanofibers using a solution of PAN dissolved in dimethyformamide (DMF). Electrospinning was our method of choice owing to its advantages over other methods of fiber production viz., fair range of diameters within the nanoscale, high aspect ratio of fibers, process repeatability and simplicity of setup. In addition, by adopting a suitable collector, aligned fibers can be electrospun with initial (but limited) molecular orientation predominantly in the length direction of the fiber. We will then demonstrate thermomechanical treatments to considerably enhance chain alignment, and demonstrate the effect of the treatment parameters on chain alignment via polarized Fourier Transform

Infrared (FTIR) spectroscopy and Wide Angle X-Ray Diffraction (WAXD) measurements.

2.1.1 Electrospinning

According to ISO TS 27687, fibers, plates, and particles are considered as nanoscale materials if at least one of their dimensions is between 1-100nm. However, fibers with diameters below 1000nm are often accepted in many scientific articles and industries as nanofibers. Since the early 2000's, nanofiber research has gained impetus, with the market for nanofiber based products increasing from \$128 million in 2011 to \$570 million by 2017 [70]. Currently, nanofibers are being researched for a number of applications including bioengineering of tissue scaffolds [71, 72, 73], filtration devices [74, 75], in semiconductor devices [76] and as fillers for matrix materials [77]. In the field of bioengineering, porous polymer nanofibers are being studied for use in drug delivery applications. Single nanofibers can be used as part of miniaturized electronic circuits, functioning as a nanodevices [33]. In addition, the high specific surface area of electrospun polymer and carbon nanofibers may lead to superior properties in various applications such as electrodes in fuel cells and supercapacitors [78, 79, 80, 81].

A number of methods are used for processing of polymer nanofibers. The fabrication methods can be classified based on polymer type used, production cost, scalability, quality, properties and end use of the nanofibers. Methods to fabricate nanofibers include drawing, template synthesis, phase separation, self-assembly and electrospinning. These have been reviewed in Table 2.1.

Electrospinning is a process that was first known to be used in the late 19th century to draw fibers from materials like shellac and beeswax [82]. The process of electrospinning was first patented in 1900 by J. F. Cooley [83, 84, 85]. However, commercial developments were only patented in 1934 [86, 87] and the process has gained commercial significance only in the past two decades or so for fabrication of a wide range of polymer nanofibers.

Process	Drawing	Template Synthesis	Phase Separation	Self-Assembly	Electrospinning
Scalability	N	N	N	N	Y
Repeatability	Y	Y	Y	Y	Y
Ease of Processing	Y	Y	Y	N	Y
Control of fiber dimensions	N	Y	N	N	Y
Advantages	Minimum equipment required	Various diameter fibers can be fabricated	Minimum equipment required, batch to batch consistency, nanofiber matrix can be directly fabricated, mechanical properties can be altered	Good for obtaining smaller nanofibers	Cost effective, long continuous nanofibers can be produced
Disadvantages	Discontinuous process	-	Only some polymers can be used	Complex process	Jet instability, leading to distribution of diameters

Table 2.1: Comparison of polymer nanofiber fabrication methods [33]

Figure 2.1(a) is a schematic of the electrospinning process. The electrospinning setup consists of three main components: syringe infusion system, high voltage power supply and a collector. A high voltage is applied between the syringe tip and the collector to create an electric field between them, stretching the solution as it leaves the needle tip and getting deposited on the collector. The solution in the needle experiences electrostatic forces exerted by the external electric field, as well as surface tension in the needle tip.

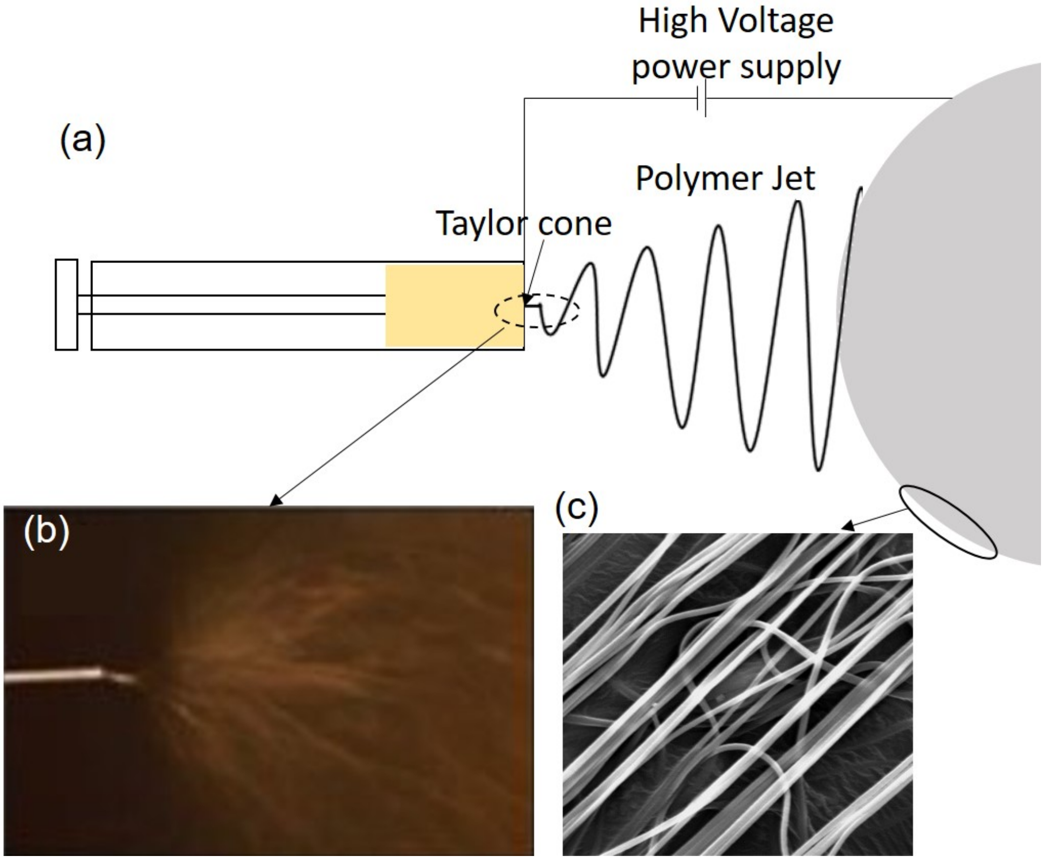

Figure 2.1: (a) Schematic of electrospinning, (b) bending instabilities during electrospinning, (c) typical SEM image of electrospun PAN nanofibers

Once the solution is infused it forms a droplet at the needle tip. When the electrostatic charges experienced by the droplet overcome the surface tension, the solution leaves the needle tip, forming a conical jet, called the Taylor cone (Figure 2.2). The Taylor cone is

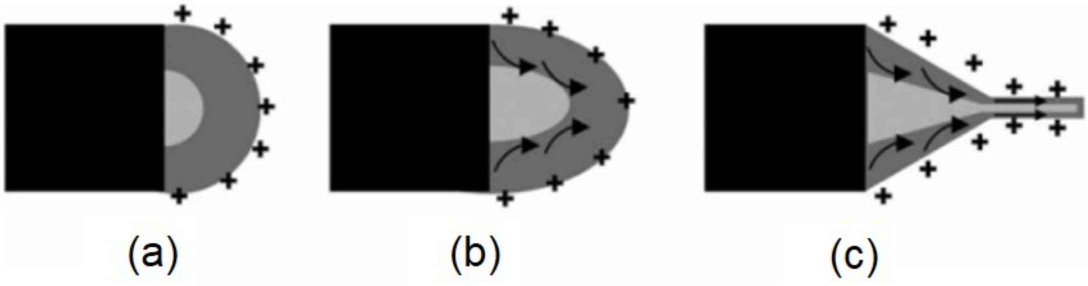

Figure 2.2: Schematic illustration of taylor cone formation (a) surface charges on the solution droplet, (b) viscous drag exerted on the core deformed droplet, (c) taylor cone formed due to continuous viscous drag [13]

unstable and experiences whipping motion as it moves towards the collector while elongating the fibers and reducing the diameter. The whipping motion causes reduction in diameter from many microns to hundreds and tens of nanometers [79]. The breaking of the jet as it comes out of the needle to the collector is seen in Figure 2.1(b) and a typical SEM image of the fibers obtained in Figure 2.1(c). As observed in Figure 2.1(b), it appears that multiple jets are formed during the electrospinning process from the needle tip to the collector. However, with the help of high speed photography, Yarin et. al. [88, 89], found that there is a single jet that is rapidly whipping, leading to the conclusion that the jet does not break up into multiple jets, but has one jet that is rapidly moving and bending to create the nanofibers. Other studies have also shown that at sufficiently high voltages, the single jet breaks up and forms multiple jets during electrospinning [90, 91] (Figure 2.3).

The key features of the electrospinning process are:

- The polymer is often dissolved in a solvent to lower the viscosity,
- The vapor pressure of the solvent must be adequate for it to evaporate before the fiber reaches the collector. However, very high vapor pressure is not desired as it may suppress jet drawing due to premature vitrification before reaching its desired

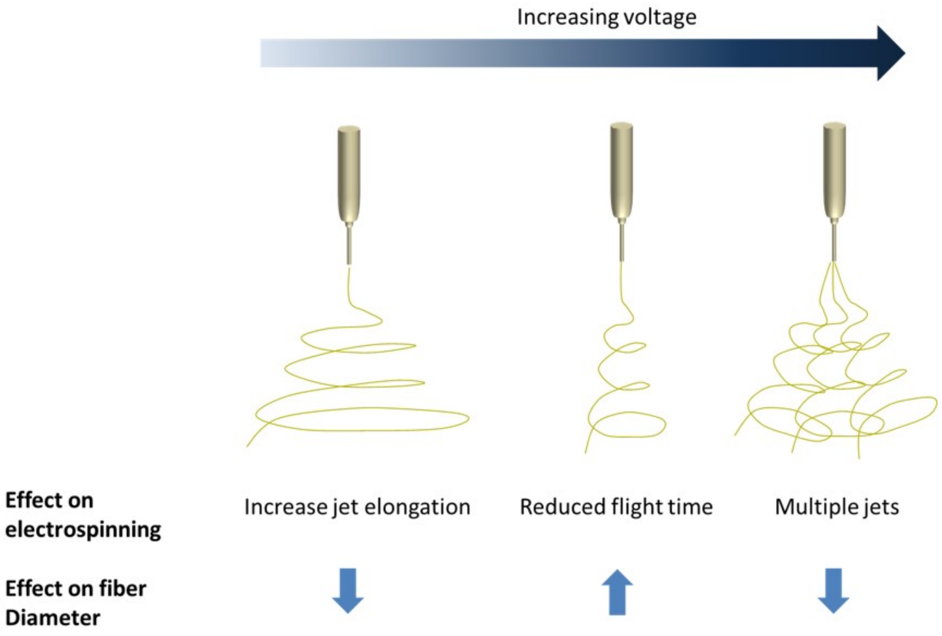

Figure 2.3: General effect of voltage on fiber diameter and number of jets formed [14]

diameter,

- The solution should have sufficient viscosity and surface tension, so that it does not flow freely from the syringe tip, but should also not be so viscous that it prevents the solution from leaving the needle tip,
- The power supply should be able to sustain a jet flowing from the tip to the collector, and should also be able to overcome the viscosity and surface tension of the solution.

Key parameters affecting nanofiber morphology and diameter: Material and processing parameters during electrospinning play a significant role in the final morphology and diameter of electrospun nanofibers. Type of polymer, its molecular weight, electrical conductivity, viscosity, polymer chain conformation are some of the parameters affecting the fiber properties. In addition, solubility, evaporation rate, polarity and surface tension of the solvent affects the electrospinning process.

The formation of droplets or beads in the fiber during electrospinning is a problem frequently observed by researchers [92, 93, 94]. On leaving the needle, the polymer forms a configuration of least surface area, causing the surface tension to form droplets, while the electrostatic repulsion between the charges on the jet, favors formation of thin fibers by increasing the surface area. Also, sudden changes in shape are resisted by the viscosity of the solution, thus favoring fiber formation. Hence, proper tuning of viscosity, surface tension and electrostatic forces is required to obtain bead free fibers.

With the aim to understand the parameters required to yield bead free fibers, poly (acrylonitrile-co-methyl acrylate) copolymer in DMF was electrospun [95]. Polymer concentration, distance between the collector and the infusion system and applied voltage were varied in order to alter the solution viscosity, surface tension and electrostatic forces on the system. At a constant distance and voltage between the infusion system and the collector, with varying the change in polymer concentration, bead free fibers were formed at rather high solution concentrations ($>$17.5%). The higher polymer concentration of the polymer increased the viscosity and electrical conductivity of the solution, thus improving the stretchability of the PAN fibers during electrospinning and resisting the formation of beads, as described in the previous paragraph. At constant voltage, the smallest diameter bead free fibers (350nm ± 70nm) were obtained at concentration of 19wt% and 0.5 ml/hr infusion rate. Also, the smallest fiber diameter was obtained when the average electric field intensity was about 1 kV/cm. Moreover, at constant concentration and distance, increasing applied voltage led to thicker fibers to form due to the stronger electrostatic attraction between the fiber and collector, leading to reduction in flight time, hence, reduction in stretch. The outcome of this study was beneficial in determining electrospinning parameters that we employed in our study.

Another factor which affects the morphology of electrospun fibers is the molecular weight of the polymer, which represents the length of polymer chain. Higher molecular weight often means greater chain entanglements. During electrospinning, as the solution leaves the needle tip, the chain entanglements increase the jet strength and thus allow for continuous and stable jet formation, from the needle tip to the collector [96]. The molecular weight of the polymer also affects the viscosity of the solution. On the other hand, overly high solution viscosity will hinder the process of infusion of the solution during electrospinning [97] and may cause the solution to form droplets at the needle tip. During its motion towards the collector, the polymer tries to conform to a least surface area configuration, thus trying to form beads. The viscosity of the solution works against this formation and resists sudden changes in the shape of the fiber. Low viscosity of the polymer causes formation of beads on the fiber [94, 98]. The beads on the fiber change from spherical to elongated in shape with increase in viscosity and when the viscosity reaches the optimum value, the beads completely stretch and beadless fibers forms. With increasing viscosity, the solution experiences difficulty in forming beaded configurations. Many researchers have also demonstrated that with increase in molecular weight of the polymer, the diameter of electrospun fiber also increases, possibly due to higher resistance of the fibers to drawing [90, 91, 93, 99, 100].

Alignment of electrospun nanofibers: Certain applications such as tissue engineering [101] and as load carrying members using continuous nanofiber composites require aligned nanofibers. Certain types of collectors like a solid rotating cylinder, split electrodes, rotating disc collector, rotating wired drum collector have proven to be advantageous (Figure 2.4). Cylinders or rotating drum collectors (Figure 2.4(a)) can be solid or wired in design. The rotating velocity of the cylinder allows the fibers to be collected in the direction of rotation. Using the solid cylinder only a small degree of overall alignment could be achieved. The solid drum was modified by Zussman [102], to a rotating disc with a tapered edge. The tapered edge caused concentration of charges, depositing fibers at the edge, parallel to each other and along the circumference of the disc. The rotational velocity (also known as take up velocity) played a role in fiber alignment and properties. Fibers in the form of narrow ribbons, several centimeters in length were formed using the rotating disc collector (Figure 2.4(b)).

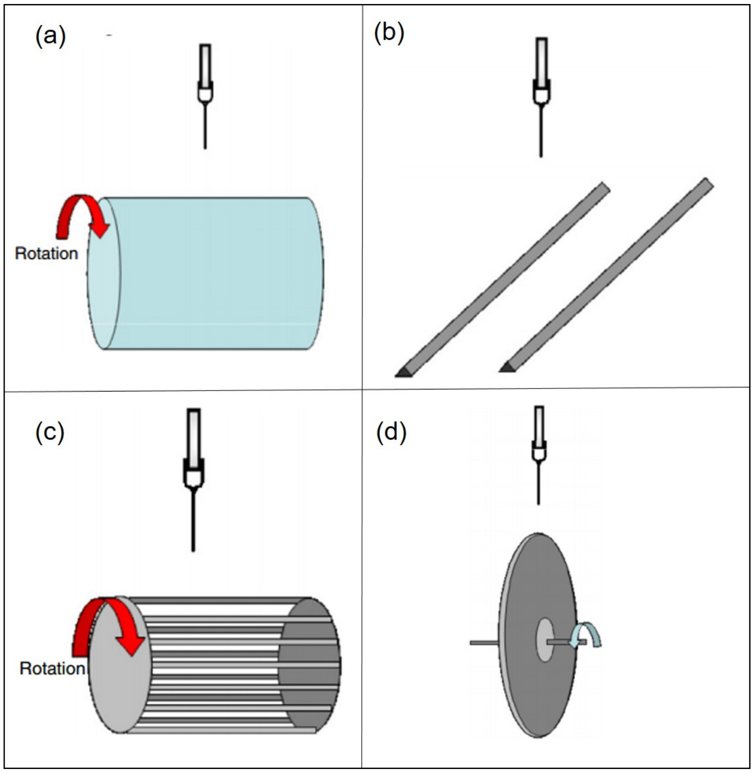

Figure 2.4: Types of collectors (a) rotating drum, (b) split electrode [15], (c) rotating wire drum [16], (d) rotating disc [17]

A modification combining the split electrode and rotating cylinder method led to the rotating wired drum collector (Figure 2.4(c)). This approach combines the benefits of rotational velocity of the drum and the split electrodes to form highly aligned fibers between the wires. Mats of nanofibers can be formed using this method [16].

Molecular alignment: The electrospinning jet experiences high electromechanical elongational and shear forces. These forces draw the jet and thus, enhance the chain alignment in the jet. Moreover, solvent evaporation and solidification of the fiber inhibits the chain relaxation in the fibers, leading to improved molecular alignment in fibers formed by the electrospinning process. In large diameter fibers an outer skin layer of highly ordered chains was observed [103]. This skin-core structure of electrospun polymer fibers is attributed to the rapid evaporation of the solvent from the surface, causing the chains to remain aligned. Electrospun polystyrene fibers showed isotropic nature above 2.5 m diameter, however, below this diameter the orientation of the fibers increased exponentially with reduction in diameter [18]. A schematic representing the structure of the fiber and the chain orientation in the skin and core section, as proposed by Richard-Lacroix and Pellerin is seen in Figure 2.5. During electrospinning, thinning of the fiber is essential, as this will assist with evaporation of solvent throughout the fiber thickness. In thick fibers, evaporation initiates at the surface first and solidifies the chains in aligned configuration. However, moving towards the center of the fiber, evaporation is slower, and as a result the chains get sufficient time to relax, leading to less oriented and more amorphous structure. It is expected that with smaller fiber diameters, this evaporation will be quick such that the chains throughout the fiber will remain aligned, leading to nanoscale diameter fibers with enhanced properties.

In a study on the relationship between PAN nanofiber diameter and strength on take up velocity of the rotating disc collector, Moon and Farris [19] found that keeping all other parameters the same, increasing the take up velocity from 4.8 m/s to 12.3 m/s led to a reduction in fiber diameter from $\approx$500nm and $\approx$300nm. Strength of yarns made with fibers spun at various take up velocities showed an optimum take up velocity at 9.8 m/s for PAN nanofibers and their carbon nanofiber yarn counterparts (Figure 2.6). The initial increase in strength with take up velocity was attributed to improvement in molecular orientation of the nanofibers during electrospinning. Also, the increase in alignment led to reduction in diameter and diameter distribution of the nanofibers. In the case of high take-up velocity,

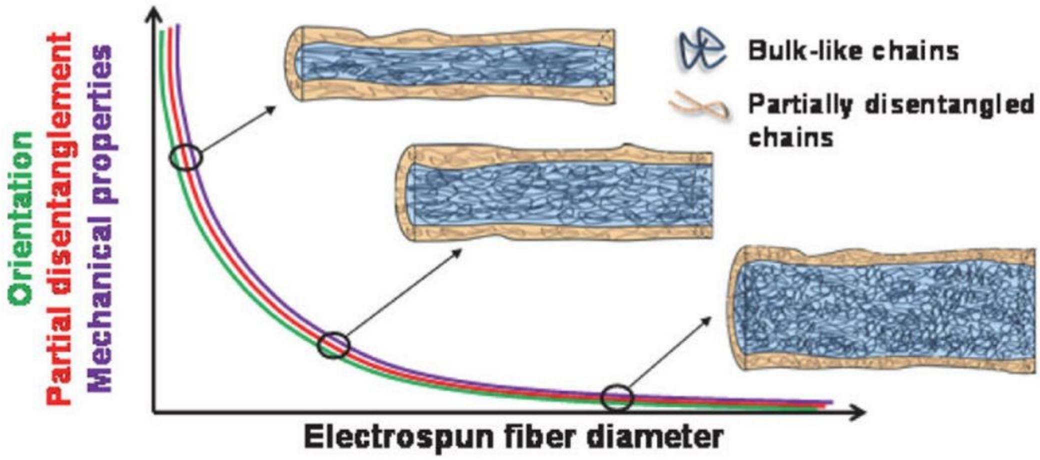

Figure 2.5: Schematic showing chain orientation in fiber with fiber diameter [18]

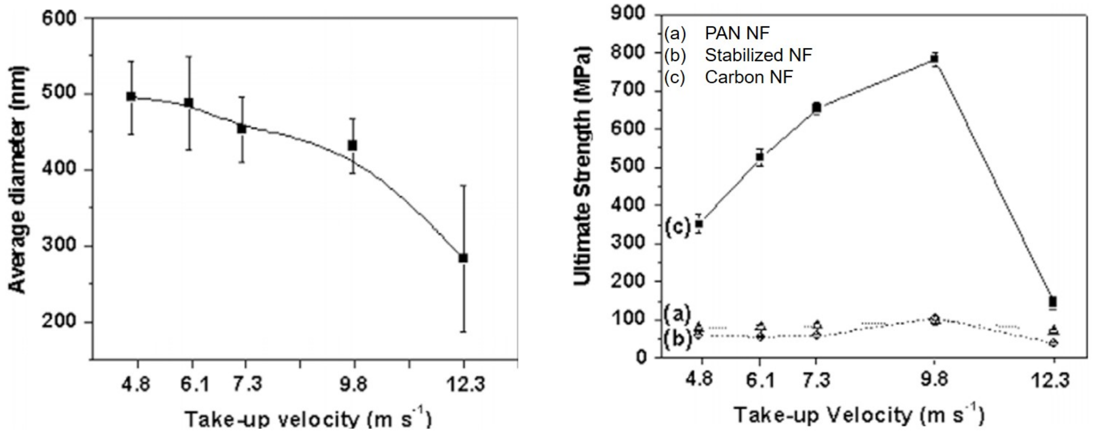

Figure 2.6: (a) Change in diameter with take up velocity of disc collector, (b) strength dependence of PAN, stabilized-PAN and carbon nanofibers with take up velocity of disc collector [19]

the fibers tend to break once they reach the collector causing the molecular chains to recoil and become less aligned. Due to higher number of chain ends, the possibility of bond ruptures is higher on heat treatment, causing the fibers to have lower strength than the fibers produced using lower take up velocities.

Thus far, we have discussed improvement in molecular orientation in nanofibers due to electrospinning parameters alone. This improvement is limited due to fast solvent evaporation which suppresses chain mobility and prevents further chain alignment. Therefore, post-spinning methods must be adopted to further align molecules. The next section discusses improvement in molecular orientation and crystallinity by hot drawing which also drastically changes mechanical properties of the fibers.

2.1.2 Hot Drawing

Conventionally, carbon fibers are made from precursor materials that are hot drawn using the method patented by Phillips and Johnson [60, 104]. In this method, fibers are stretched using constant load while heated to 135°C for five minutes. The T_g of PAN is around 95°C. At temperatures below T_g, the amorphous polymer is brittle and the polymer chains are not free to move. At temperatures above T_g, the chains obtain energy to move and can recoil and slide over each other. At these temperatures, the polymer shows ductile behavior. Stretching of the polymer at temperatures greater than T_g is dependent on the loading rate. At low loading rates, the polymer chains have sufficient time to uncoil and move. However, after a small amount of stretch, the recoil energy of the chains balances the stress experienced during loading and the fiber stretch reaches equilibrium. Beyond this, additional stretch can be achieved by employing a careful combination of temperature and applied stress. At high loading rates, the polymer chains have insufficient time to move, and cause breakage in the fiber instead of elongation. For the molecules to move with respect to each other above T_g and to enable elongation, it is important that the time taken by the polymer to stretch is less than its relaxation time. In our study the limiting values of applied stress for the molecular chains to uncoil and hence for the fibers to elongate was found to be 15MPa and 20MPa respectively, at a temperature of 135°C.

It is clear that improvement in molecular orientation of the nanofibers along the axis enhances its mechanical properties such as strength and modulus [18, 19, 61, 105, 106]. However, the fabrication methods used to produce polymer fibers such as melt spinning and electrospinning provide limited amount of orientation in the fibers. As such, further improvement in the orientation must be obtained using post processing techniques such as wet drawing in boiling water or in saturated steam [20, 44], drawing in a bath of diluted Copper Chloride ($CuCl_2$)[45] or DMF solutions [46] and to dry stretch in nitrogen atmosphere or air at elevated temperatures [47, 48, 49]. PAN has molecular dipole-dipole bonds that inhibit the stretching and sliding of the chains. The stretching methods used aim to reduce the dipole interactions between the chains, allowing them to slide over each other. Moreover, plasticizers such as $CuCl_2$, DMF and water reduce these interactions and allow the fibers to stretch. Regardless of the method, hot drawing is typically carried out at temperatures above the T_g of the polymer and below the temperature at which it begins to chemically alter (cyclize in case of PAN) (95°C-220°C).

Each method of drawing has its own advantages and drawbacks and permits a limited amount of stretch in the fiber. DMF is a good solvent for PAN and can dissolve PAN from the fiber causing the fibers to fuse together during stretch. In the case of water and steam stretch, there is a possibility of formation of pores on the fiber surface due to the diffusion of water in the fiber. Drawing in air at elevated temperatures uses heat to enhance chain mobility and thus requires higher temperature for hot drawing than the methods using a solvent and multi-stage drawing process may be required. However, this method permits improvement in molecular orientation without the addition of a chemical plasticizer or moisture, thus allowing better control of properties. In the process of stretching PAN nanofibers, it is important to keep in mind the end goal of the stretch process, which in our case is to create high strength and modulus carbon nanofibers by improving the molecular orientation of the PAN nanofibers. While hot drawing improves the molecular orientation of the fibers, it is important to understand the effects of hot drawing on crystallinity of the nanofibers and the effect on the subsequent processing, morphology and properties of carbon nanofibers obtained.

As stated earlier, at industrial scales as well, carbon fibers are also manufactured by carbonizing precursors which have been subjected to hot drawing. However, the draw ratios reported for macroscale fibers are not achievable by nanofibers possibly due to the small diameters. As discussed previously, smaller diameter fibers have improved orientation of the chains during the electrospinning as compared to fibers with larger diameters [18]. As such, one hypothesis is that the improvement in alignment achievable via hot drawing is less in smaller diameter fibers due to the presence of already partially aligned chains in the latter. In other words, smaller diameter fibers (and nanofibers) are often fabricated by drawing polymer fibers/jets, during which chains can become partially aligned with the drawing direction (which is the same as the fiber axis). Also, homopolymer PAN has hydrogen bonds between chains which inhibits the chains from gliding over each other [107]. On the other hand, copolymers of PAN, such as methyl acrylate (MA) and itaconic acid (IA), typically used in industrial scale microfiber [108] fabrication facilitate movement of the chains.

By applying the hot drawing to nanofibers, some researchers have been able to obtain elongation upto six times the original fiber length. Hou et. al [109] achieved 55% and 156% improvement in strength and modulus respectively of hot drawn PAN nanofiber sheets. In a study performed by Song et. al. [106], electrospun PAN nanofiber sheets were hot stretched using the method by Johnson and Philip [60, 104], and subsequently carbonized at 1000°C. Approximately five fold improvement was observed in modulus and tensile strength of the carbon nanofiber sheets.

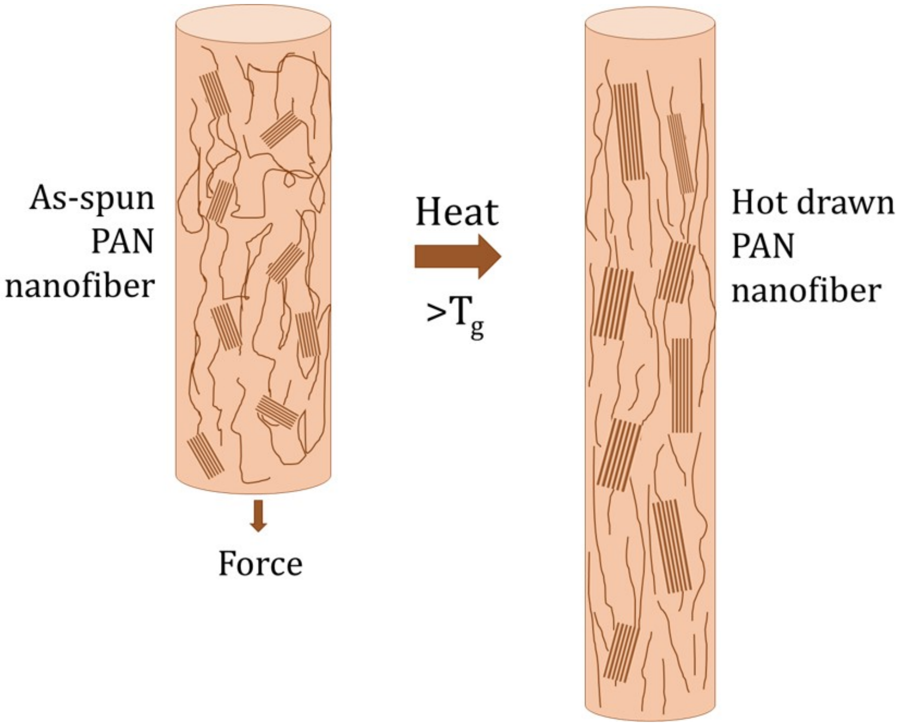

Figure 2.7: Schematic of hot drawing process

The most frequently used approach to hot-draw fibers is the one proposed by Johnson and Phillip [60, 104]. Figure 2.7 shows a schematic of the process. In this technique, the PAN nanofiber ribbon is fixed on a stationary rod at one end, and hung vertically. A weight is attached to the ribbon on the free end. The weight exerts a force on the ribbon causing the ribbon to stretch when heated to temperatures above T_g, typically at 135°C. At elevated temperatures, the molecules gain enough mobility to move passed each other, get uncoiled and thus nanofibers get elongated. Our study uses a modified hot drawing method (multi-step hot drawing) for the nanofibers to achieve maximum draw ratio, which is described in detail in Section 2.2.2.

While here have been studies on hot drawing of polymer nanofibers to improve their molecular orientation, these efforts often do not describe sufficient details of the morphology of the fibers through this process. This is important to understand the correlation between the processing parameters (such as hot drawing ratio, temperature of drawing), morphology and mechanics of fibers.

Effect of molecular weight on hot drawability: Kobayashi [20] studied the effect of molecular weight on the hot drawability of PAN.

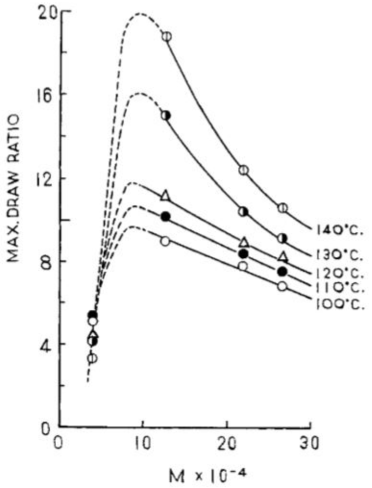

Figure 2.8: Effect of molecular weight on hot drawability at elevated temperature [20]

The fibers obtained after spinning were washed with nitric acid and hot stretched in a bath of hot water and saturated steam, at 100°C-140°C. His studies show that the draw ratio steadily increases from MW 25,000 g/mol to 80,000 g/mol fibers and then has a negative linear correlation with increase in molecular weight. Interestingly, for all molecular weights, the same trend was observed with respect to the draw ratio, and maximum draw ratio was obtained for fibers made from 80,000 g/mol polymer drawn at 140°C (Figure 2.8). The non-monotonic variation of the drawability with MW is likely rooted in the density of chain entanglement which scales linearly with MW. In other words, an optimum degree of chain entanglement is required to prevent fiber failure during drawing, while higher entanglement density does not allow chains to move freely passed each other to accommodate fiber drawing.

This work also concluded that the force required for stretching did not depend on the molecular weight of the polymer.

2.2 Experimental Work

The electrospinning configuration using a rotating drum collector is shown in Figure 2.9. The setup is placed in a humidity chamber to control the temperature and humidity of the electrospinning surrounding. In the work presented here, the drum collector shown in the figure is replaced with a rotating disc collector, shown in Figure 2.10. It consists of a syringe infusion system, a rotating disc collector, a high voltage power supply between the syringe and the collector and a power supply to rotate the disc. The syringe infusion system and the collector are enclosed in a humidity chamber, with the humidity of surrounding environment maintained at ≈25% RH.

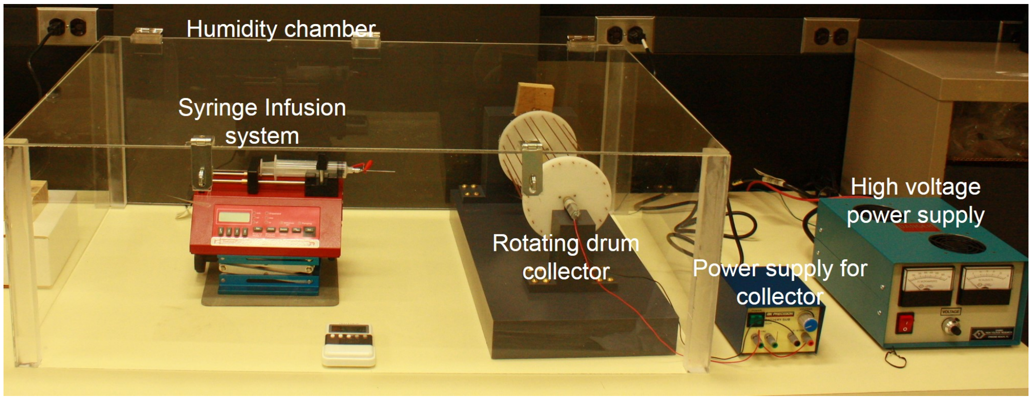

Figure 2.9: Electrospinning setup with a rotating drum collector

Figure 2.11 shows the formation of nanofibers during the electrospinning process. The breakup of the polymer solution from the tip of the needle leading to formation of

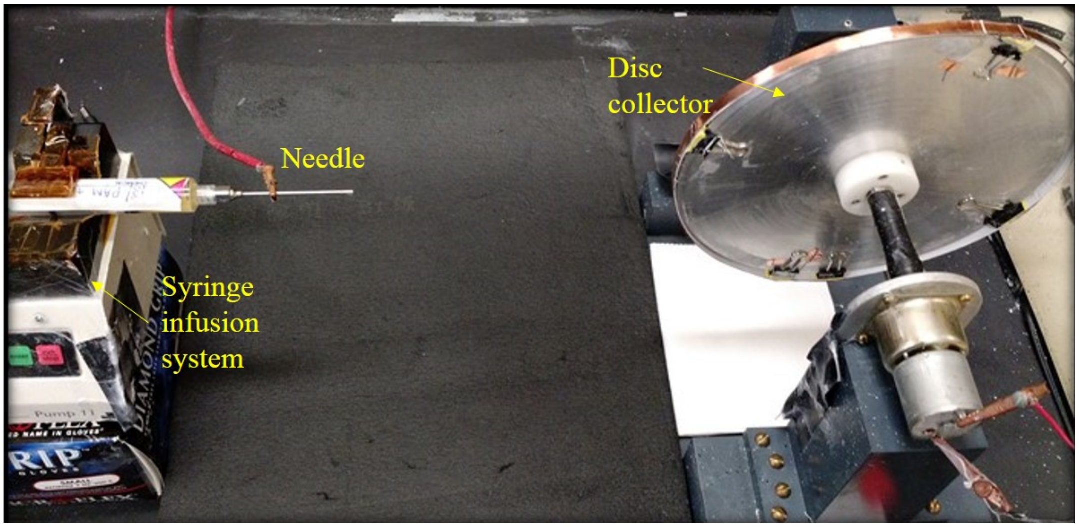

Figure 2.10: Electrospinning setup with a rotating disc collector

nanofibers is clearly seen in the figure.

PAN and DMF used in this study were purchased from Sigma Aldrich. A solution of PAN powder (M.W. 150,000 g/mol) was dissolved in DMF using a magnetic stirrer. The solution was stirred overnight to ensure homogeneity. The solution of PAN and DMF was poured into a syringe with a needle of 0.85 mm inner diameter. The setup was placed in a humidity chamber.

As seen in Figure 2.10, an aluminum disc collector was used to collect the PAN nanofibers. The disc collector had a tapered edge to create a high density electric field in order to direct the fibers on the rotating edge. For easy removal of the fibers from the disc, the circumference of the disc was covered with copper tape. The nanofibers obtained were in the form of ribbons, approximately 0.8cm width $\times$ 10μm thick $\times$ 55cm length, containing millions of fibers with diameters in the submicron range.

Figure 2.11: Breakup of jet during electrospinning leading to formation of nanofibers

2.2.1 Effect of Electrospinning Parameters on Fiber Morphology

In this section, the effect of concentration on PAN in DMF, i.e. solution concentration and take-up velocity of the collector are discussed.

Effect of solution concentration on fiber morphology: The first step in this work was to obtain a set of electrospinning processing parameters to obtain beadless PAN nanofibers. Electrospinning factors leading to bead formation have been discussed in Section 2.1.1 of this chapter. To this end, four different solution concentrations were studied.

In each case, approximately 50 readings of fiber diameter were taken using the Scanning Electron Microscope (SEM). An example of the SEM images of the electrospun PAN nanofibers is seen in Figure 2.12. As seen in the figure, at 9wt% PAN in DMF, a large number of beads were present in the fiber. By increasing the solution concentration to

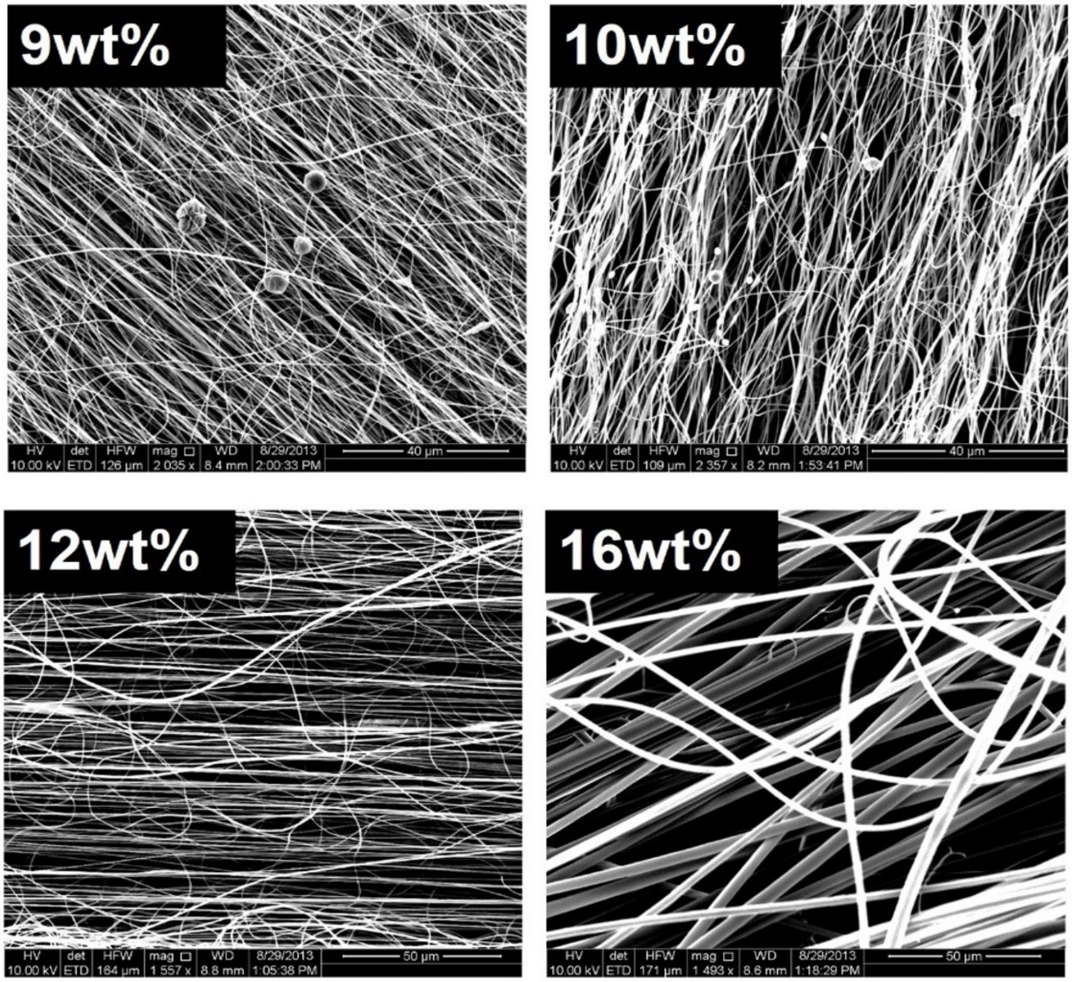

Figure 2.12: SEM Images of PAN nanofibers electrospun at different concentrations of PAN in DMF

10wt%, no significant change in the morphology of the fiber or fiber diameter was observed and fibers with beads were formed. However, by further increasing the solution concentration to 12wt%, the number of beads was reduced, lower number of broken fibers and fibers with more uniform diameter along their length were obtained. In addition, at 16wt%, beadless fibers were obtained with uniform diameter across the fiber length and the fiber showed less surface undulations.

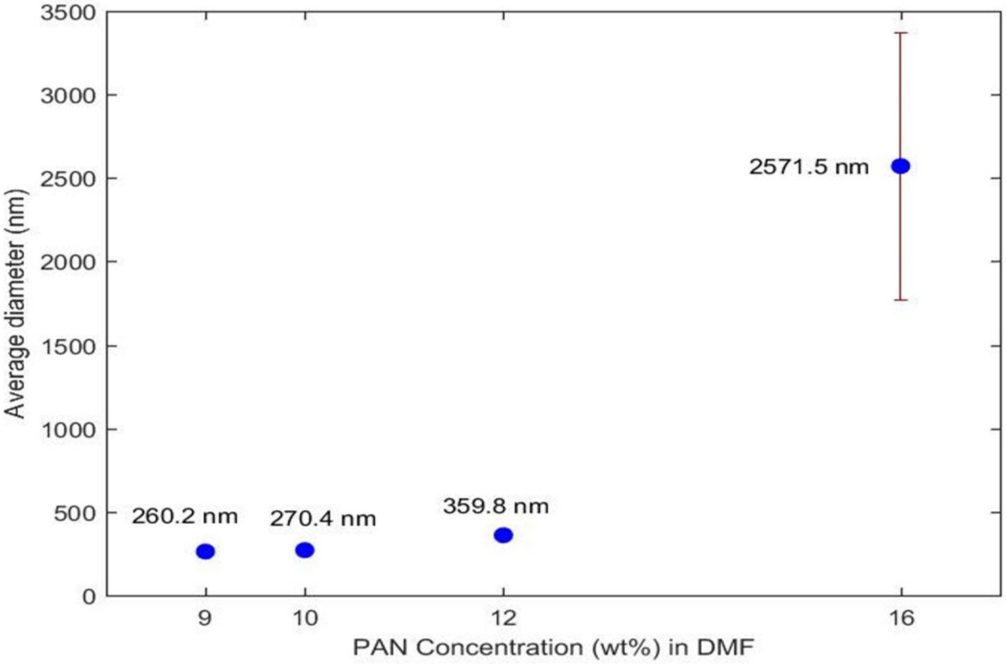

Figure 2.13: Average diameters of PAN nanofibers electrospun using different concentrations of PAN in DMF

The average diameter of the fibers increased from 360nm to 2.57μm as the solution concentration was increased from 9wt% to 16wt% (Figure 2.13). Higher concentration of PAN also caused more scatter in the fiber diameters. Less than 5% scatter in fiber diameters was observed in the case of 9wt%, 10wt%, 12wt% PAN in DMF, while for the case of 16wt% PAN in DMF, the scatter in diameter was $\approx$20%. Increase in concentration of PAN caused the viscosity and net charge density of the solution to increase. At lower viscosity, higher amount of solvent molecules and fewer chain entanglements caused the surface tension to be the dominant force in the electrospinning process. The surface tension favored reduced surface area and spherical or oval beads due to the low energy configuration. This behavior was also observed by other authors [94, 98]. Moreover, we observed that increasing the solution concentration tends to eliminate the beads.

According to Ramakrishna [33], at higher viscosities, larger number of chain entanglements are present in the solution and the charges on the jet will enable better stretch of the solution, the beads become smaller and more spindle-like, while the diameter of fibers become smaller. Moreover, at higher concentrations, higher viscosity of the solution poses greater resistance to stretching of the solution, leading to larger diameter fibers [91].

Considering the desire for diameter uniformity, narrow diameter distribution and formation of bead-free fibers, nanofibers fabricated from 12wt% PAN in DMF was chosen as the precursor of CNFs for further studies.

Effect of take-up velocity on fiber morphology: The electromechanical forces applied on the electrospinning jet can partly align the chains with the fiber axis. However, the rapid solvent evaporation during electrospinning will reduce chain mobility, which in turn limits molecular orientation that can be achieved through electrospinning. To induce and enhance chain alignment in the as-electrospun nanofibers, we electrospun PAN from a PAN in DMF solution on a rotating disk. The mechanical forces on the jet as it is being collected and drawn by the disk is expected to induce elongational and shear flows on the jet and align the chains. We fabricated PAN nanofibers with 50 rpm, 500 rpm and 1000 rpm corresponding to disk tip (pick up) velocity of i.e. 0.5 ms^{-1}, 5.3 ms^{-1} and 10.6 ms^{-1}, respectively.

The effect of disc speed on the alignment of the chains was analyzed using Polarized Fourier Transform Infrared Spectroscopy (FTIR). For this purpose, the Thermo Nicolet 380 FTIR spectrometer was employed with a manual infrared (IR) polarizer obtained from PIKE Technologies.

For each take-up velocity, three bundles of aligned electrospun PAN nanofibers were analyzed with light polarizations parallel and perpendicular to the fiber axis. Polarized FTIR spectra were used to study the orientation of the nitrile ($C \equiv N$) group with respect to the fiber backbone.

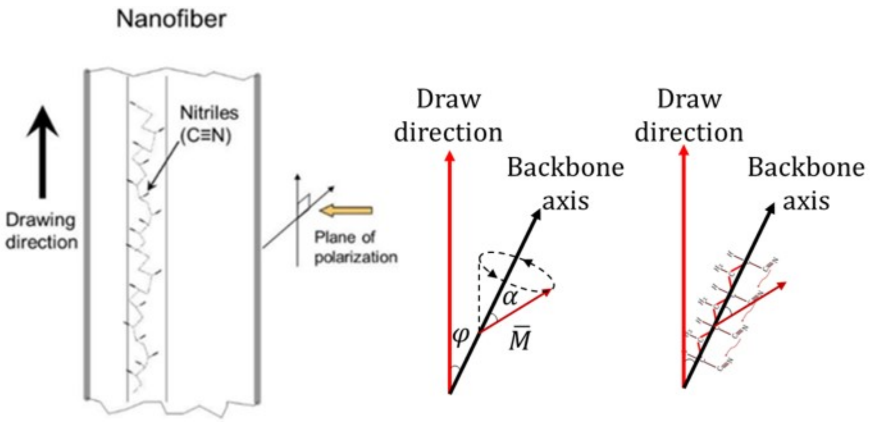

Figure 2.14: Schematic of molecular orientation in PAN

A schematic of the molecular chains in PAN with the molecular chains of PAN aligned predominantly in the fiber direction is shown in Figure 2.14. The C $\equiv$ N (nitrile) groups are oriented at 73° to the backbone of PAN. The level of molecular orientation of the fibers was analyzed using polarized FTIR. The peak at 2243 cm^{-1}, representative of the nitrile group in the FTIR spectrum was used as an indication for the amount of orientation. The degree of orientation is calculated using Herman's orientation factor as in Equations 2.1 and 2.2.

$$f = \frac{3 < cos^2\phi > -1}{2} \tag{2.1}$$

$$f = \frac{(D-1)(D_0+2)}{(D_0-1)(D+2)} \tag{2.2}$$

where,

$$D = \frac{A_{||}}{A_{\perp}}$$

$$D_0 = 2cot^2\alpha$$

For the purpose of quantifying molecular orientation of PAN nanofibers, focus is placed on the 2243cm^{-1} (C $\equiv$ N) region in the FTIR spectra taken at polarizer angles of 0° ($||$) and 90° ($\perp$). In Figure 2.15, the blue curve is taken from the FTIR spectrum using 0° polarizer and the red curve is taken from the FTIR spectrum using 90° polarizer. From Equation 2.2, $A_{||}$ is the magnitude of the 2243cm^{-1} peak in the 0° spectrum and $A_{\perp}$ is the magnitude of the 2243cm^{-1} peak in the 90° spectrum. The spectra are taken in absorbance mode (A) of the FTIR and converted to transmittance mode (T) using the FTIR software. Baseline correction is not carried out for the entire spectrum. However, for the region being measured, as seen in Figure 2.15, a line is drawn at the base of the peak and height from the horizontal baseline (black line in Figure 2.15) to the maximum of the peak (i.e. peak height) is measured.

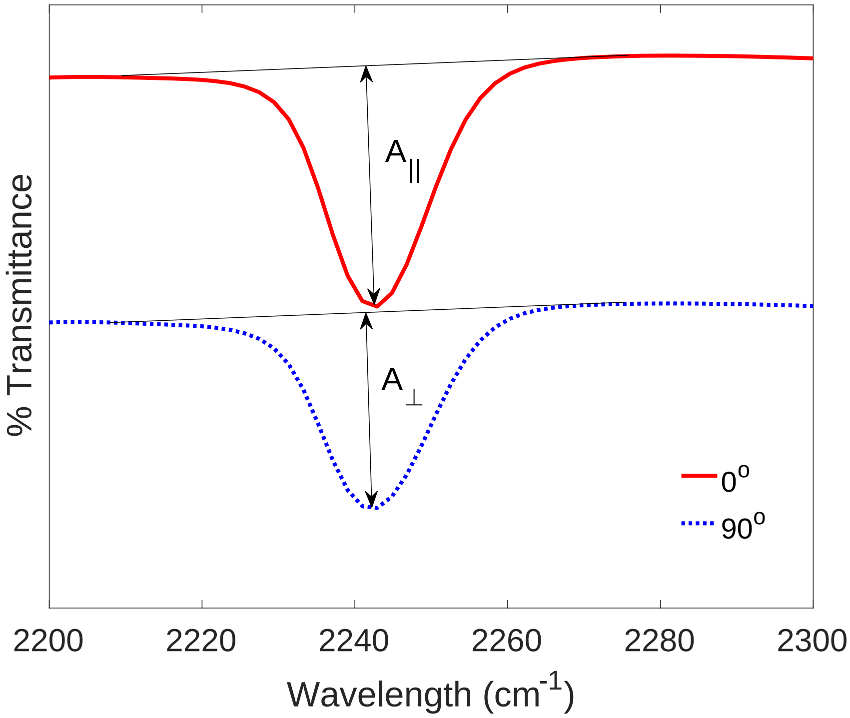

Figure 2.15: FTIR curve showing measurement of $A_{||}$ and $A_{\perp}$

The Herman orientation factor f ranges from 1 when all the chains are aligned with the fiber axis, to -0.5 when the chains are perpendicular to that. For a completely random polymer, the Herman orientation factor is 0. The angle is the angle between the nitrile group and the backbone axis and ϕ (as seen in Figure 2.14) is the angle between the draw direction or the fiber direction and backbone axis. $A_{||}$ is defined as the magnitude of the nitrile group (2243 cm^{-1}) at 0°, and $A_{\perp}$ is the magnitude of the nitrile group at 90°.

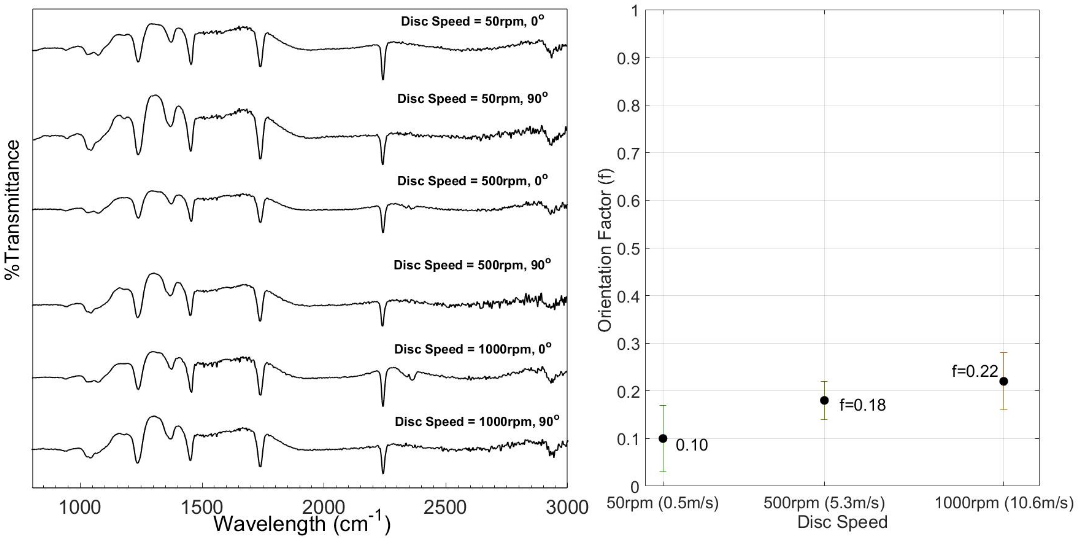

Figure 2.16: (a) Polarized FTIR for PAN nanofibers electrospun at disc speeds of 50 rpm, 500 rpm, 1000 rpm (0.5m/s, 5.3m/s and 10.6m/s, respectively), (b) Herman's orientation factor f as a function of disc speed

Using Equation 2.2 and magnitudes of the peak intensity of the C $\equiv$ N peak in Figure 2.16, Herman's orientation factor f was calculated [110]. This value is used with Equation 2.1, to obtain the overall orientation of the molecules with respect to the PAN fiber (angle ϕ). That values obtained are tabulated in Table 2.2.

Modifying only the take-up velocity of the disc, provided approximately 19$\%$ improvement in the orientation of the molecules with respect to fiber axis. The angle between the

Take-up velocity (m/s)	f	ϕ
0.5	0.10 ± 0.07	$50.8° \pm 2.7°$
5.3	0.18 ± 0.04	$47.7° \pm 1.5°$
10.6	0.22 ± 0.06	$46.1° \pm 2.3°$
% Improvement at 10.6m/s as compared to 0.5m/s	120%	9.3%

Table 2.2: Herman's orientation factor f and angle ϕ

polymer backbone and the draw direction i.e. the fiber axis reduced by 2 degrees. Further increasing the take up velocity of the disc caused the fiber to break during the electrospinning process. This analysis showed that the molecular alignment achievable using electrospinning is limited. This is likely due to the fast solvent evaporation during electrospinning and the consequent loss in chain mobility, which prevents chain alignment via mechanical forces of the rotating disk. As a result, we turned to already established methods for further improvement in alignment of PAN fibers and adopted them for nanofibers.

2.2.2 Hot Drawing

The method used in this study to align PAN chains in PAN nanofibers was patented by Philip and Johnson on microfibers [60, 104] and has been effectively used to enable stretching of fibers. This method utilizes heat to energize PAN chains and to enable the movement of PAN molecules. In this method, the fiber is heated above its T_g to enhance chain mobility, thus allowing them to uncoil and align. To implement hot drawing of PAN nanofibers, nanofiber ribbons obtained from electrospinning were mounted on a fixed arm with tacky tape on one end of the fiber. The other end (lower end) of the fiber also had tacky tape which was used as a grip to apply the load. The tacky tape mitigated the stress concentrations arising from the grips and mimicked a continuous production line used in industry. The top end of the fiber was hung from a fixed arm, while the lower end had a hook and box arrangement to which weights were added to provide the force required

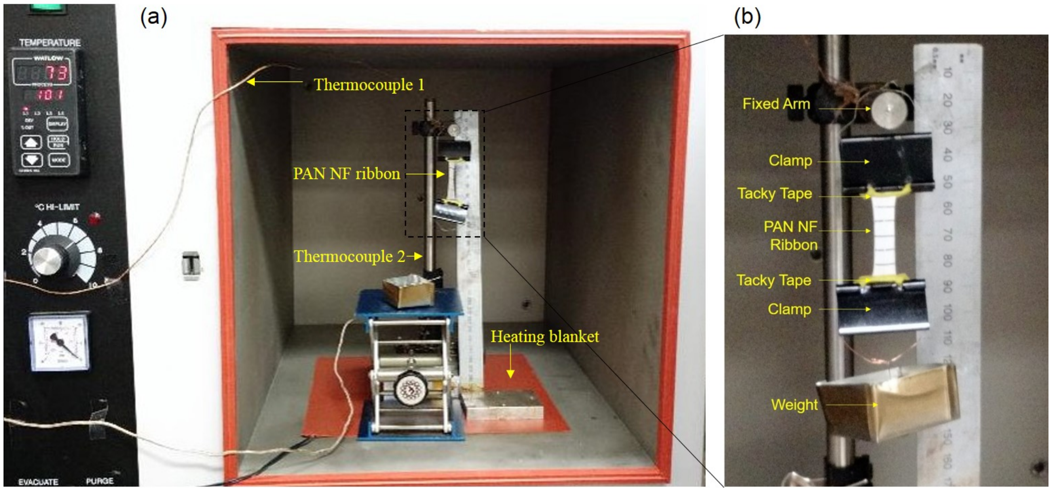

Figure 2.17: Experimental method to hot draw PAN ribbons

to stretch the fiber. The entire setup was placed in an oven as seen in Figure 2.17(a).The oven used had heating elements only on the inner top surface, which caused a temperature gradient in the oven. To overcome this, a heating blanket was placed on the bottom of the oven. There were two thermocouples in the oven, the top one was integral to the oven, and the second was placed close to the lower end of the ribbon. This setup ensured uniform temperature distribution through the entire length of the fiber. The setup to clamp the fiber for hot drawing is seen in Figure 2.17(b).

The glass transition temperature of PAN nanofiber used in this study was 99°C, as calculated using DSC (Figure 2.18). Above this temperature, the PAN chains will have the free volume required to coil/uncoil depending on the applied forces. The temperature of the oven was raised from RT to 100°C. At this temperature, a weight was placed in the container at the lower end of the fiber, applying a tensile force on the fiber and preventing the molecules from coiling. The force applied an engineering stress of 19MPa on the ribbon. As a result of the applied stress and elevated temperature, the nanofiber ribbon was stretched upto a maximum draw ratio of 4 (to 4x of its original length) at a temperature of 135°C. In this study, applied stress of 15MPa to 19MPa permitted elongation of the ribbon. At 135°C, applied stress of 15MPa caused a stretch of 1.5x on the fiber, and stress to 17MPa stretched the fiber to 2.5x. When stress of 20.5MPa was applied, at initial temperature of 100°C, it caused the ribbon to break almost instantaneously, and no higher temperatures or forces were tried. At a draw ratio of 4x, the linear density of the fiber reduced to $0.25\lambda_1$x, with λ_1x being the linear density of the as-spun fiber (draw ratio $= 1$).

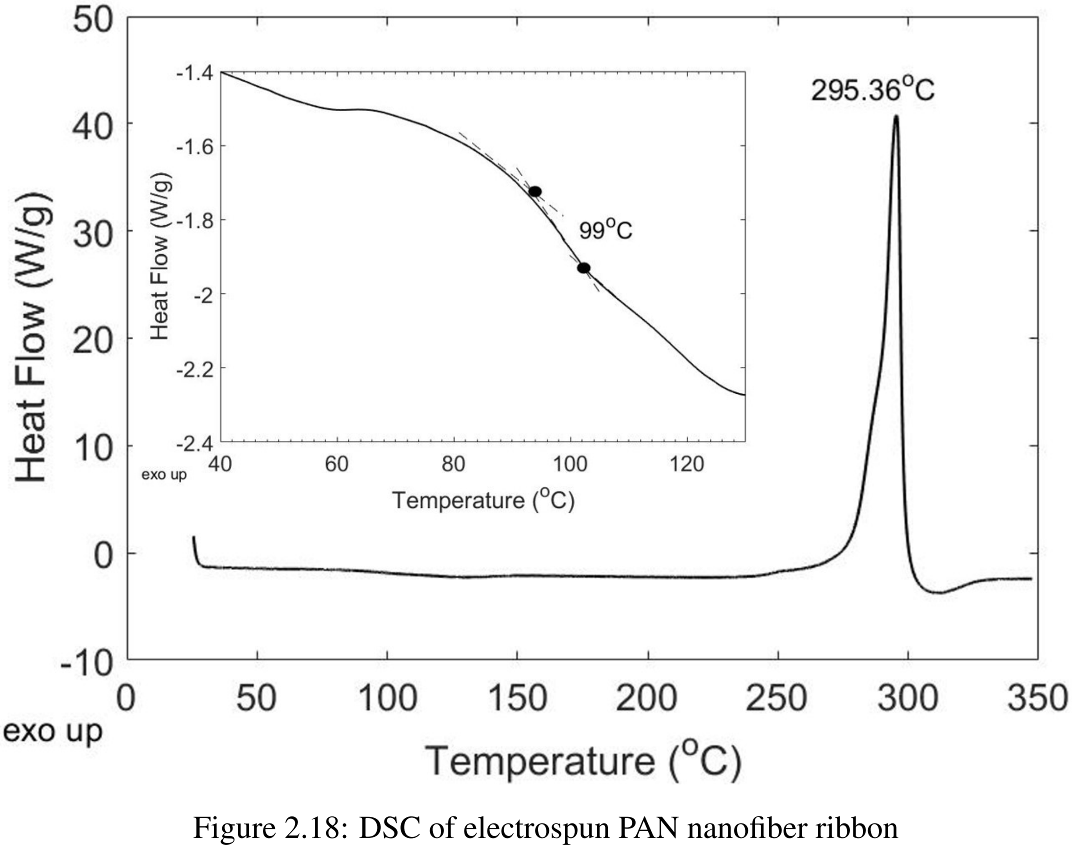

Figure 2.18: DSC of electrospun PAN nanofiber ribbon

In addition to the applied stress, the draw ratio was also a function of the temperature. At oven temperature of 120°C and 19MPa stress, the fiber was able to stretch only upto 2x. Further stretching at this temperature is potentially prevented by the residual entanglement between chains and the limited free volume of the chains achieved at this temperature. Higher temperatures can further increase the free volume of the chains and lower the interactions between them, facilitating further drawing. For instance, when the temperature is raised to 135°C at the same applied stress of 19MPa a stretch ratio of 4(x) was achieved.

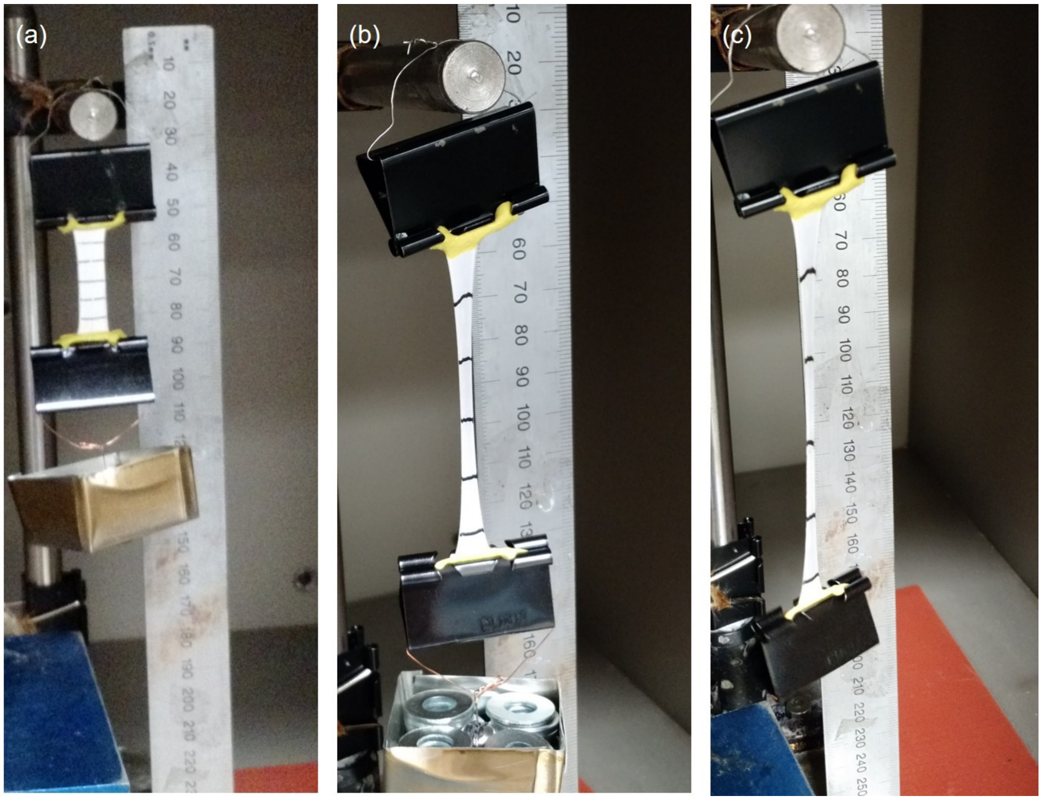

Figure 2.19: Experimental method to hot draw PAN ribbons

Figure 2.19(a) shows the fiber at the beginning of the hot draw stage, at 100°C when the force is just applied on the ribbon, Figure 2.19(b) shows the fiber when stretched to 2x and

Figure 2.19(c) shows the fiber in its final configuration of 4 times the original fiber length, '4x'. Markings are made on the fiber at distances of 0.5 cm apart, to ensure uniform stretch in the fiber. As seen in Figures 2.19(b-c), the regions in the middle portion of the fiber are uniformly stretched, while the regions near the grips experience unequal elongation. This is due to additional stress applied by clamping of the grips and heat transfer from the grips causing changes in the local temperature of the fiber. For further processing, fibers from the center sections of the ribbon are used. The three cases of '1x', '2x' and '4x' will be heat treated and tested to understand the role of hot drawing on the final morphologies and properties of single CNFs.

Characterization of hot drawn PAN nanofibers using polarized FTIR: Qualitative and quantitative assessments were both made on hot drawn PAN nanofiber ribbons to understand the effect of hot drawing on the nanofibers. Qualitative assessments were through polarized FTIR and X-Ray diffraction (XRD). Quantitative assessments of improvement in molecular orientation in nanofiber ribbons were made using tensile tests on PAN and is discussed in Section 2.2.3. The effect of hot drawing on the mechanical properties of the derived carbon nanofibers is discussed in Chapter 4.

Hot Draw Ratio	f	ϕ
1x	0.22±0.06	46.1°± 2.3°
2x	0.42±0.05	38.5°± 1.9°
4x	0.55±0.05	33.2°± 2.1°
% Improvement at 4x as compared to 1x	150%	28%

Table 2.3: Herman's orientation factor f and angle of backbone axis with fiber axis ϕ

The FTIR spectrum of hot drawn fibers was collected in a manner similar to that discussed in Section 2.2.1. Using the equation for Herman's orientation factor f in Equation

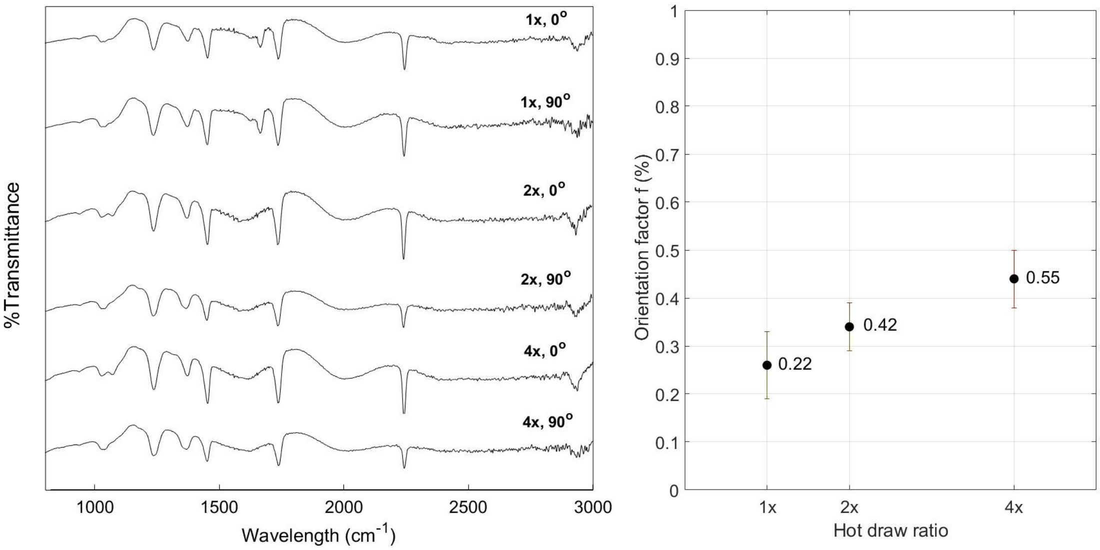

Figure 2.20: (a) Polarized FTIR for PAN nanofibers at hot draw ratios 1x, 2x, 4x, (b) orientation factor f as a function of draw ratio

2.2 and the magnitude of the C $\equiv$ N peak at 2243 cm^{-1}, the Herman's orientation factor was calculated for the hot drawn fibers, seen in Table 2.3 and Figure 2.20. Improvement in alignment (Herman's orientation factor) from 0.22 to 0.55 by hot drawing as electrospun samples to draw ratio 4.

Characterization of the crystalline structure of hot-drawn PAN using x-ray diffraction (XRD): X-ray diffraction experiments were carried out on PAN nanofibers in order to study the development and alignment of the crystalline domains in the nanofiber as a result of hot-drawing. A schematic of the crystalline and amorphous domains in the nanofibers is shown in Figure 2.21.

Wide angle XRD was carried out using D8 Discover with General Area Detector Diffraction System (GADDS) (2D X-ray diffraction) and powder diffraction was performed on the D8 Advance system.

The powder diffraction plots for the cases of 1x, 2x and 4x PAN nanofibers is seen in

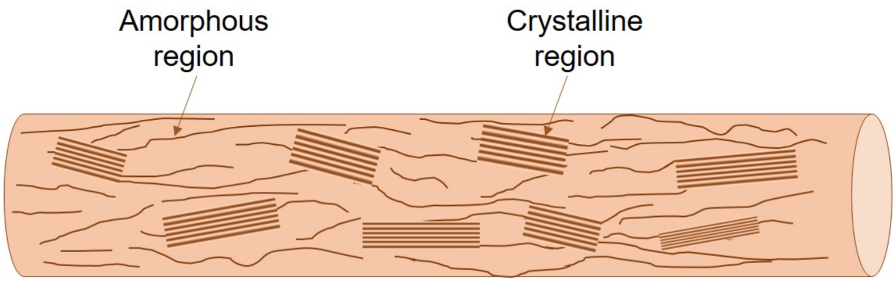

Figure 2.21: Schematic of crystalline and amorphous regions in a polymer

Figure 2.22.

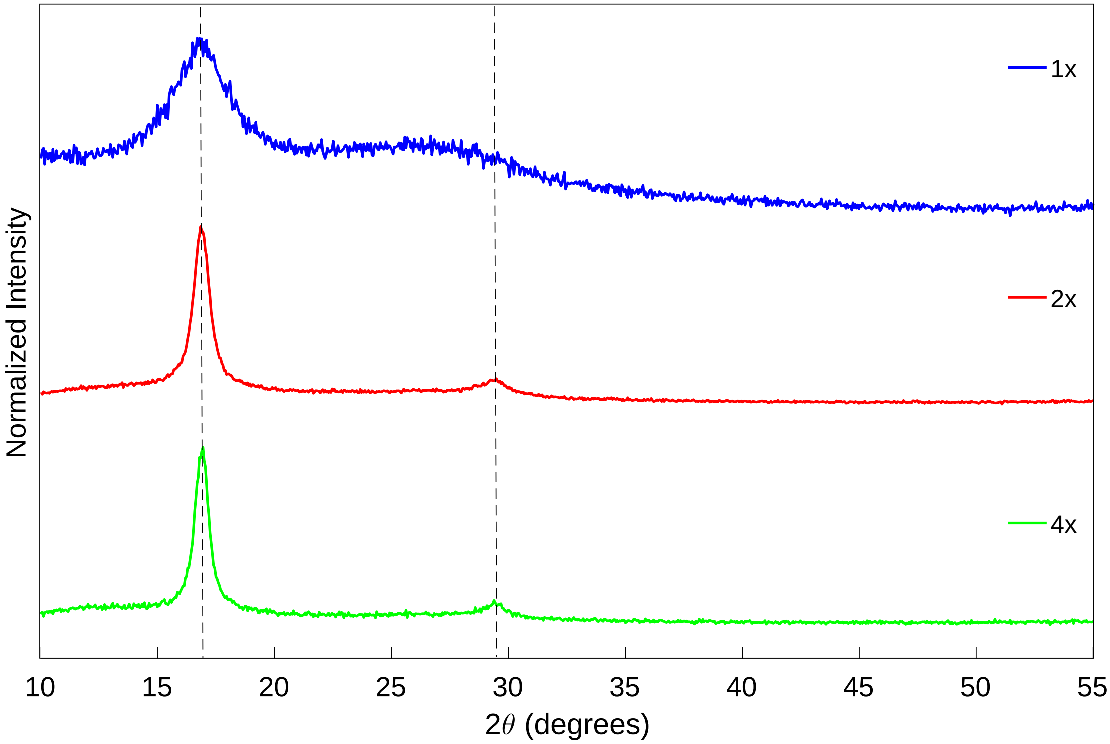

Figure 2.22: Powder X-Ray diffraction of 1x, 2x and 4x hot drawn PAN nanofibers

The X-ray powder diffraction pattern of as-electrospun PAN nanofiber ribbons shows a broad peak at $2\theta = 17°$. This peak in the hot-drawn samples becomes very sharp, and a second peak emerges at 2θ = 29.5°. The crystalline nature of the broad peak in the as-electrospun samples is subject to speculation, while the sharp peak in hot-drawn samples leaves no doubt that crystalline domains have formed/grown as a result of hot-drawing.

Calculation of amount of crystallinity: The powder diffraction X-ray data obtained for the as-spun and hot drawn nanofibers was used to calculate the amount of crystallinity in the nanofiber. The percentage of crystallinity gives the amount of crystallinity in the fiber in relation to the amorphous regions. This value is calculated using the Equation 2.3, given below:

$$Percent\ crystallinity = \frac{A_{cr}}{A_{am} + A_{cr}} \tag{2.3}$$

where A_{cr} is the area under the crystalline peak at $2\theta = 17°$ (Figure 2.23), and A_{am} is the area of the amorphous region. Since the peak at $2\theta = 29.5°$, is wide, it was not considered to be a peak arising from crystalline structure for purposes of this calculation.

Using Peakfit, the baseline was extracted from the powder diffraction data, as shown with the red line in Figure 2.21(a). The area under the peak at $2\theta = 17°$, highlighted in gray in Figure 2.21(b) is calculated as A_{cr}. The total area $(A_{am} + A_{cr})$ is the area under the entire curve in Figure 2.21(b). The percent crystallinity in the 2x and 4x nanofibers is tabulated in Table 2.4.

Hot Draw Ratio	**% Crystallinity**
1x (as-electrospun)	20%
2x	43%
4x	49%

Table 2.4: Calculation of percent crystallinity

While no clear indication of crystallinity was found in the as-electrospun fibers,it was calculated to be approximately 20%. The degree of crystallinity of the 2x hot drawn PAN

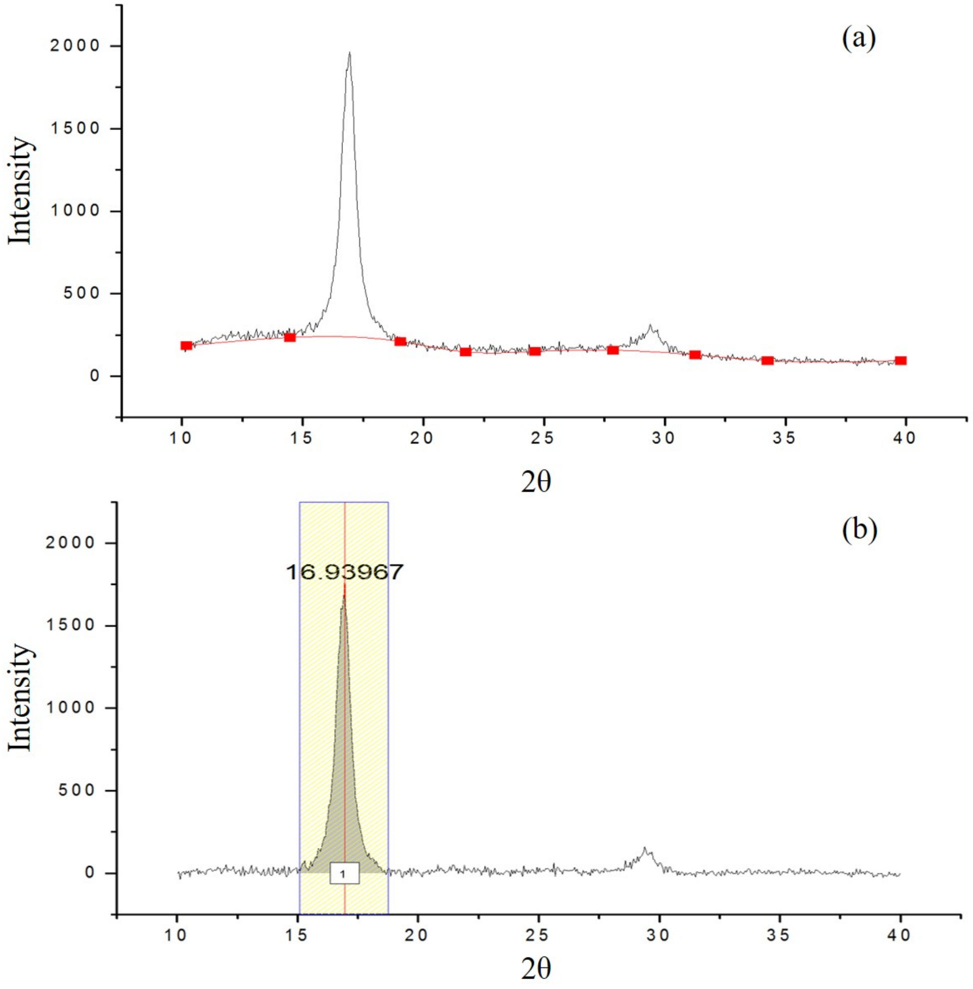

Figure 2.23: Crystallinity calculation for 4x hot drawn nanofibers

nanofibers was calculated to be 43% with a slight increase to 49% when hot drawn to 4x. Therefore, hot-drawing indeed enhanced crystallization in PAN. That can be explained by considering the fact that aligned PAN chains can get packed more efficiently, leading to the formation of crystals.

Calculation of interatomic spacing: The crystallographic distances associated with the peaks was calculated according to the Bragg's Law (Equation 2.4):

$$d_{hkl} = \frac{\lambda}{2sin\theta} \tag{2.4}$$

where d_{hkl} = Lattice spacing, λ_{XRD} = X-ray wavelength = 0.154nm, θ = Scattering angle, in degrees(°)

The peaks of $2\theta = 17°$ and $2\theta = 29.5°$ correspond to crystallographic distances of $5.3\dot{A}$ and $3.03\dot{A}$, respectively. The ratio of the crystallographic distances of the peaks is $\frac{5.3\dot{A}}{3.03\dot{A}} = 1.75$. This value, within the experimental uncertainties associated with identifying the exact location of peaks, is the same as $\sqrt{3}$ $(= 1.73)$, suggesting that the PAN structure takes a hexagonal structure arrangement as a result of hot drawing, in which each chain is confined within the boundaries of a cylinder with a radius of $3.03\dot{A}$, with cylinders been parallel to the fiber axis and hexagonally arranged within the fiber cross section. This structure has been described as "laterally ordered" crystallites with hexagonal packed "molecular rods" [111]. With this hexagonal arrangement of PAN chains, the two peaks correspond to (100) and (110) in the PAN crystalline structure (Figure 2.24).

Assuming that the PAN has a hexagonal lattice structure, the peak at 2θ = 17° is due to X-ray scatter from the 100 planes with $d_{100} = 5.3\dot{A}$. The existence of the 100 plane in the as-electrospun samples indicates some initial orientation of PAN chains, arising from electrospinning (in line with the polarized FTIR results). In addition, the peak at 2θ = 29.5° in the XRD pattern of hot-drawn samples corresponds to the 110 planes, with $d_{110} = 3.03\dot{A}$. The crystallographic distances calculated from the powder X-ray diffraction are shown in Table 2.5.

Orientation index, a relative measure of alignment of the crystalline phase: The 2D diffraction pattern of the as-electrospun and hot-drawn PAN samples (Figure 2.25 (a)-(c)) further verifies our assumption about the hexagonal packed arrangement of PAN chains. As shown in the 2D diffraction pattern of the 1x fibers (as-electrospun), the ho-

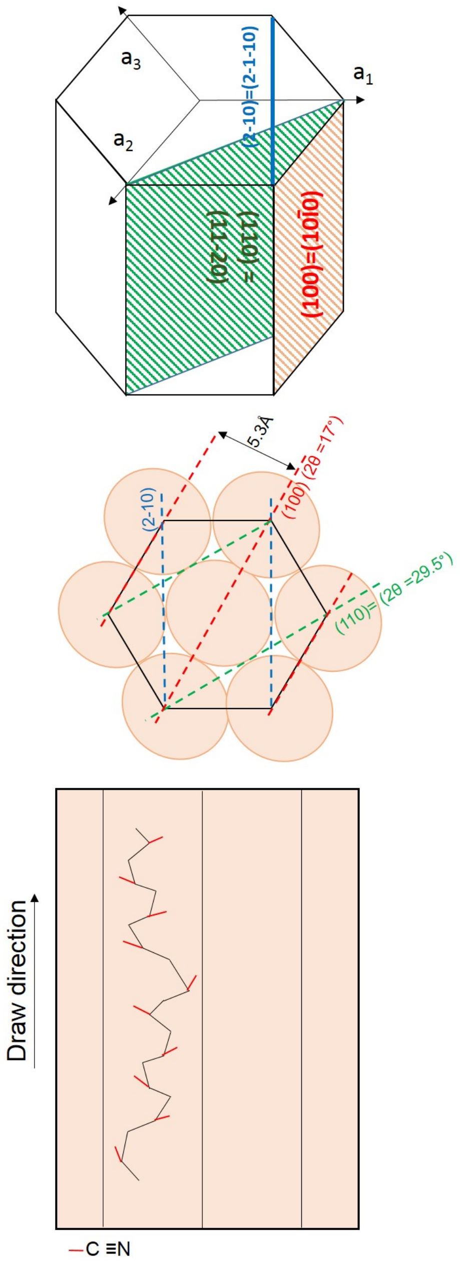

Figure 2.24: Hexagonal structure of PAN

mogeneous ring representing (100) plane at $d = 5.25\dot{A}$ denotes nearly no preferential arrangement of crystalline phase. In this case, there was no ring at $d = 3.03\dot{A}$. However, the pattern for the 2x and 4x fibers is symmetric with respect to the fiber axis (shown with a

Table 2.5: Calculation of interatomic spacing d using Bragg's law

Hot Draw Ratio = 1	Hot Draw Ratio = 2	Hot Draw Ratio = 4
	$\underline{2\theta = 17^\circ}$	
$d_{100} = \frac{0.154nm}{2sin\frac{16.84}{2}}$ $= \frac{0.154nm}{2\times0.146}$ $= 0.525nm$	$d_{100} = \frac{0.154nm}{2sin\frac{16.84}{2}}$ $= \frac{0.154nm}{2\times0.146}$ $= 0.525nm$	$d_{100} = \frac{0.154nm}{2sin\frac{16.94}{2}}$ $= \frac{0.154nm}{2\times0.147}$ $= 0.522nm$
	Hot Draw Ratio = 2	Hot Draw Ratio = 4
	$\underline{2\theta = 29.5^\circ}$	
	$d_{110} = \frac{0.154nm}{2sin\frac{29.5}{2}}$ $= \frac{0.154nm}{2\times0.2544}$ $= 0.303nm$	$d_{110} = \frac{0.154nm}{2sin\frac{29.5}{2}}$ $= \frac{0.154nm}{2\times0.254}$ $= 0.303nm$

black line). The maximum x-ray intensity appears on two arcs (rings): the inner and outer ring correspond to (100) and (110) planes, respectively. Since these peaks which correspond to spacing between "molecular rods" appear at nearly 90° angle with respect to the fiber axis, the rods should be parallel with the fiber axis, as expected from the hexagonal arrangement of PAN chains model proposed by [111].

The alignment of the crystalline domains was quantified for comparison purposes by defining an Orientation Index as:

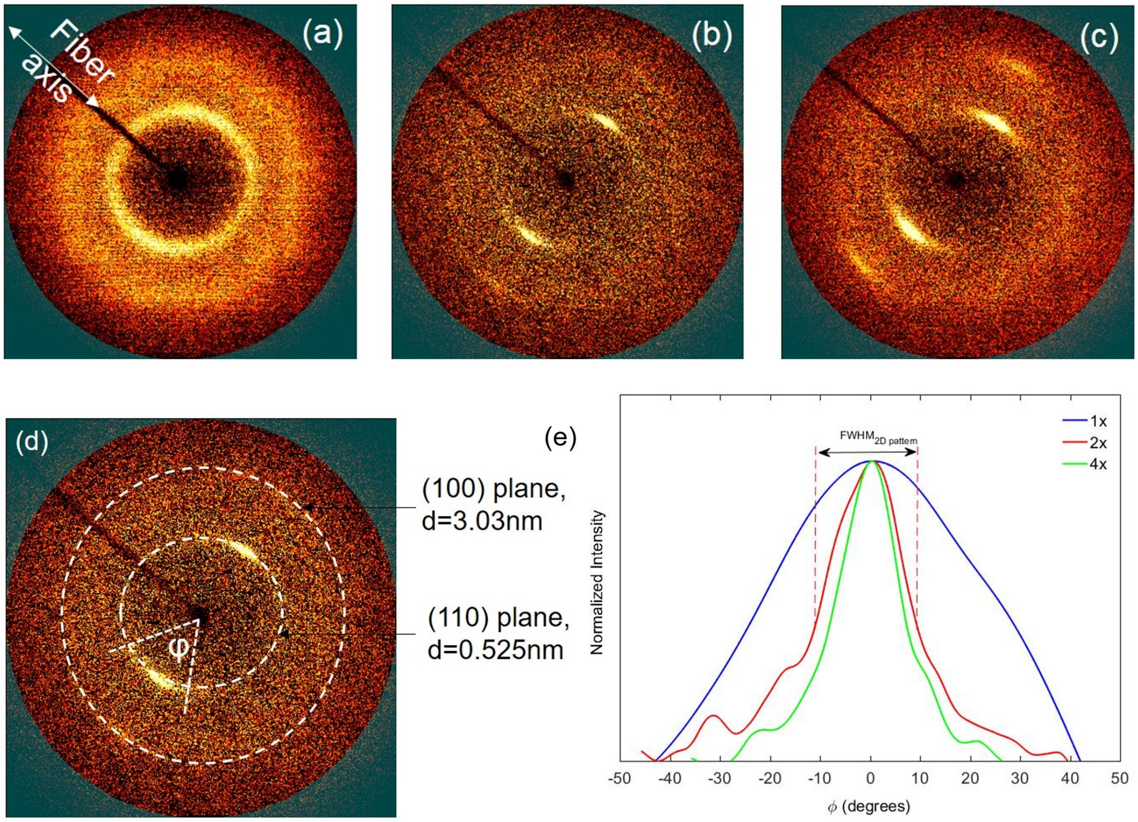

Figure 2.25: 2D Diffraction patterns for (a) 1x, (b) 2x, (c) 4x, (d-e): measurement method for FWHM calculation from diffraction patterns

$$Orientation\ Index = \frac{180 - FWHM_{2D\ pattern}}{180} \tag{2.5}$$

where $FWHM_{2D\ pattern}$ is the full width at half maximum of the X-ray intensity as a function of the azimuthal angle (ϕ as shown in Figure 2.25(d)) in the inner ring of the 2D XRD pattern (100). The variation of the XRD intensity as a function of for the three types of PAN nanofibers (as-electrospun, 2x and 4x) is shown in Figure 2.25(e).

Hot Draw Ratio	**Orientation Index**
1x	0.72
2x	0.88
4x	0.92

Table 2.6: Calculation of orientation index for crystalline phase

The orientation index is tabulated in Table 2.6. It is clear that the orientation of the crystallites has increased from the 1x fibers to the 2x fibers. Further hot-drawing the fibers to 4x, however, does not result in significant improvement in alignment. Orientation index of 1 signifies full alignment in the direction, of fiber axis. The crystallites in the fiber are significantly aligned at hot draw ratio of 2, leaving less room for further alignment of the already present chains.

Calculation of crystallite domain size: Crystallite size of the PAN (L_c) is calculated using the Scherrer equation Scherrer (Equation 2.6):

$$L_c = \frac{K\lambda_{XRD}}{(FWHM_{Powder}\ cos\theta)} \tag{2.6}$$

where K = shape factor, typically $\approx$ 0.94 for PAN, λ_{XRD} = X-ray wavelength = 0.154nm, θ = Bragg angle, in degrees, $FWHM_{Powder}$ = Full Width at Half Maximum of the X-ray diffraction pattern, in radians,

Substituting the value of FWHM obtained from the powder diffraction patterns seen in Figure 2.25 in the Scherrer equation (Equation 2.6), the crystallite size can be calculated. Figure 2.26 shows the normalized intensity for the powder diffraction curves at 17°. From this figure, the FWHM can be calculated. The calculated values of L_c are in Table 2.7. As expected, there are significant improvements in the size of the crystallites on initial hot drawing. Initial hot drawing upto 2x shows a 200% increase in the size of crystallite as compared to the as-spun (1x) case. Moreover, hot drawing from 2x to 4x leads to an additional 30% increase in the size of the crystallites.

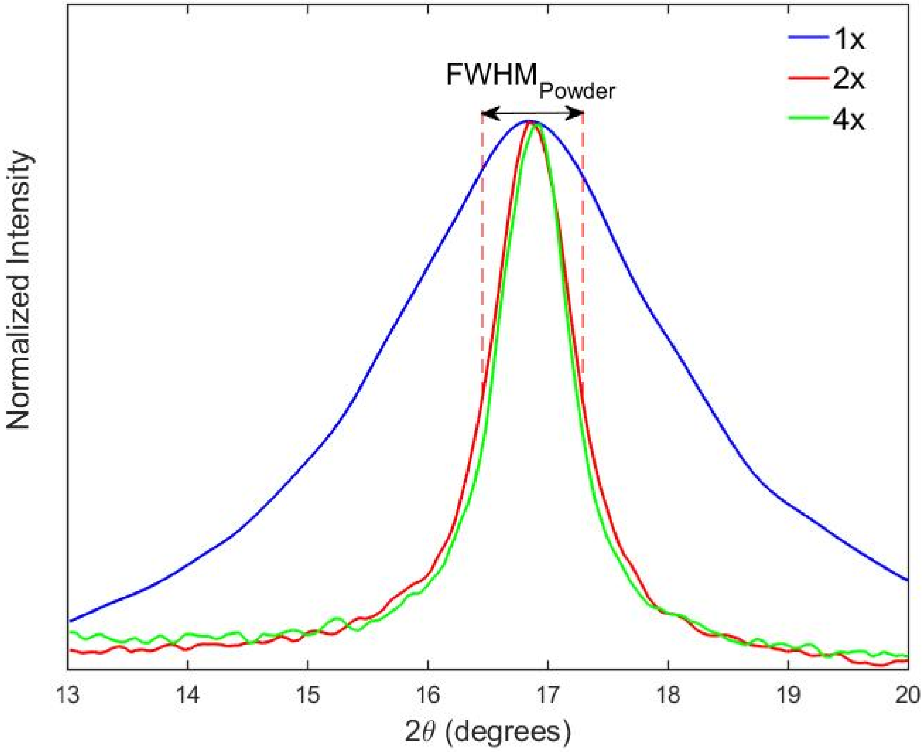

Figure 2.26: Normalized powder diffraction curves used to calculate FWHM

Hot Draw Ratio	L_c
1x	3.21
2x	9.62
4x	12.38

Table 2.7: Calculation of crystallite size L_c

2.2.3 Mechanical Characterization

The goal of hot drawing was to improve the chain alignment in PAN. A quantitative indication of chain alignment could be sought in mechanical properties of PAN as a function of hot drawing, specifically the strength and elastic modulus of the PAN nanofibers. To this end, the nanofiber ribbons were tested in tension using a GATAN microtest machine. Using a 20 N loadcell, nanofiber ribbons with linear density approximately 25 tex (1 tex=1 g/km) were tested. The nanofiber ribbons were mounted on a sample holder using adhesive applied at the portion of the grip. The sample holder was then transferred on to the testing stage and fixed in position using serrated grips.

A schematic of the sample holder is shown in Figure 2.27(a). The sample is mounted in the device shown in Figure 2.27(b), with a gage length ranging from 5 mm to 8 mm. As the nanofiber ribbon was relatively porous in regions between the fibers, true cross section of the nanofiber ribbon was measured indirectly as a function of the linear density of yarns to get accurate tensile properties. The true area (A_{true}) and linear density (λ) of the specimen is calculated as in Equation 2.7 and 2.2.3. The linear density was measured experimentally, and the true area was calculated accordingly.

$$A_{true}(m^2) = \frac{\lambda}{\rho}\frac{tex}{\frac{g}{cm^{-3}}}10^{-9} \tag{2.7}$$

$$\lambda(tex) = \frac{m_{ribbon}}{l_{ribbon}}\frac{g}{cm}10^{5}$$

$$\sigma = \frac{F}{A_{true}} \tag{2.8}$$

$$\epsilon = \frac{l}{l_0} \tag{2.9}$$

where A_{true} = true cross sectional area, λ = linear density, ρ = density of PAN = 1.3 g/cm^3, m_{ribbon} = mass of ribbon, l_{ribbon} = length of ribbon, 1 tex = 1 g/km, F = applied force, l = elongation of the ribbon, l_0 = gage length of the ribbon.

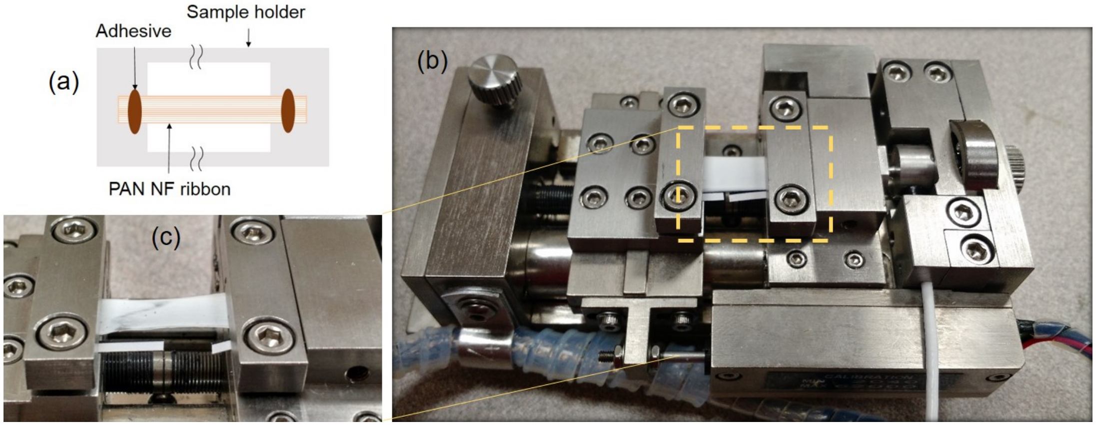

Figure 2.27: (a) Schematic of sample holder, (b) Gatan Microtester, (c) Tested PAN nanofiber specimen

The Gatan microstage movement was controlled using the software provided. One side (right grip side in Figure 2.27(b)) remained stationary while the other end moved, elongating the nanofiber by applying a strain rate $\dot{\epsilon}$ of 1mm/min. In all three cases, the failure occurred in the gage section of the fiber. The failed specimen of 1x is shown in Figure 2.27(c). Failure occurred in the ribbon in the gage section, as seen for the 1x case. An example of stress-strain plots of 1x, 2x and 4x hot drawn ribbons tested in tension, is presented in Figure 2.28. Stress and strain are calculated using Equation 2.8 and Equation 2.9 respectively. The 1x fiber demonstrated a ductile behavior, as is expected from predominantly amorphous polymers. The case of 1x fiber showed linear behavior upto 2.5%

strain. After this, the material yields while continues to elongate upto 20%. Hot-drawing to 2x and 4x results in a significant enhancement in modulus by 260% and 780%, which is likely due to the enhancement of alignment of chains achieved due to hot-drawing. In other words, the applied load on to the fiber will more effectively be transferred to the covalent bonds in the backbone of the chain when chains are more aligned with the fiber axis. Transition from ductile to brittle behavior also is observed in hot-drawn samples, with higher strength and lower strain to failure. The rather low ductility of the hot-drawn samples can be attributed to the formation of crystals which anchor the amorphous chains and lower their mobility. With an increase in alignment and growth of the crystalline domains, the strain to failure of the polymer is further reduced, and the sample fails catastrophically.

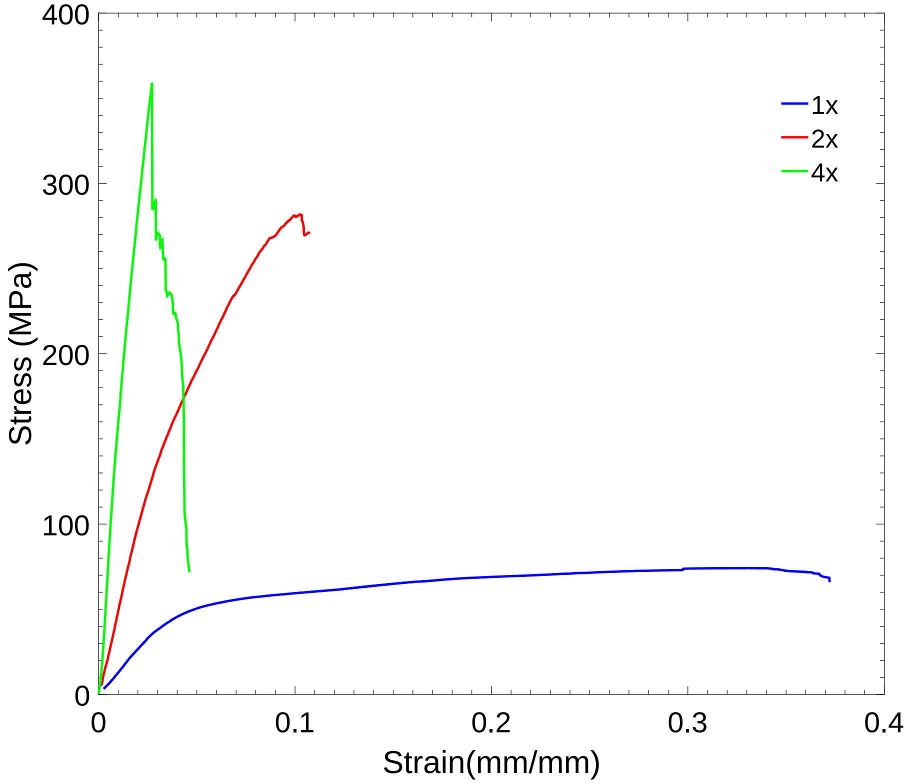

Figure 2.28: Tensile test of PAN nanofiber ribbons, hot drawn to 1x, 2x and 4x

Hot Draw Ratio	**Herman's Orientation Factor** f	**Strength (MPa)**	**Modulus (GPa)**
1x	0.22±0.06	75.4±2.1	1.5±0.3
2x	0.42±0.05	193.5±35.8	5.4±1.2
4x	0.55±0.05	391.4±9.8	13.2±6.3
% improvement of 2x w.r.t. 1x	91%	156%	260%
% improvement of 4x w.r.t. 1x	150%	420%	780%

Table 2.8: Summary of effect of hot drawing ratio on fiber properties

2.3 Conclusion

This chapter discussed fabrication of polyacrylonitrile nanofibers using the electrospinning technique with improvement of molecular orientation achievable during fabrication. Further enhancement in orientation was achieved using hot drawing of the as-electrospun nanofiber ribbons. Using spectroscopic characterization tools such as FTIR and XRD, the development of crystallites and their alignment have been quantified. Upto 150% improvements in the orientation of the molecular chains was observed. In addition the orientation index of crystalline phase increased to a value of 0.92, signifying almost complete alignment or the crystallites with the fiber axis. Approximately 300% increase in the size of the crystallites was observed using powder diffraction methods. Using this data obtained from non-destructive spectroscopic techniques, it was seen that improvement in properties started to plateau at hot drawing ratio of 4x. Thus, additional hot drawing beyond 4 times the original length of the nanofiber ribbon would not prove considerably beneficial in the process of aligning the molecular chains and improving the crystallinity of the nanofiber. Correlation between hot drawing, spectroscopic evaluations of alignment and the mechanical properties of the nanofiber ribbons were evaluated. Mechanical testing on as-spun and hot drawn nanofiber ribbons showed an improvement in strength and modulus of 420% and 780% respectively. In other words, the improvement in alignment of chains, increase of crystallite size and crystallinity due to hot drawing had a major impact on the tensile strength and modulus of the PAN nanofibers.

The next step in this research was to understand the impact of hot drawing of PAN nanofibers on their carbon counterparts. To achieve this, the PAN nanofiber ribbons were subjected to heat treatment processes of stabilization and carbonization to convert them to carbon nanofibers. Optimization of stabilization conditions, carbonization and spectroscopic methods of analyzing the effect of hot drawing will be studied in the next chapter, followed by mechanical testing of single carbon nanofibers in the subsequent chapter.

3. HEAT TREATMENT: CONVERSION OF POLYMER NANOFIBERS TO CARBON NANOFIBERS

3.1 Introduction

The conversion of PAN nanofibers to carbon nanofibers is known to take place through a series of chemical reactions led by a rise in temperature from 200°C to over 800°C. The thermal treatments on carbon nanofiber (CNF) precursor, namely thermal stabilization and carbonization, is often adopted from the carbon fiber (CF) industry which is used to produce microscale carbon fibers. However, the different processing steps utilized to fabricate microfiber and nanofiber precursors can result in distinctly different morphologies of precursors, thus, demanding modified thermal treatments to obtain the desired microstructure in CNFs.

In this chapter, we will first present a literature review on the formation of carbonized fibers and nanofibers as a function of the thermal treatment parameters. The literature presented here is mainly focused on CFs, but wherever the data exists in literature, we will also present a review of the literature on CNFs. Given the similarities in the precursor type (PAN) and thermal treatments to convert the precursor to carbon, the literature on carbon fibers has significantly guided us in pursuing our studies on CNFs. In the latter half of the chapter, we will present our experimental studies on the microstructure of carbon nanofibers as a function of the thermal treatment parameters. The focus will be on thermal stabilization conditions as a function of the molecular alignment in the precursor nanofibers, while the microstructure of the CNFs (after carbonization) will also be studied.

---

*Part of the data reported in this chapter has been reprinted with permission from “Carbonized Micro- and Nanostructures: Can Downsizing Really Help?” by Mohammad Naraghi and Sneha Chawla, 2014, Materials, 7, 3820-3833, Copyright [2014] by MDPI

The precursor nanofibers in our study are fabricated by electrospinning from a solution of PAN in dimethylformamide (DMF) followed by hot-drawing as discussed in the previous chapter. The molecular structure of precursors, thermally stabilized PAN and CNFs has been studied via a host of techniques including FTIR, XRD and TEM imaging.

3.2 Literature Review

Heat treatment of PAN precursor fiber to convert them into carbon is carried out at temperatures higher than 200°C. Liu et. al. [112] outlined three steps that are involved in conversion of PAN fibers into carbon fibers.

Oxidative stabilization: Heat treatment in air that forms cyclic structure of precursor fiber and prepares it for treatment at higher temperatures (200°C 400°C),

*Carbonization:*Heat treatment carried out in nitrogen or an inert atmosphere, forming turbostratic structure by removing the non-carbon atoms (800°C 2000°C),

*Graphitization:*High temperature treatment (HTT) in inert atmospheres subjecting the fiber to higher temperatures (2000°C 3000°C), thus improving the orientation of basal planes forming graphitic structure and imparting high stiffness to the fibers

The majority of chemical changes in the fiber occur when the fiber is heat treated between 200°C and 1500°C. At temperatures greater than 1500°C, minimal chemical changes are reported. However, enhancement in orientation, alignment and ordering of graphitic domains are observed at higher carbonization temperatures.

3.2.1 Chemical Changes in PAN Nanofibers during Stabilization

The first step in converting PAN nanofibers to CNFs is thermal stabilization. The stabilization, also referred to as oxidation, is carried out in air. The oxygen in air facilitates conversion of PAN leading to formation of a cyclic ladder-like structure as seen in Figure 3.1. Formation of the ladder structure is essential as it prevents fusion of molecular chains with each other during high temperature heat treatment (HTT).

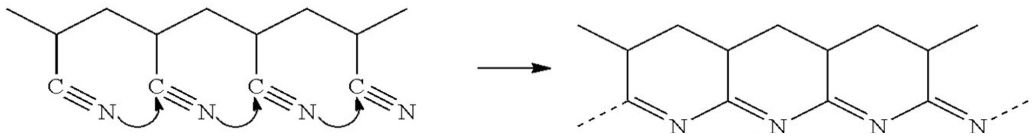

Figure 3.1: Proposed model of fully aromatic cyclized ring structure [21]

Stabilization of the fiber is an essential step to form mechanically strong carbon fibers. Stabilization is partly led by the diffusion of oxygen occurring from the outer skin of the fiber to the core. Insufficient diffusion of oxygen to the core can lead to incomplete stabilization of the fiber. A poorly stabilized core often leads to formation of highly defective and more randomly oriented turbostratic domains in the core. In extreme cases, upon carbonization of incompletely stabilized fibers, carbon fibers with hollow core have been observed [63, 113]. The presence of hollow core is likely an indication of the unstabilized core which got melted during carbonization and became conformal to the surrounding more stabilized PAN.

Proper stabilization conditions promote conversation of $C \equiv N$ groups to $C = N$, forming the ladder structure shown in Figure 3.1. FTIR studies can quantitatively determine the progress of stabilization of PAN fibers by evaluating the relative proportions of CH_2 and $C \equiv N$ groups in PAN which have converted to $C = N$ groups in stabilized PAN based on their peak intensities in the FTIR spectrum [39, 114]. The $C = N$ bonds act as initiators for subsequent chemical reactions at higher temperatures converting the PAN molecules to graphitized structure.

Most researchers have found temperatures between 200°C-300°C to be sufficient for stabilization of fibers, [39, 115, 116, 117, 118] while some researchers [45] claim that temperatures as high as 400°C are required to complete the stabilization process.

Thermal stabilization of PAN is highly exothermic, causing sudden generation of volatile species to leave the fibers. During this process and when high stabilization temperatures are employed, scission in the polymer chains may also occur [116]. Conversion of the nitrile groups into $C = N$ ladder structure suppresses the chain scission high temperature heat treatment. Stabilized PAN shows lower weight loss during carbonization, resulting in higher yield [119].

Very low stabilization temperatures inhibit complete stabilization, however, excessive stabilization temperatures can cause fusion of molecules and lead to thermal degradation. Optimization of stabilization conditions is thus essential to produce carbon fibers with good properties. Thermal stability of the stabilized PAN structure is attributed to cyclization of the nitrile groups forming a ladder structure. Extended amount of conjugation during the stabilization process, along with the oxygen incorporated in the polymer backbone, reduces the mobility of the molecules [32]. Due to formation of the ladder-like structure (Figure 3.1) and restricted mobility of the molecules, the stabilized PAN can be considered to be a thermoset in contrast to the thermoplastic PAN.

Chemical changes occurring in the fiber can be categorized into oxidation, cyclization, crosslinking, dehydrogenation, denitrogenation and aromatization [112, 120].

The proposed sequence of occurrence of these chemical reactions differ among researchers. Two different paths, seen in Figure 3.2 were suggested to form the cyclized structure. In the first proposed path, PAN molecules can undergo cyclization converting the nitrile groups into $C = N$ groups, followed by dehydrogenation giving rise to stabilized structure of PAN. The second path suggests the occurrence of dehydrogenation first causing elimination of the CH_2 bonds, followed by cyclization of chains forming a ladder structure of stabilized PAN [22]. Changes occurring in each of these stages is explained below:

Oxidation Reaction: Stabilization of PAN can be performed in air or an inert atmosphere. Stabilizing in air provides the advantage of a more evolved polymer backbone due to oxidation, providing better stability to the structure [121]. The proposed structure of PAN and

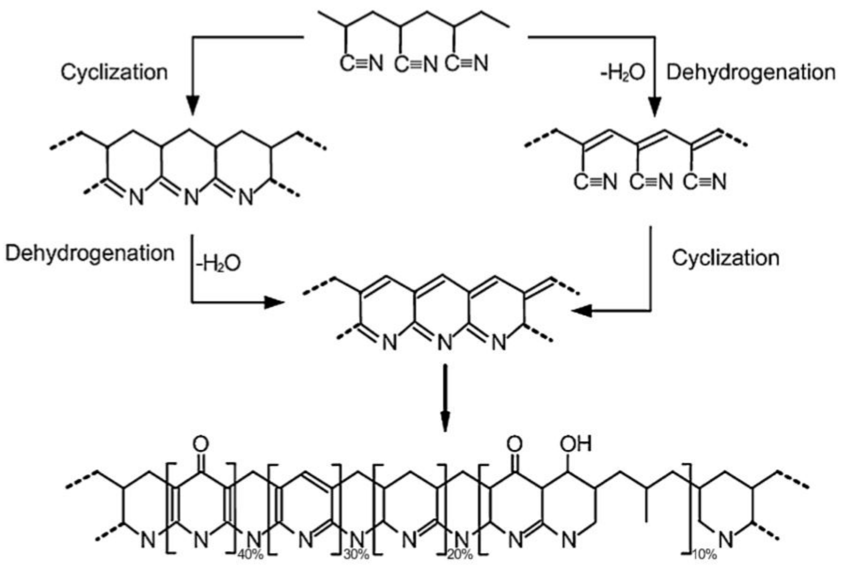

Figure 3.2: Proposed chemistry for conversion of PAN during pyrolysis [22]

thermally stabilized PAN in air is shown in Figure 3.3(a) [21]. It is to be noted that there is no consensus on the exact structure of stabilized PAN and slightly different structures of stabilized PAN have also been proposed [23] (Figure 3.3(b)).

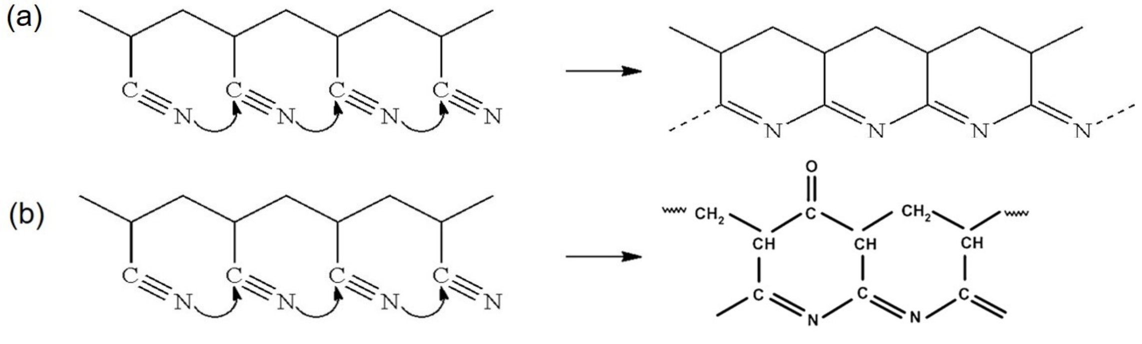

Figure 3.3: (a) Proposed model of fully aromatic cyclized ring structure [21], (b) proposed ladder structure [23]

Oxygen acts as an initiator to form activation sites for cyclization [122]. Structures containing ether links, hydroxyl groups, carbonyl groups and those in which nitrogen donates a lone pair of electron to oxygen have been proposed to serve as activation sites [123]. *Dehydrogenation Process:* In this process, PAN molecules lose hydrogen molecules by converting $C \equiv N$ to $C = N$ providing stability to the carbon chain. The dehydrogenation process consists of at least two steps. The first stage is oxidation, in which the oxygen molecule from the atmosphere creates an activation site as discussed above. The second stage is the elimination of hydrogen and oxygen in the form of water molecule. Different researchers propose the reactions in different sequences, with the original PAN molecule undergoing dehydrogenation followed by cyclization or cyclized PAN polymer undergoing dehydrogenation as seen in Figure 3.2. Dehydrogenation is not observed for stabilization in an inert atmosphere due to the lack of oxygen. However, bonds formed during dehydrogenation (in the presence of oxygen) are essential to provide thermal stability to the molecule and to reduce chain scission during high temperature treatment [123].
Cyclization Process: In this process polymer nitrile groups form bonds with adjacent chains to form a stable, ladder-like structure, similar to the one shown in Figure 3.2 [123]. The cyclization reaction is exothermic in nature and accompanied by evolution of gaseous products [124]. Cyclization can have many initiators: (a) impurities such as residual polymerization products, catalyst fragments [125], (b) chain end groups [126], (c) $C = N$ groups [127] (d) random initiation by hydrogen atom [125] (e) ketonitrile formation during hydrolysis [128].

3.2.2 Length Scale Dependence

In pure PAN, the cyclization and crosslinking mechanisms continue through radical or ionic reactions [23, 129], until inter- or intra molecular hydrogen transfer takes place [130]. On the basis of mathematical modeling, after stabilizing for one hour, the reacted oxygen content in the fiber plateaued beyond a radial position at 40% outward from the center of the fiber [131]. This indicates that if the fiber diameter was 60% of its original diameter, after one hour, the reacted oxygen content would be constant through the fiber cross section, thus, stabilizing it completely.

Radial inhomogeneities in the form of skin-core structures in carbon fibers have been known to arise from stabilization process [9, 12, 60, 61], as discussed in details in Chapter 1. Thus, as hypothesized in Chapter 1, if the fiber diameter is reduced to the diameter of the skin in microfibers or less, fibers with lower radial inhomogeneities will be formed [12]. This hypothesis has led to the idea of the formation of nanofibers, with more uniform structure and higher strength, which is the basis of the current study.

3.2.3 Fiber Shrinkage during Stabilization

During stabilization, shrinkage in length of the fiber has been observed. Shrinkage between 13%-33% during stabilization has been reported by researchers [24, 27, 122, 132]. The shrinkage is partly due to entropic forces developed in PAN at elevated temperatures which tend to coil the chains. Amount of shrinkage can be controlled by applying tensile loads on the fibers during stabilization. Sufficiently high loads can overcome entropic forces and prevent this mode of fiber shrinkage. On application of higher loads, initial elongation is observed in the fiber followed by shrinkage [50]. Chemical changes occurring in the fiber upon tensing, lead to plastic flow. Following this plastic flow, the nitrile groups in the fiber rotate with respect to each other, forming $C = N$ groups at an angle of 120°, leading to macroscopic shrinkage in the fiber [122, 133].

Shrinkage in the fiber can be divided into primary and secondary shrinkage [28], with primary shrinkage about 10% for homopolymer fibers. The primary shrinkage is considered to be physical relaxation of the chains and is not influenced by external conditions of stabilization time, temperature and environment, while secondary shrinkage is due to chemical reactions and is influenced by external conditions [27, 122, 123]. Amount of tension applied on the fiber is very important to obtain mechanically strong fibers [134]. The amount of required tension varies according to type of polymer, co-monomer content, heating temperature, method of applying tension, time and temperature of stabilization. Layden [132] reported that tension was generated in the fiber when heated at 250°C. However, when using multi stage heating, he found that upto a temperature of 150°C, tension was generated in the fiber, which fell rapidly at higher temperatures from 150°C to 250°C and again increased and plateaued at 270°C. This could be attributed to temperature dependent relaxation mechanisms in the fiber at different temperatures. Tension applied on the fibers during stabilization caused links to form between adjacent chains due to the C = O bonds, thus restricting the motion of the chains [60].

Fibers that are stretched more or less than their optimum amounts during stabilization are seen to have pores when carbonized. According to Bahl [28], optimally stretched fibers possess no surface holes after carbonization and have high tensile strength as compared to fibers that have been stretched above or below this optimum amount. Over-stretching of the fibers causes the chains to be straight, however, the high tension causes bond rupture and surface holes. On the other hand, under-stretching of the fiber during stabilization allows for chain relaxation and loss of chain alignment during stabilization.

3.2.4 Effect of Stabilization Temperature and Duration on Morphology of CNFs

Carbon nanofibers fabricated from PAN nanofibers stabilized at 280°C for 2 hours with a load applied during stabilization did not show the skin core inhomogeneity that was observed in carbon fibers. Turbostratic domains in the fibers were observed throughout the cross section of these fibers [38]. On the other hand, nanofibers with 400nm diameter have been found to be insufficiently stabilized at temperatures below 280°C for 2 hours [38]. On stabilization at 250°C for 30 mins, Zussman et.al [135], observed skin-core structure in carbon nanofibers of diameter 220nm, possibly due to the low heat treatment temperatures used in the study which did not permit cyclization of the core. Contrary to this, a study on carbon nanofibers of 300nm diameter that had been stabilized at 280°C for 3 hours saw a homogeneous distribution of turbostratic domains through the fiber diameter [136]. In another study, skin-core structure was not observed in nanofibers of 500nm diameter that were stabilized at 300°C for two hours and carbonized at 1700°C [30]. In this case, the turbostratic domains were dispersed throughout the cross section of the nanofiber and were randomly oriented throughout the fiber with little or no preferential orientation in the fiber direction. These results further establish the hypothesis of disappearance of the skin-core structure as the diameter of carbon fibers is reduced from the microscale to the nanoscale.

3.2.5 Chemical Reactions during Carbonization

In their patent, Saito and Ogawa [137] recommended stabilizing the fibers in an oxidizing atmosphere under a load such that the fibers are allowed to shrink 40% -70% of the free shrinkage in the fiber. Free shrinkage is the amount of shrinkage that would have occurred if the fibers were oxidized without any applied load. According to their study, shrinkage of less than 40% of the free shrinkage can adversely affect strength and modulus (possibly due to excessively high internal stresses developed during processing), while shrinkage greater than 70% of the free shrinkage yielded poor quality fibers with fuzzing likely due to entropic forces generated in the polymer during carbonization and consequent partial loss of graphitic alignment. The authors also recommended carbonizing the fibers upto 1000°C under tension, and further heat treatment without load. Bahl [134] suggested that carboxyl and carbonyl bonds formed during stabilization prevent chain cleavage during carbonization of PAN fibers.

At temperatures just above stabilization temperature, from 300°C to 500°C, oxygen escapes as water vapor, reducing the quantity of oxygen in the fiber [138]. Water vapor

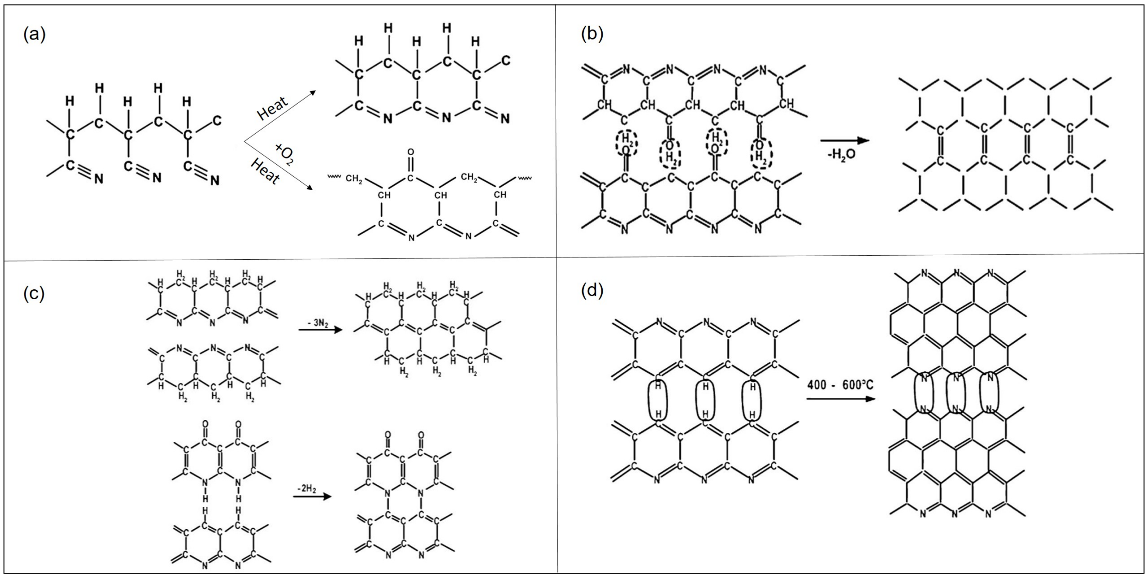

Figure 3.4: Proposed chemistries for conversion of PAN to CNF (a) during stabilization [21], (b) release of H_2O [24], (c) release of N_2 and H_2 [25], (d) formation of turbostratic layers

is formed due to crosslinking condensation reactions between adjacent chains as seen in Figure 3.4(b) [24]. At 600°C to 700°C, the oxygen that has entered the fiber during the stabilization stage, is released as carbon monoxide. However, graphite-like crystallites have already started to form, creating a fairly rigid backbone [60]. At temperatures upto 800°C, hydrogen cyanide and ammonia are released [139]. According to Watt [25], the ammonia is formed due to the chain termination reaction that takes place. The evolution of N_2 is first observed around 720°C. More nitrogen is released from the bulk than surface of the fiber [140]. The mechanism for evolution of N_2 and H_2 proposed by Watt, is seen in Figure 3.4(c). At higher temperatures upto 2000°C, C - C bonds form in aligned chains and create turbostratic layers (Figure 3.4(d)).

At higher temperatures, the misalignment between turbostratic layers is reduced, the impurities present between layers are removed, reducing the distance between layers to that of graphite (0.335nm). The structure of turbostratic and graphitic carbon is seen in

Figure 3.5.

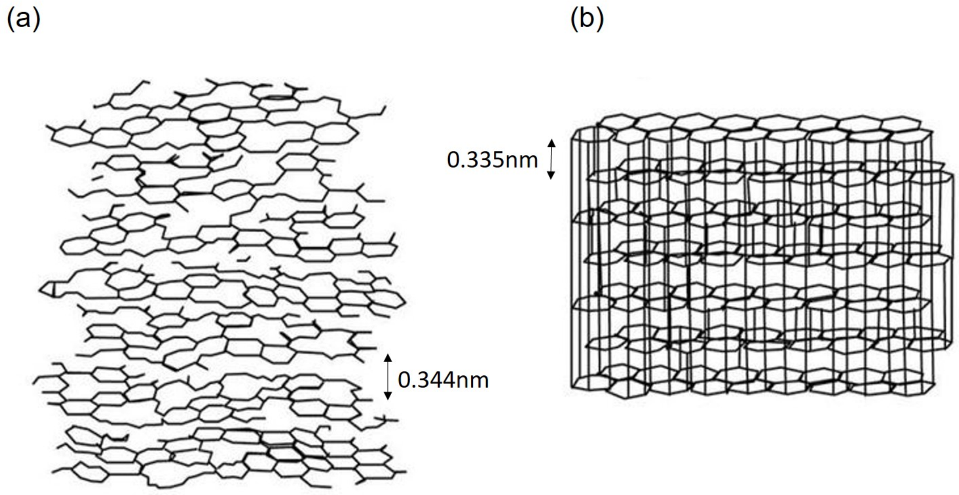

Figure 3.5: Structure of (a) turbostratic carbon, (b) graphitic carbon [26]

3.2.6 Effect of Heat Treatment Parameters on Microstructure and Mechanical Properties of Carbon Fibers Prepared from PAN Precursors

A systematic study carried out by Fitzer [27] et. al, evaluated mechanical strength of carbon fibers formed by stabilizing precursor fibers at varying temperatures and heating rates. Copolymer PAN precursor fibers containing 6wt% methylacrylate (MA) and 1wt% itaconic acid (IA) were used in the study of mechanical tests were performed on fibers carbonized at 1350°C. A clear indication of the effect of stabilization can be seen in Figure 3.6. According to this study, stabilization temperature of 270°C at 1°C/min was the optimum stabilization parameters to maximize the strength of carbon fibers.

Studies done by Bahl [28] and Watt [141] showed that the oxidation process is intramolecular instead of intermolecular leading crosslinking between chains (Figure 3.7). Bahl carried out experiments on stabilized fibers that were oxidized for times ranging

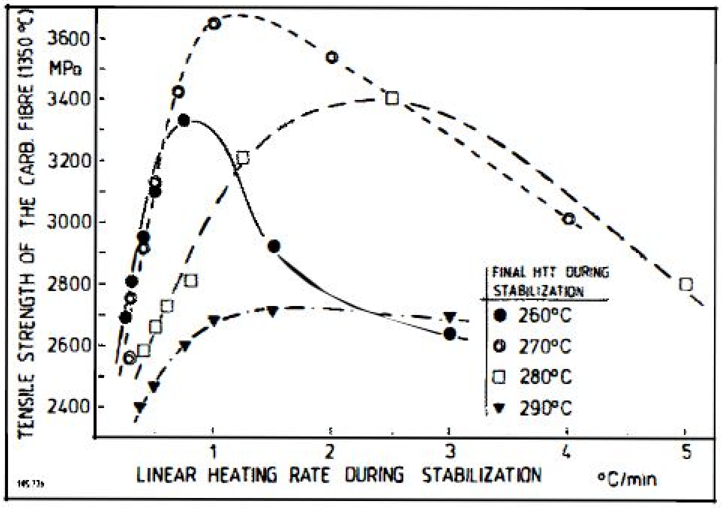

Figure 3.6: Mechanical Strength of C-fibers formed by different stabilization temperatures and time [27]

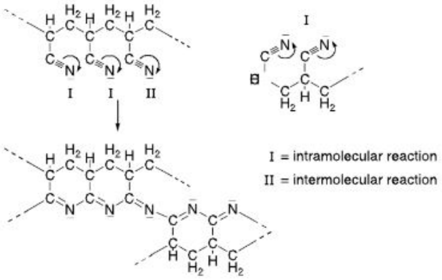

Figure 3.7: Inter-molecular and intra-molecular reactions during stabilization of PAN [28]

from 2 hours to 40 hours. He found that for fibers stabilized upto 8 hours at 205°C, the strength of the oxidized fiber reduced dramatically with oxidation time, however, at higher oxidation times, the decrease in strength is more gradual. By observing the decrease in fiber strength Bahl concluded that if the oxidation process is intermolecular, more strength would be required to overcome the force between the chains. Since the force required in this case was reduced on oxidation, he concluded that the cohesive energy between the relative chains was reduced, and hence the reaction is intramolecular. He suggested that there exists an optimum time for oxidation, at which the mechanical strength of the carbon fibers is maximized [134].

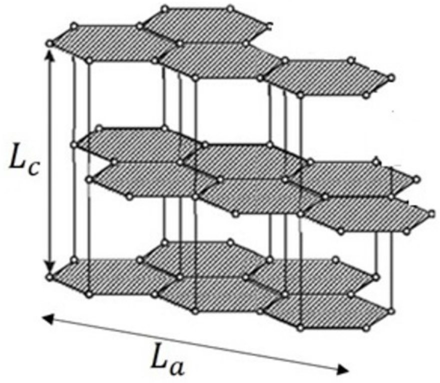

Figure 3.8: Schematic of turbostratic domain showing L_a and L_c [29]

Many researchers have studied the effect of the carbonization temperature (often above 800°C) on the microstructure and properties of subsequent carbon fibers. Kim et. al. Kim, used XRD for characterization of carbon fibers, and calculated the crystallite size, L_c (as seen in the schematic in Figure 3.8) and the crystallographic distance associated with each peak, d_{hkl}, by using the Scherrer equation (Equation 2.6) and Bragg's law (Equation 2.4).

An increase in carbonizing temperature from 700°C to 1000°C resulted in an increase of 86% in L_c. Similar work, at higher temperatures, was carried out by Ko et. al [142], who showed an increase in the size of L_c from 2nm to approx. 7.5nm with an increase in carbonization temperature from 1400°C to 2800°C. Preferred orientation of the crystallites (Equation 2.5), increased from 94% to 97%.

Modulus of the carbon fibers was enhanced by increasing the carbonization temperature from 1400°C to 2800°C, with slower rate on increase in the 1600°C to 2400°C range. In contrast, the tensile strength of the fibers was at its maximum at 1600°C, then reduced and remained fairly constant at temperatures above 2100°C. Rafique et. al. [143] studied fabrication of ultra-thin PAN nanofibers and their conversion to carbon nanofibers. In his work, stabilization temperature of 300°C was used. Lower temperature of 200°C, led to incomplete stabilization of the fiber, causing them to melt and fuse with each other during carbonization. Heating rates of 1°C/min were used for carbonization, as higher rates caused fiber breakage during the process. CNFs that were carbonized on substrates which did not allow for shrinkage were straighter and thinner compared to fibers carbonized without any constraints.

Arshad et. al [30] carbonized nanofibers at temperatures between 800°C to 1700°C. In this study it was found that maximum strength in the nanofibers was achieved at carbonization temperature of 1400°C, while the modulus of the nanofibers continue to increase with increase in temperature to its maximum value at 1700°C (Figure 3.9). The increase in mechanical strength of the nanofibers is due to the crystalline structure of the nanofibers, which continues to evolve with temperature. Randomly oriented crystallites were formed at higher carbonization temperatures, which caused early rupture due to the stress mismatch at the interface of the turbostratic domains embedded in amorphous matrix. Initial increase in strength was attributed to an increase in carbon content of the fiber and densification. However, as the crystallite size continues to increase with temperature, the neighboring crystals will interact with each other and compete for the atoms of amorphous carbon in between them, leading to residual stresses and a noticeable drop in strength.

As seen from the discussions above, numerous works have been performed on improving the properties of carbon fibers and carbon nanofibers via heat treatment conditions. However, there is little literature on the effect of alignment and crystallinity on stabilization of nanofibers and the effect of molecular alignment on the cyclization reactions. Also, there is no literature published to date on the effect of improvement in molecular alignment on the mechanical properties of single carbon nanofibers.

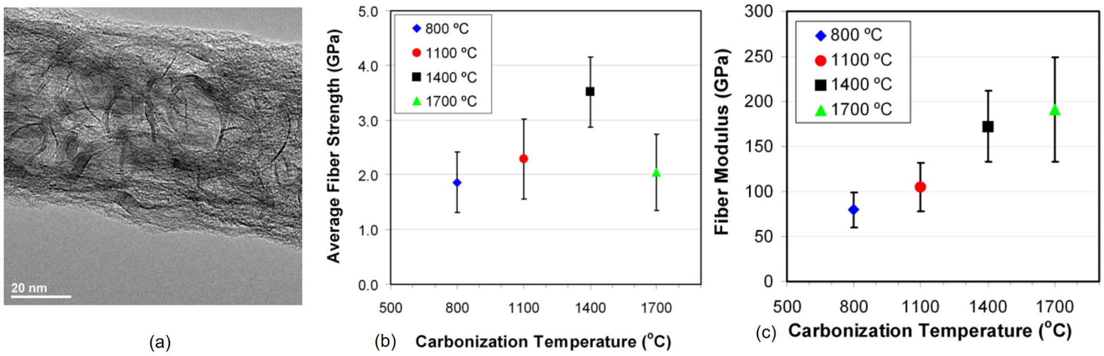

Figure 3.9: (a) TEM image showing crystallites of turbostratic carbon in nanofibers carbonized at 1400°C, (b) average fiber strength vs carbonization temperature, (c) fiber modulus vs carbonization temperature [30]

The following sections present a detailed description of the effect of alignment on the stabilization parameters required to form high quality carbon nanofibers. The procedure used for carbonization of the nanofibers is also discussed.

3.3 Experimental Work

3.3.1 Effect of Stabilization Temperature on Cyclization of PAN

In order to convert electrospun PAN nanofibers into carbon nanofibers, the first step is to thermally stabilize the fibers. The as-spun nanofibers were stabilized in air in a conventional oven at temperatures of 250°C - 300°C. Thermocouples were placed close to the sample to properly monitor and adjust the temperatures of the stabilization environment. As discussed in Section 3.2.3, free shrinkage is observed in nanofibers that have been stabilized without applied load, due to the thermally enhanced entropy of the chains and relaxation in the molecules. Prior to beginning the stabilization process, the fibers were gripped at the ends with approximately 20% slack in a ceramic crucible. As stabilization progressed, the nanofibers were allowed to shrink, however, at the end of stabilization, the fibers were in tension due to the gripped ends. Reducing the initial slack to less than

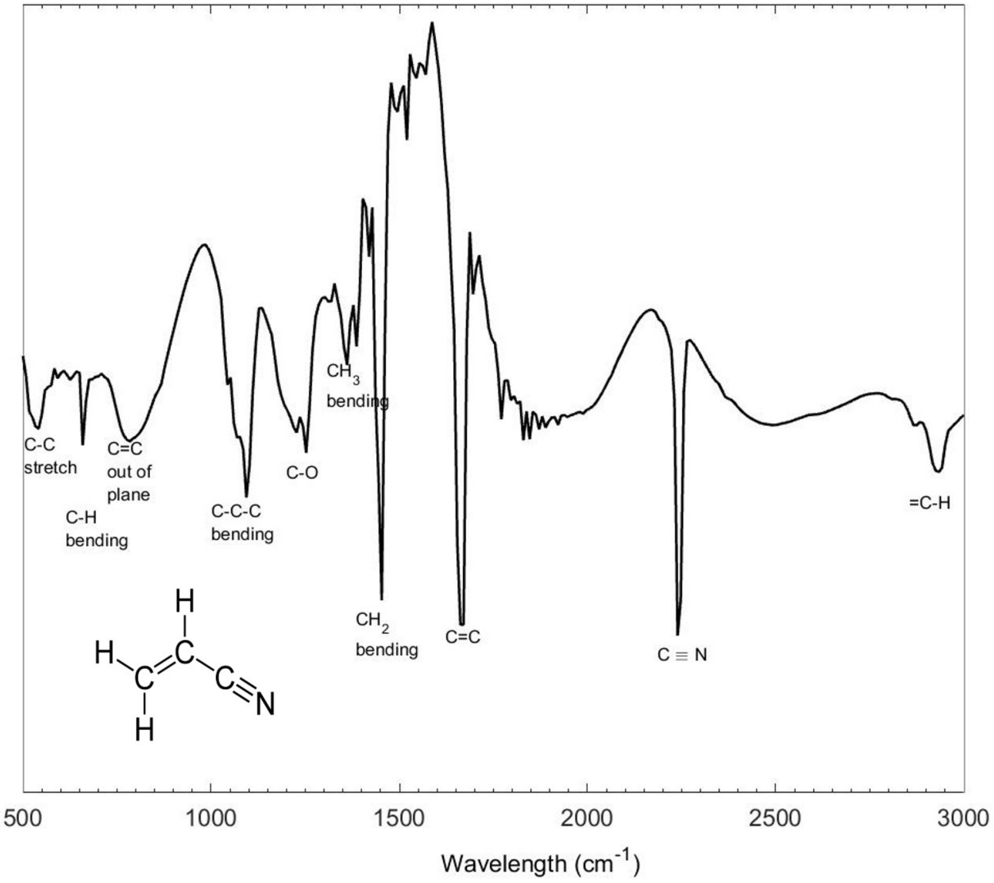

Figure 3.10: FTIR spectra of as-spun PAN nanofiber ribbon before stabilization

20% led to fiber breakage during stabilization due to internal stresses developed in the nanofibers. Additional slack however could be accommodated due to more than 20% thermal shrinkage of the fiber.

As described in previous sections, the formation of ladder structure of PAN (Figure 3.2) plays a vital role in the formation of high quality carbon nanofibers. To study the evolution of the ladder structure and ensure completion of the stabilization process, PAN nanofibers were heat treated to various temperatures viz, 100°C, 180°C, 220°C, 245°C, 265°C, 280°C, 295°C. In all cases the oven was heated from room temperature (RT) upto the desired temperature at a rate of 2°C/min and held at constant temperature for 2 hours.

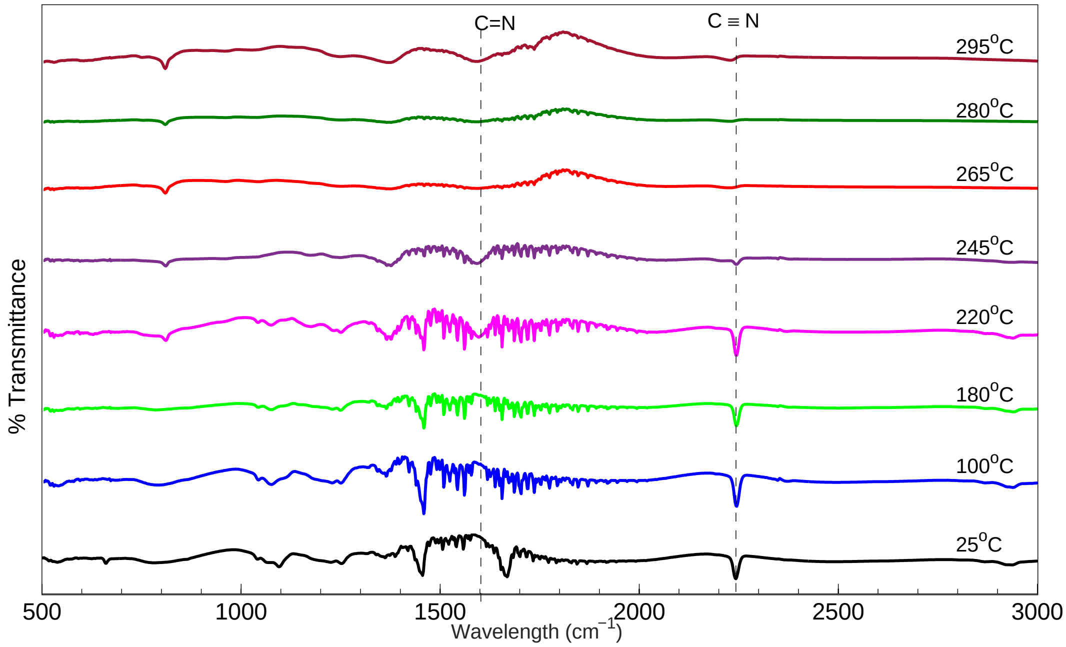

Figure 3.11: FTIR spectra for as-spun 1x PAN nanofibers stabilized at various temperatures

Once the fibers were stabilized, they were air cooled in the oven. The stabilized nanofiber ribbons were mounted on a specimen holder and prepared for testing using Fourier Transfer Infrared Spectroscope (FTIR). The FTIR spectrum of the samples were collected via Thermo Nicolet IR spectrometer at room temperature. Transmittance FTIR spectra for as-spun PAN nanofiber ribbon is shown in Figure 3.10 and for PAN nanofiber stabilized at 295°C is shown in Figure 3.13 The FTIR spectrum of PAN nanofibers before stabilization has peaks relating to C−C, C−H, CH_2, CH_3, C−C−C, C−O, C ≡ N, =CH bonds. The peak observed at 2243cm^{-1} relates to the nitrile groups (C ≡ N) present in the molecular chain of PAN. The peaks at lower frequencies (500cm^{-1} to 1400cm^{-1}) relate to bending frequencies in the molecule. The FTIR spectra for stabilization temperatures of 100°C, 180°C, 220°C, 245°C, 265°C, 280°C and 295°C were baseline corrected and plotted in Figure 3.11. They were compared to the reference sample, PAN at 25°C (i.e. as-spun, un-

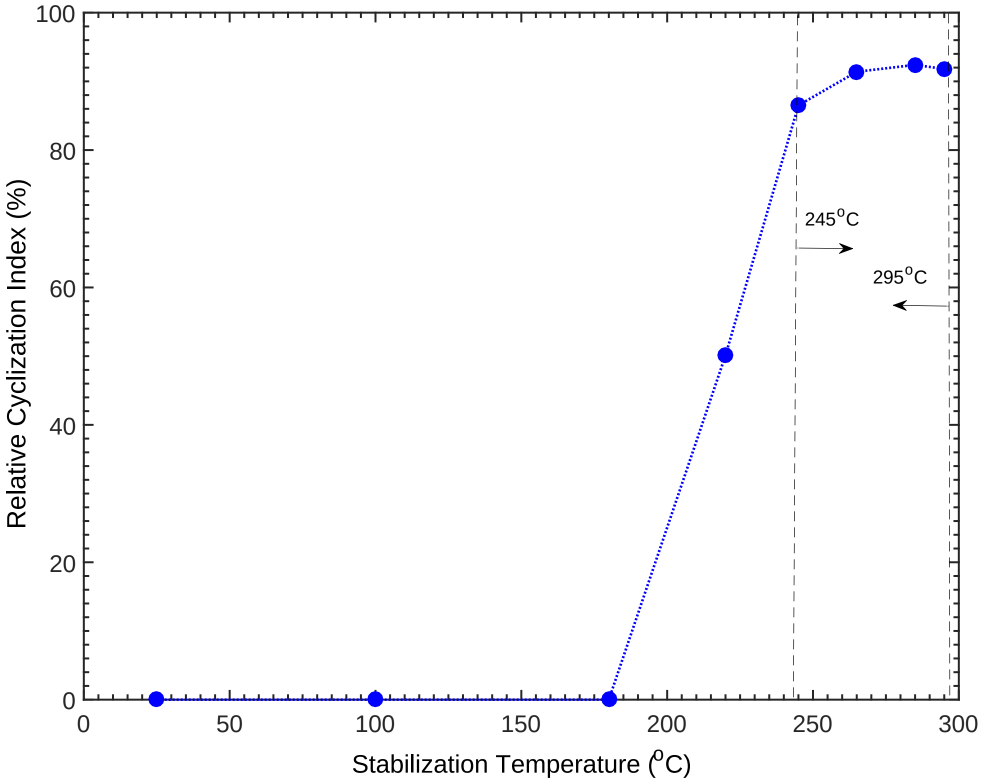

Figure 3.12: Relative cyclization index calculated for 'as-spun' (1x) PAN fibers stabilized at different temperatures

stabilized PAN nanofiber ribbon) to understand the evolution and removal of key elements and chemical bonds developed in the process of stabilization. The primary change was observed in the reduction of the peak at 2243cm^{-1} (representing $C \equiv N$) and the evolution of the peak at 1600cm^{-1} (representing $C = N$). This change was observed to begin at 220°C and continued upto 295°C. This change in FTIR spectra is indicative of the formation of ladder structure that has been discussed previously in Section 3.2.1. The degree of thermal stabilization can be estimated by monitoring the intensity of peak for the ring structure, i.e. $C = N$ group, seen at 1600 cm^{-1} relative to the prominent peak of $C \equiv N$ in PAN before stabilization at 2243 cm^{-1}. As the temperature was increased, the intensity of the

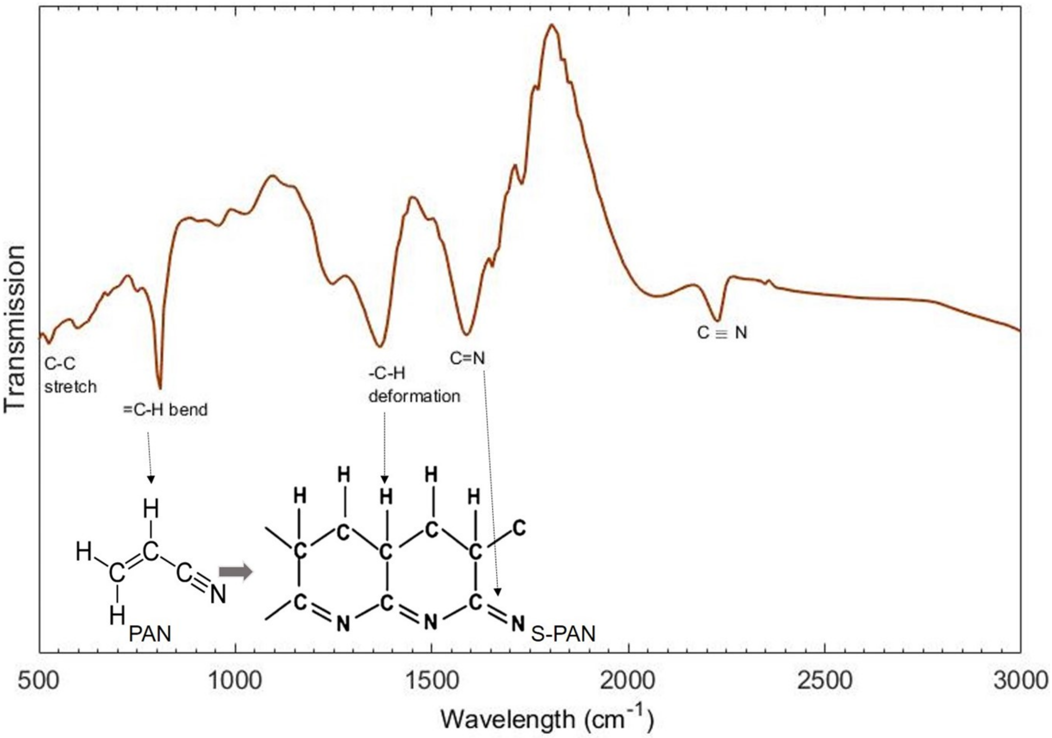

Figure 3.13: FTIR spectrum of PAN fibers stabilized at 295°C, showing the bonds present in the fiber

C = N peak increases and the C ≡ N peak reduces. Also, a peak at 800 cm^{-1} was seen above 220°C, corresponding to C-H out-of-plane bending of the molecules. The amount of cyclization (stabilization) in the nanofibers was calculated using the Relative Cyclization Index (RCI), given in Equation 3.1 as the ratio of the intensity of peaks of the C = N bonds and the nitrile group.

$$RCI = \frac{I_{C=N}}{I_{C=N} + I_{C\equiv N}} \tag{3.1}$$

The RCI for various temperatures is plotted in Figure 3.12. The emergence of the C = N peak at 220°C is clearly reflected in the calculated RCI of stabilized nanofibers. As the C ≡ N in the PAN backbone continue to form cyclic structures and convert to C =

N (Figure 3.11 and Figure 3.12), the RCI value continued to increase rather rapidly until about 265°C, where it began to plateau.

According to this analysis, a minimum temperature of 245°C was required for the nanofibers to achieve a degree of cyclization of 85%. Using RCI as the only criteria, the range of stabilization temperature could have been chosen to be anywhere in the range of 245°C to 295°C satisfying a minimum of 85% cyclized structure. However, other factors for selecting the optimum stabilization conditions will be discussed in the following sections.

Color change in stabilized PAN fibers: In addition to using FTIR, change in color of the nanofibers has been used as a visual indicator to estimate the amount of cyclization that had occurred in the nanofibers.

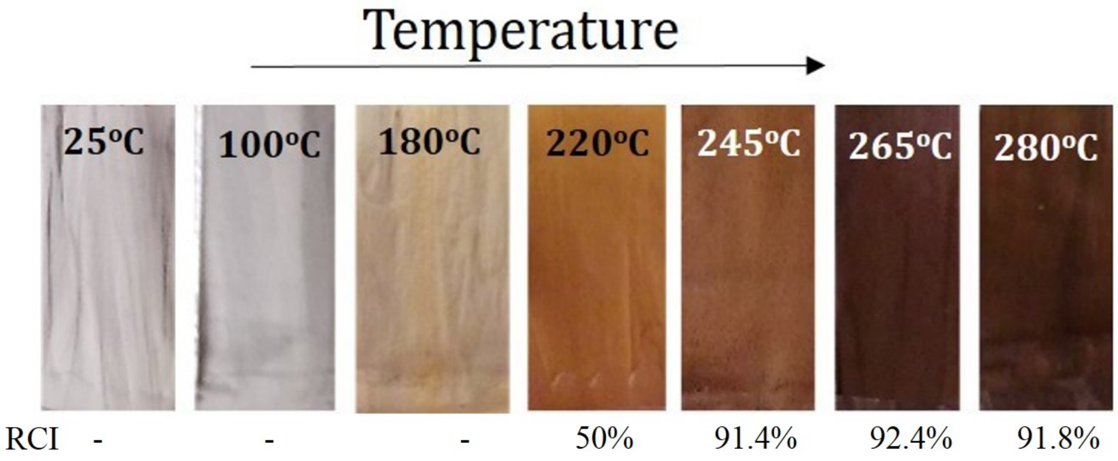

Figure 3.14: Color change in heat treated of PAN nanofiber ribbon. The associated ring cyclization index (RCI) is shown underneath each figure. The ring cyclization below ≈200°C is insignificant.

A clear change in color from white to yellow to light brown to dark brown was visible with increasing temperature. This change in color was attributed to the ladder structure formed in the stabilized PAN nanofiber [144].

A visible change in the color began at 180°C where the fibers started to have a yellowish appearance. At 220°C, a significant color change was observed, turning the ribbon to a yellow-brown color. With further increase in stabilization temperatures, the color changed to dark brown (Figure 3.14). As exothermic heat of stabilization was released, the intensity of change in color of the nanofibers started to reduce and complete stabilization was assumed once the fibers reached a dark brown color seen at high temperature in Figure 3.14.

Radial inhomogeneity resulting from stabilization conditions: From the data presented to this point, any heat treatment temperature above 245°C was sufficient to stabilize the fibers upto 85% RCI. The next step in this study was to analyze the temperature effect on the formation of the skin core structure during stabilization, a phenomena clearly seen in micro scale fibers, as discussed in Section 1.2. A distinct appearance of this inhomogeneity has been observed in fibers with large diameters when hollow fibers were formed upon carbonization of poorly stabilized fibers. It is essential to understand if this effect will be reduced or even eliminated by scaling down the fibers. According to the discussion in Section 3.2.1, since stabilization is controlled by the diffusion of oxygen to the fiber core, reducing the fiber diameter should facilitate the diffusion of oxygen to the core, thus stabilizing the fiber homogeneously through the thickness. In the past, researchers have estimated the critical thickness of the fiber to be 1-2μm in order to achieve through thickness stabilization yielding a high degree of graphitic alignment [4, 57].

Since it is driven by the diffusion of oxygen and heat, the thermal stabilization of CNFs is not only controlled by the penetration depth of oxygen, but also by the rate of the stabilization of the core. Hence, under accelerated stabilization conditions, e.g., relatively high stabilization temperatures, CNFs with radial inhomogeneity may also form.

In other words, rapid stabilization in the skin even in submicron fibers may suppress the oxygen diffusion rate to the core, leading to poorly stabilized core. To further study and demonstrate this effect, we carbonized PAN fibers that were stabilized at two temperatures: 265°C and 295°C. The stabilized nanofibers were then carbonized at 1100°C in nitrogen atmosphere and observed under SEM and Transmission Electron Microscope (TEM). The details of the carbonization procedure are described in Section 3.3.2 CNFs from various locations of the ribbon were mounted on a SEM holder. Using the sputter coater, the fibers were sputter coated with Pt of thickness 4nm to reduce charging effects in the SEM. The sputter coated CNF specimens were observed in the SEM (FEI Quanta 600FE). SEM images revealed that the diameter of the CNFs were mostly in the range of 200nm - 800nm. The CNFs were then mixed with ethanol and sonicated for 20 minutes after which, using a dropper, they were mounted on Cu TEM grid for observation in TEM. The TEM used for this purpose was the G2 F20 FE. The samples were then observed in TEM. The CNF's stabilized at 265°C showed fairly homogenous cross-section and did not show any sign of radial inhomogeneity. However, TEM images of CNFs achieved from stabilization at 290°C showed hollow cross-sections or core sections with lower density of carbon. There seemed to be a critical diameter of $\approx$500nm above which nanofibers with a hollow core formed, as shown in Figure 3.15. The formation of the hollow cores in CNFs could be attributed to the poorly stabilized/unstabilized PAN core, which melts during carbonization and conforms to the surrounding PAN, a mechanism proposed by Liu et al. [112]. The poor stabilization of the core, as pointed out before, was a result of the low rate of oxygen and stabilization by-products being diffused through the skin. In addition, the formation of hollow cores in 295°C stabilized fibers, in contrast to solid (filled) CNFs of 265°C stabilized fibers, suggests that the thermal stabilization of the PAN at 295°C suppresses oxygen diffusivity. In other words, the higher temperature of 295°C could have led to accelerated thermal stabilization of PAN skin, preventing or suppressing further diffusion of oxygen to the core. This is in contrast to lower stabilization temperatures of 265°C, in which slow thermal stabilization of the skin could only marginally affect the diffusion of oxygen to the core. Using TEM images of 295°C, the maximum penetration depth of oxygen from the surface of PAN can be approximated to be equal to the thickness of the solid skin of CNFs, as presented in Figure 3.15 and Table 3.1, which is $\approx$250nm - 400nm.

Therefore, there seem to be two parameters controlling the formation of radial inhomo-

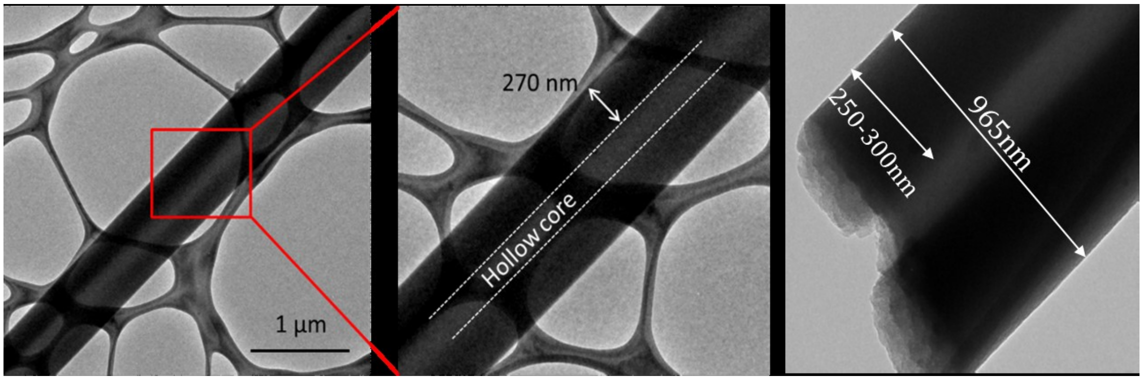

Figure 3.15: Carbon fiber obtained from PAN precursor stabilized at 295°C showing evidence of skin core structure

Sample No.	Diameter of CNF (nm)	Hollow / Filled	Skin thickness (nm)
1	133	Filled	-
2	209	Filled	-
3	375	Filled	-
4	428	Filled	-
5	584	Hollow	250
6	747	Hollow	308
7	829	Hollow	344
8	965	Hollow	369

Table 3.1: Diameter of CNF with corresponding fiber structure

geneity in carbonized structures: thickness of the sample and rate of thermal stabilization. While generally samples with thicknesses comparable to or less than the penetration depth of oxygen diffusion tend to be uniform, rapid stabilization of the skin may suppress the skin's oxygen diffusivity, lowering the oxygen content reaching the core. Depending on the temperature of the stabilization, oxygen penetration depth may vary from $\approx 0.5\mu$m to 2μm, with lower stabilization temperatures favoring the upper bound.

The study presented above which relates the formation of radial inhomogeneity to the rate of thermal stabilization and fiber diameter was carried out on as-electrospun PAN nanofibers i.e. 1x case of nanofibers. Hence, taking into consideration the relative cyclization of the PAN nanofibers as well as the structure developed in the subsequently fabricated carbon nanofibers, for the case of the as-spun (1x) nanofibers, 265°C for 2 hours is concluded to be the optimum stabilization conditions. Other factors analyzed led us to change this temperature range for hot-drawn samples as will be explained in Section 3.3.1.

Adjusting the stabilization conditions of PAN for hot drawn fibers: According to the results discussed in the previous section for stabilization of as-electrospun fibers, selecting a temperature above 245°C and below 295°C will result in highly stabilized fibers. However, the formation of the crystalline domains in hot-drawn samples can drastically influence the kinetics of thermal stabilization. To study this effect, fibers that were hot drawn upto 2x and 4x times after electrospinning were subjected to the same study as the previous section to understand the effect of stabilization on hot drawn nanofibers. This study is an essential step prior to carbonizing the fibers to achieve similar degrees of cyclization for different fibers and for a systematic study of the effect of hot-drawing on mechanics of nanofibers. Figure 3.16 and Figure 3.17 show the FTIR curves for the 2x and 4x hot drawn nanofiber ribbons, stabilized at temperatures of 135°C, 220°C, 245°C, 265°C, 280°C and 295°C. Using Equation 4, the RCI for hot drawn fibers is calculated. Stabilization temperatures below 200°C have little or no effect on the stabilization reactions.

The RCI calculated using Equation 3.1 for hot drawn nanofibers, seen in Figure 3.18, shows a similar trend at low temperatures when compared with the 1x fibers. However, at temperatures above 180°C, it can be seen that RCI for the hot drawn fibers is lower than that of the as-spun fibers. As the temperature of stabilization is increased, there continues to be a considerable difference in the RCI for hot drawn and as-spun fibers, with the RCI for 2x and 4x being consistently lower than 1x with this difference reducing at 295°C.

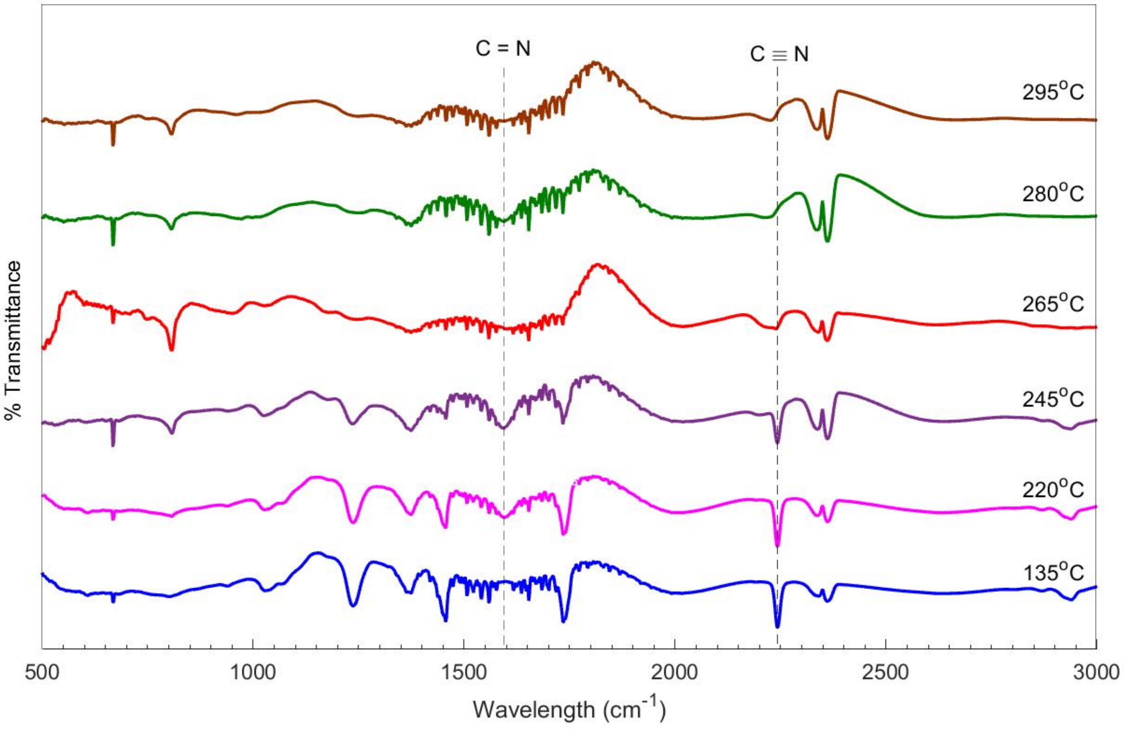

Figure 3.16: FTIR spectra for 2x hot drawn PAN nanofibers stabilized at various temperatures

The RCI calculated using Equation 3.1 for hot drawn nanofibers, seen in Figure 3.18,

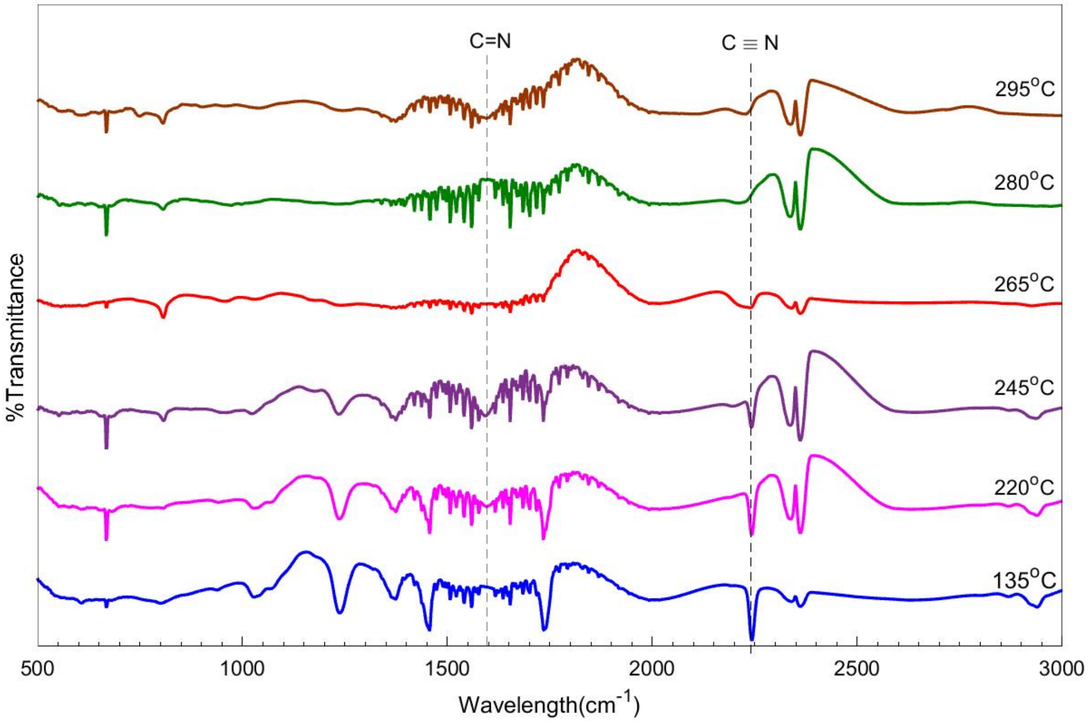

Figure 3.17: FTIR spectra for 4x hot drawn PAN nanofibers stabilized at various temperatures

shows a similar trend at low temperatures when compared with the 1x fibers. However, at temperatures above 180°C, it can be seen that RCI for the hot drawn fibers is lower than that of the as-spun fibers.

As the temperature of stabilization is increased, there continues to be a considerable difference in the RCI for hot drawn and as-spun fibers, with the RCI for 2x and 4x being consistently lower than 1x with this difference reducing at 295°C. At 295°C, the high amount of cyclization of the skin, and the rate of stabilization can result in comparable and rather high RCI. However, from previous TEM results, at higher stabilization temperatures, there is a risk of obtaining hollow fibers, or fibers with incompletely stabilized core regions. According to previous analysis, stabilization temperature of 265°C was determined to be ideal for stabilization of the 1x fibers. At this temperature, the 1x fibers have an RCI of 91.4%, while the RCI of the 2x and 4x stabilized fibers is 86.4% and 72.64% respectively.

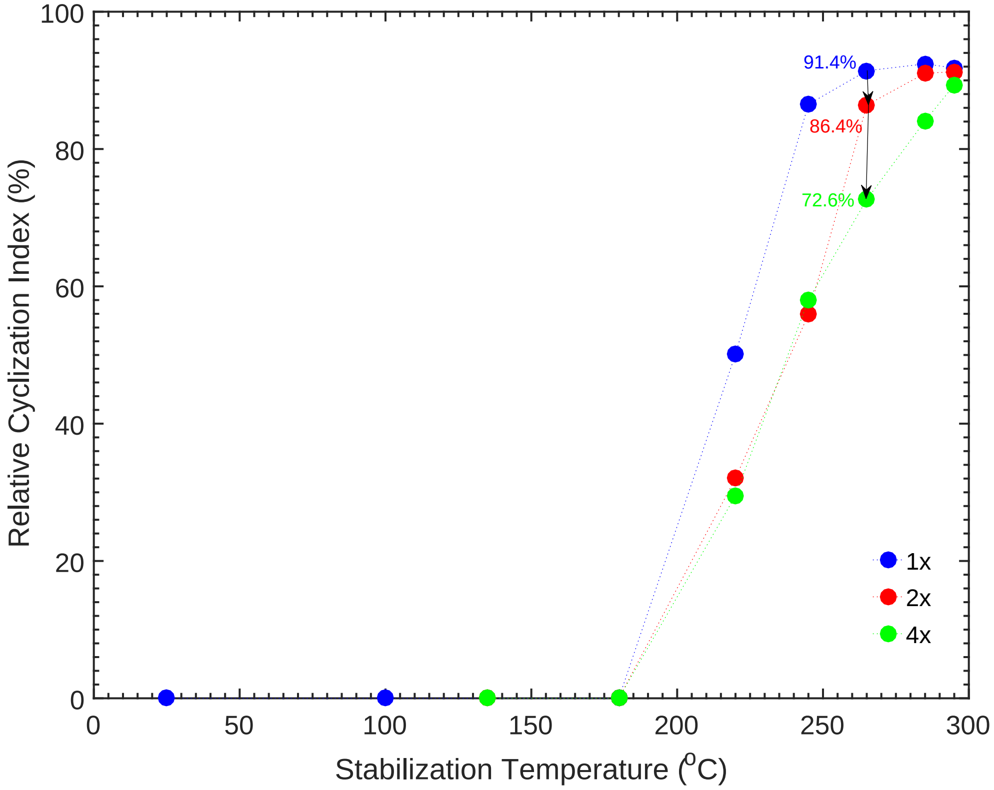

Figure 3.18: Relative cyclization index (RCI) for 1x, 2x and 4x hot drawn nanofibers

To explain these results, we studied thermally induced phase changes in as-electrospun and hot-drawn PAN via Digital Scanning Calorimetry (DSC). DSC was performed at heating rates of 10°C/min from 40°C to 350°C in air. The nanofibers were initially heated upto 120°C and cooled to room temperature to remove any thermal history in the fibers. From the DSC results in Figure 3.19, it is evident that the temperature of decomposi-

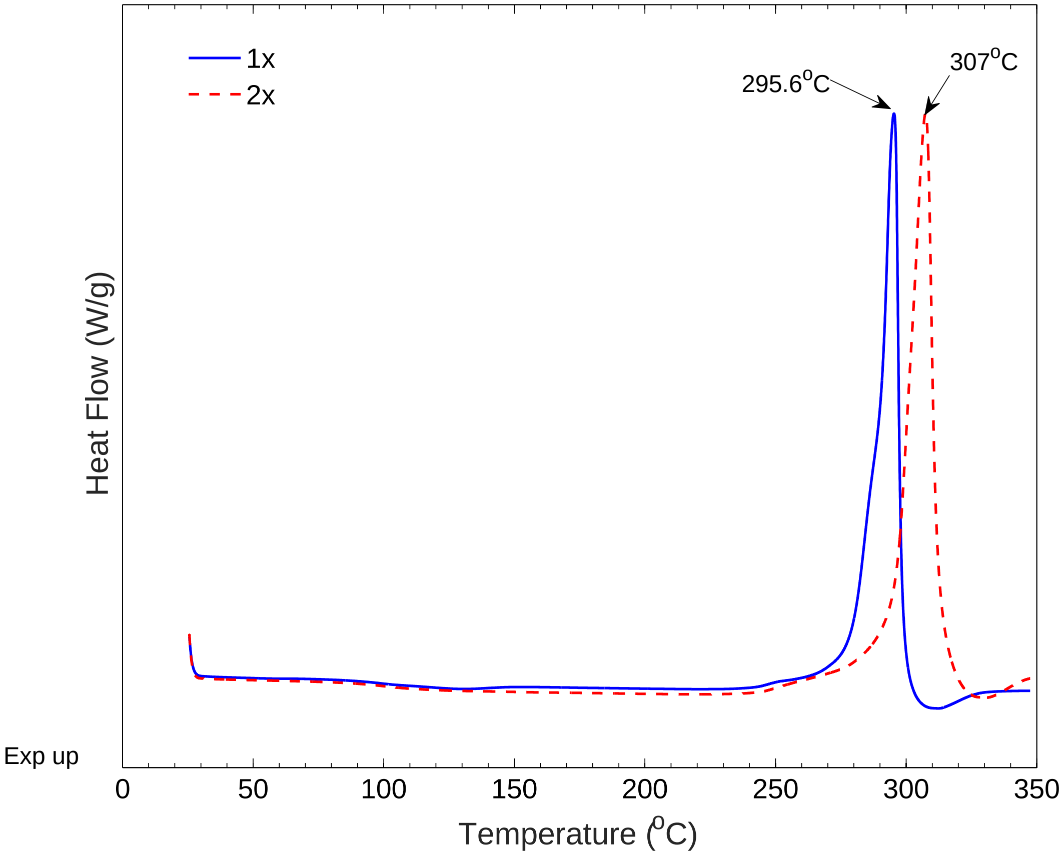

Figure 3.19: DSC curves for 1x and 2x nanofibers

tion of the PAN nanofibers increased from 295.6°C for 1x nanofibers to 307°C for hot drawn 2x nanofibers. Thus, hot drawing plays a key role in the amount of cyclization and decomposition temperature, which can be attributed to the effect of hot drawing on the microstructure of the nanofibers. That is, hot drawing increases the concentration of crystalline domains in the fiber. As a result of this, more heat is required in order to provide the molecules sufficient energy to reconfigure from the crystalline phase and form bonds with adjacent molecules. This conclusion is in line with prior studies who suggest that thermal stabilization and cyclization starts in the amorphous phase [145, 146, 147]. Thus, to achieve similar degrees of stabilization in fibers fabricated with different hot-drawings, the thermal stabilization parameters were modified as a function of hot-drawing ratios.

Modified stabilization conditions for hot drawn nanofibers: As demonstrated in the previous section, the formation of the crystalline domains in hot-drawn samples delayed thermal stabilization. Thus, it is clear that the heat treatment conditions have to be a function of the drawing ratio to ensure similar RCI values. High temperature of heat treatment could not be used since that can lead to non-homogeneous cyclization through the fiber transverse direction and the formation of skin-core structure or hollow fibers (Section 3.3.1). Thus, step stabilization process was adopted such that nanofibers were heated starting at 265°C for 2 hours to obtain cyclization throughout the fiber cross-section as seen before, and then further heated to higher temperature to increase the amount of cyclization in the fibers. Several combinations of temperatures between 265°C and 295°C with varying times were tested and RCI was calculated for fibers which were hot drawn to different drawing ratios. RCI for these conditions is seen in Figure 3.20.

Two different combinations for step stabilization were used in order to obtain RCI above 90%. The aim was to combine the advantages of high and medium stabilization temperature (265°C) which allows the fiber to be stabilized uniformly through the transverse direction, and high temperature, which permits improved cyclization. All fibers were stabilized at two conditions, condition I, 265°C for 2 hours + 275°C for 2 hours, and condition II, 265°C for 2 hours + 275°C for 2 hours + 285°C for 2 hours. The RCI for both is plotted in Figure 3.20. For the 1x nanofibers, condition I proved sufficient to yield >90% RCI. However, 2x and 4x cases did not achieve the required RCI. In condition II, 1x did not see much improvement, however, 2x and 4x fibers saw fair amount of improvement in cyclization, raising their RCI to above 90%. Using this analysis ensured that the nanofibers chosen for further studies had comparable RCI's controlled by the stabilization conditions. The following stabilization cycles were finally chosen (Figure 3.21).

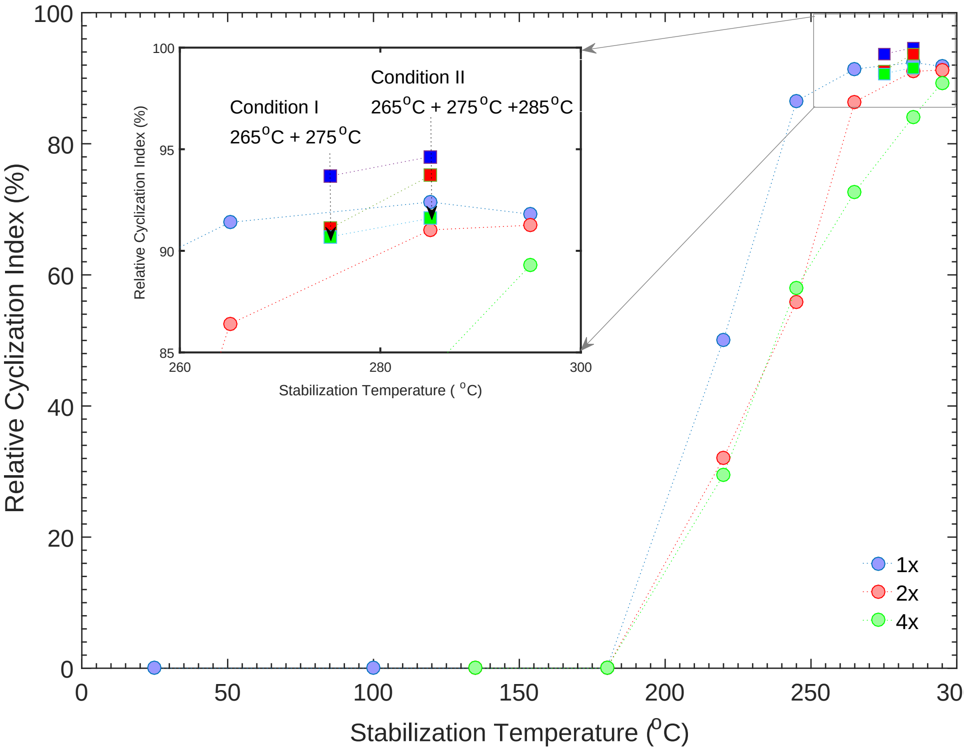

Figure 3.20: RCI for 1x, 2x, 4x nanofibers with step stabilization

1x: 265°C for 2 hours + 275°C for 2 hours

2x: 265°C for 2 hours + 275°C for 2 hours + 285°C for 2 hours

4x: 265°C for 2 hours + 275°C for 2 hours + 285°C for 2 hours

The RCI values obtained for these cases is seen in Table 3.2. It is believed that stabiliza-

Hot Draw Ratio	Stabilization Condition	RCI%
1x	265°C(2h)+275°C(2h)	93.6
2x	265°C(2h)+275°C(2h)+285°C(2h)	91.1
4x	265°C(2h)+275°C(2h)+285°C(2h)	90.7

Table 3.2: Relative cyclization index (RCI) of final set of nanofiber ribbons that were carbonized

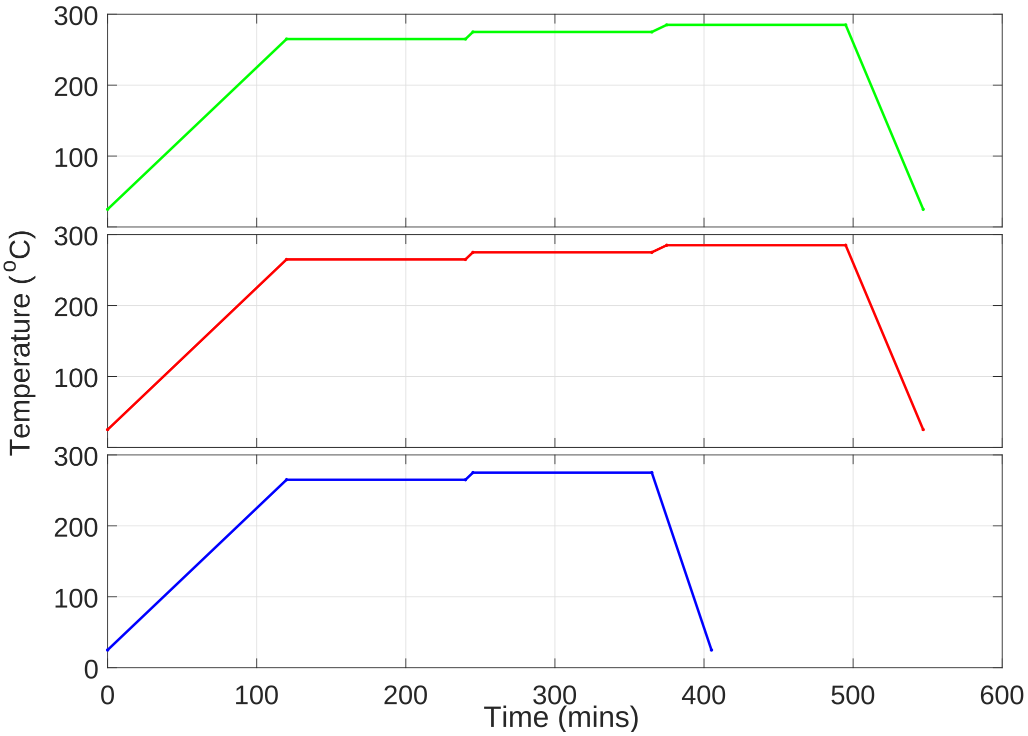

Figure 3.21: Stabilization cycle used for (a) 1x, (b) 2x, (c) 4x nanofibers

tion begins in the amorphous phase and then moves to the crystalline phase [145]. The amount of crystallinity in hot drawn nanofibers is more than that in as-spun nanofibers. As a result, the hot drawn nanofibers attain lower amounts of cyclization when subjected to the same stabilization cycle as the as-spun nanofibers.

In addition to RCI, the cross section of various nanofibers was observed to ensure that there was no existence of hollow fibers. For this purpose, the above discussed stabilized nanofibers were converted to carbon nanofibers using the method discussed in Section 3.3.2. As seen in Figure 3.22, the nanofibers show no sign of hollow or depleting core and the cross section appears to be uniform. This validates the modification in the stabilization process to ensure complete stabilization of the nanofibers.

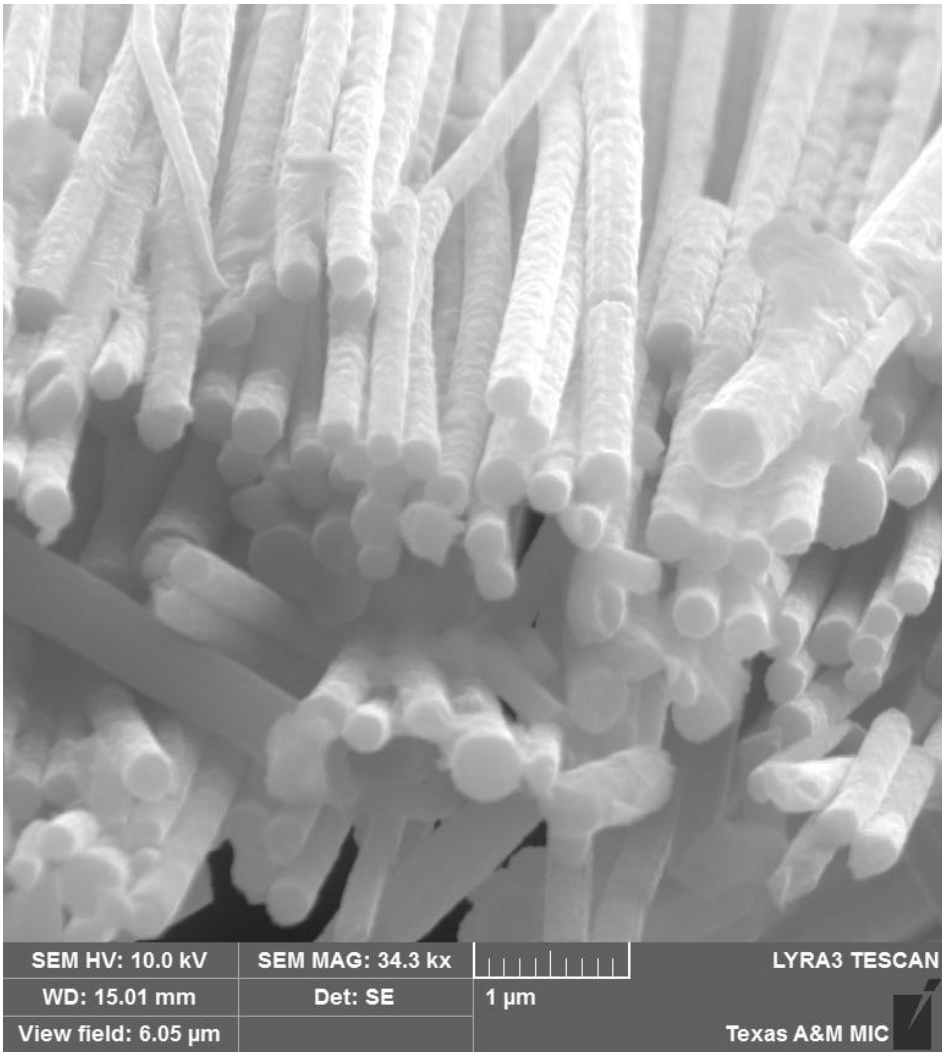

Figure 3.22: SEM image of 4x carbon nanofibers stabilized using condition II showing uniform cross-section

Selecting nanofibers that have comparable RCI values ensures that the results obtained from mechanical tests of subsequent carbon nanofibers is free from stabilization discrepancies between cases. Therefore, the improvements in strength and modulus of mechanically tested fibers can be traced back to the effect of enhancement in molecular alignment in the precursor and improved graphitic domains in the carbonized fibers.

3.3.2 Carbonization of Stabilized PAN Precursor Nanofibers

Upon completion of the stabilization process, the nanofiber ribbons were carbonized to convert them to carbon nanofibers. This process was carried out in a tube furnace, seen in Figure 3.23. The fibers were placed in an alumina crucible with the ends clamped using high temperature adhesive, to prevent shrinkage during carbonization. The crucible is placed in the tube in the region of uniform temperature. The tube is closed at both ends with pressure gages on the ends. One end, it is connected to a N_2 tank and the other end to a vacuum or open to air or to an air outlet as required. Carbonization process is carried out at 1100°C for one hour in nitrogen atmosphere. The carbonization cycle used is seen in Figure 3.24.

Figure 3.23: Tube furnace used for carbonization

Prior to beginning the carbonization, the tube was alternatively vacuumed and purged with nitrogen in order to ensure removal of oxygen molecules from the tube. Oxygen

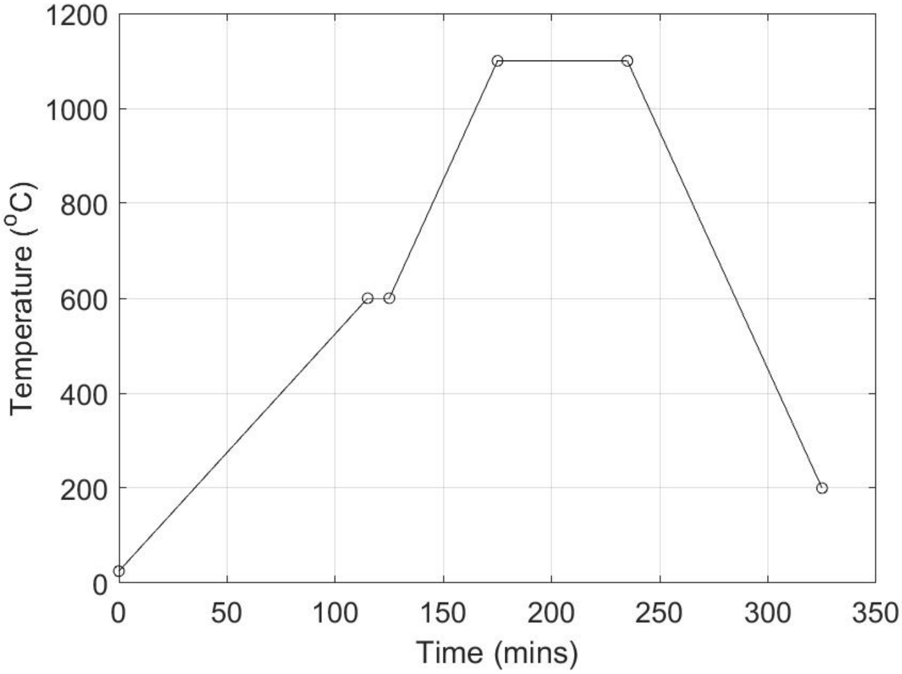

Figure 3.24: Carbonization cycle used for conversion of stabilized PAN nanofibers to carbon nanofibers

molecules present during carbonization are detrimental in the formation of carbon fibers. A continuous flow of nitrogen is vital in the production of carbon nanofibers using the tube furnace. The carbon nanofibers produced using this method have a yield of approximately 50wt% compared to the PAN precursor nanofibers. Single nanofibers were extracted from the ribbon of carbon nanofibers and tested for tensile strength and modulus, as will be discussed in Chapter 4.

Microstructure of carbon nanofibers: Carbonization enables formation of turbostratic domains in the nanofiber with the elimination of non-carbon atoms from the chains. Increase in carbonization temperature leads to improvement in turbostratic domains in the fiber. As seen in Chapter 2, hot drawing improves the molecular orientation of the chains in the PAN precursor fiber, aligning them parallel to each other and in the direction of fiber axis.

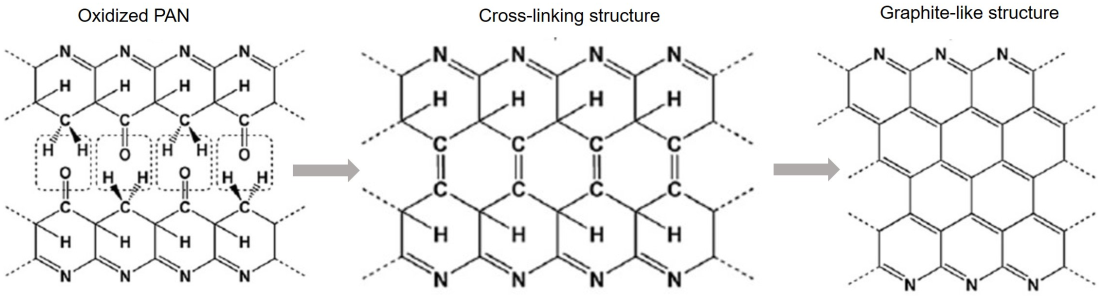

Figure 3.25: Proposed model of conversion of aligned PAN molecules forming turbostratic domains in CNF [31]

The alignment will also facilitate chain packing, as can be inferred from XRD data analysis (Section 2.2.2), such that oxygen atoms, nitrogen and hydrogen atoms in the chain can interact more readily as seen in Figure 3.25, and increasing the likelihood of crosslinking between chains by removal of hydrogen and nitrogen elements. Higher number of parallel chains should, in principle, give rise to improved turbostratic structure with improved stacking between the planes. The turbostratic domains are embedded in amorphous regions of the fibers. The amorphous carbon is created from misaligned chains or molecules that were unable to bond with other chains and form stacked sheets of turbostratic carbon. A schematic of the turbostratic domains in an amorphous matrix of the CNF are seen in Figure 3.26(a). Turbostratic domains are highlighted in the TEM image seen in Figure 3.26(b). The image studied here shows the fiber morphology and is typical of CNFs.

In order to observe the microstructure of CNFs via TEM imaging, the CNFs were sonicated for 10 minutes in an ethanol solution before being deposited on the TEM grid. The fractured surface of the CNF, transverse to the fiber cross section is the thinnest regions

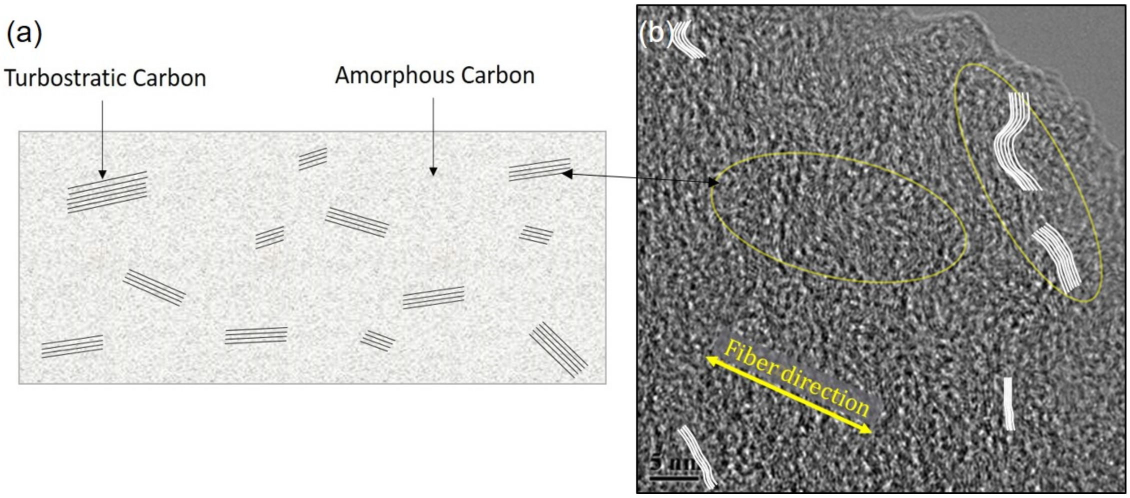

Figure 3.26: (a) Schematic of a CNF with turbostratic and amorphous domains, (b) TEM image of a typical CNF

of the fiber, and hence, used for imaging. The inner portions of the fiber appear to be more solid than the boundaries, however, this is an artifact of fiber imaging due to longer travel path of electrons from the central region of the fiber. TEM images taken for cases of 1x, 2x and 4x nanofibers are in Figures 3.27, 3.28, 3.29. Numerous observations of fracture surfaces at different locations through the fiber thickness have led us to conclude that the microstructure observed in the thinner regions in the images is similar throughout the fiber diameter and the skin-core structure commonly observed in carbon fibers (Section 1.2) is not observed in CNFs.

The TEM image of CNFs obtained by carbonization of as-electrospun PAN nanofibers (no hot-drawing, the 1x nanofibers) is shown in Figure 3.27, in which turbostratic domains throughout the nanofiber regions can be observed. The turbostratic domains appear as fine parallel lines in the amorphous matrix. Each line is a thin sheet of carbon atoms in the form of a highly defective graphene. When carefully observed, turbostratic domains are present throughout the nanofiber cross-section. They appear to be 3 to 5nm in length and few layers thick. They also appear to show small amount of preferential alignment in the

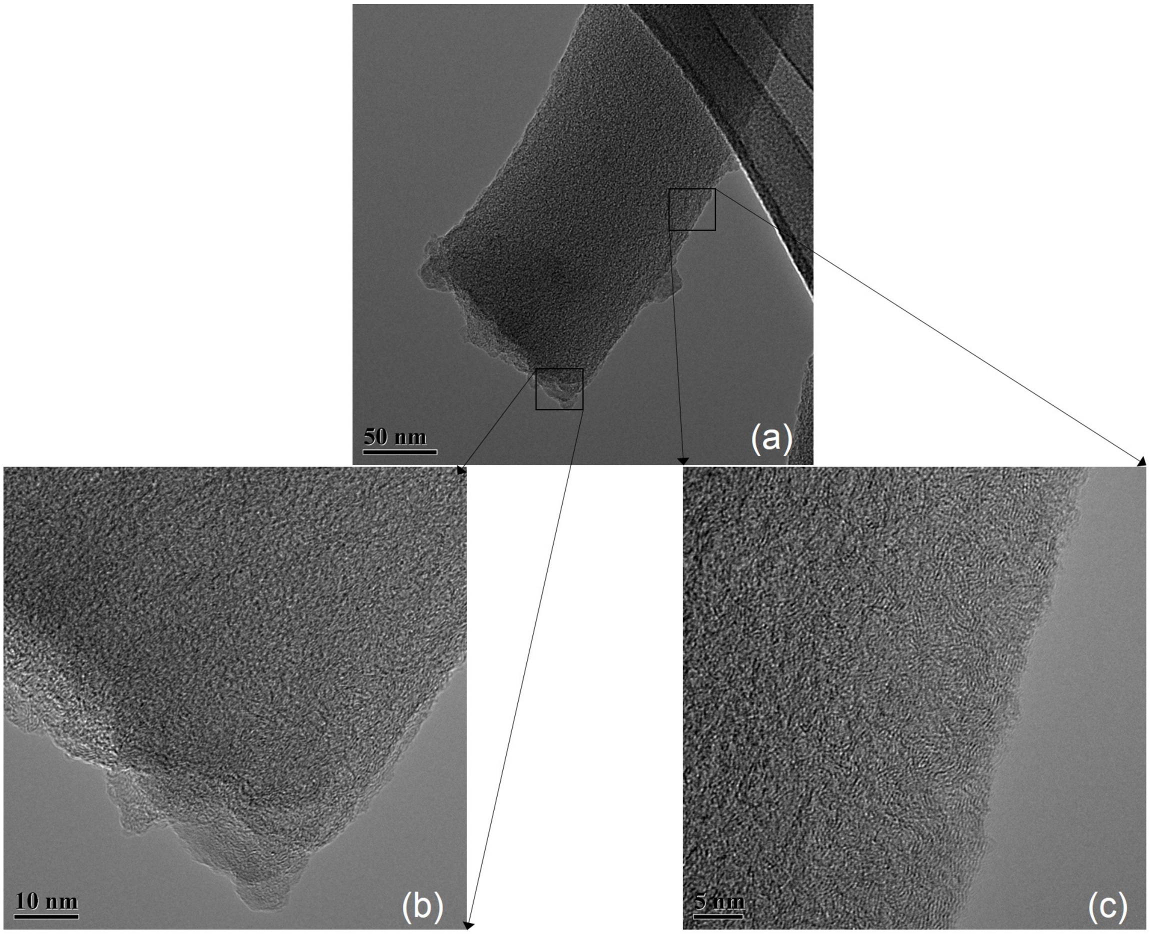

Figure 3.27: TEM image of as-spun (1x) CNF carbonized at 1100°C at (a) 71kx, (b) 285kx, (c) 450kx

direction of fiber access (Figure 3.27(c)). The latter is likely due to partial alignment of PAN chains in the as-electrospun fibers achieved due to electromechanical forces applied on the electrospinning jet.

Effect of hot drawing on microstructure of subsequent carbon nanofibers: Hot drawn PAN nanofibers, after being stabilized as discussed in Section 3.3.1 of this chapter were carbonized at 1100°C to convert them into carbon nanofibers. The TEM images of 2x and 4x hot drawn CNF are presented in Figures 3.28 and 3.29. In the hot drawn nanofibers the turbostratic domains appear to be more aligned in the direction of fiber access than the 1x fibers. Also, the length of the turbostratic domains appear to have increased considerably in length to 9nm to 12nm with some being as long as 14nm in length. Also, larger number of planes appear to be stacked on each other. In some cases as many as 8 to 10 planes are stacked, increasing the size and volume of these domains considerably.

Clearly, hot drawing of the nanofiber ribbons enhanced the alignment of the chains in the fiber direction which, on heat treatment, formed better aligned domains with more parallel chains leading to higher number of stacking planes as well as longer crystallites. The surface of the hot drawn nanofiber also shows lower roughness and surface pores. Surface morphology has been further discussed in Chapter 4.

Analysis of the electron diffraction pattern for CNF that was obtained on carbonizing the 1x nanofiber (Figure 3.30(a)) shows a homogeneous ring representing the ring for (002) plane. This plane corresponds to crystallographic distance of $\approx$0.344nm. In comparison, the (002) spacing of a graphite crystal is 0.335nm [148].

Figure 3.30(b) and (c) clearly shows the disappearance of the homogeneous ring, forming narrow arcs at $\approx$0.34nm, with the arc angle, α, scaling inversely with the draw ratio of the precursor, as in Table 3.3, indicating an improved alignment of the (002) plane of turbostratic domains with the fiber axis.

Hot Draw Ratio	**FWHM**	**Orientation Index**
1x	84°	0.53
2x	52°	0.71
4x	48°	0.73

Table 3.3: Orientation index of CNFs with hot drawing ratio 1x, 2x, 4x

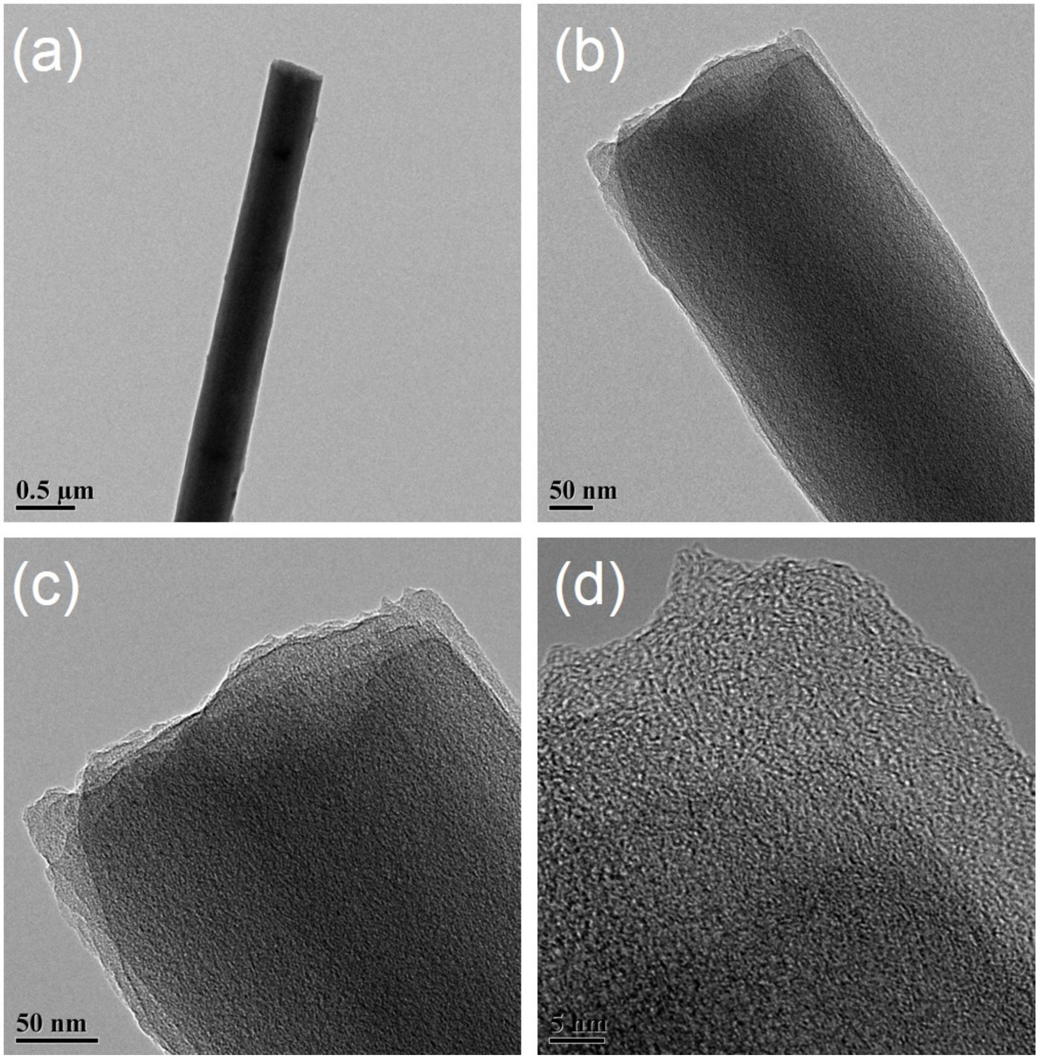

Figure 3.28: TEM image of 2x hot drawn CNF carbonized at 1100°C at (a) 5x, (b) 38kx, (c) 71kx, (d) 450kx

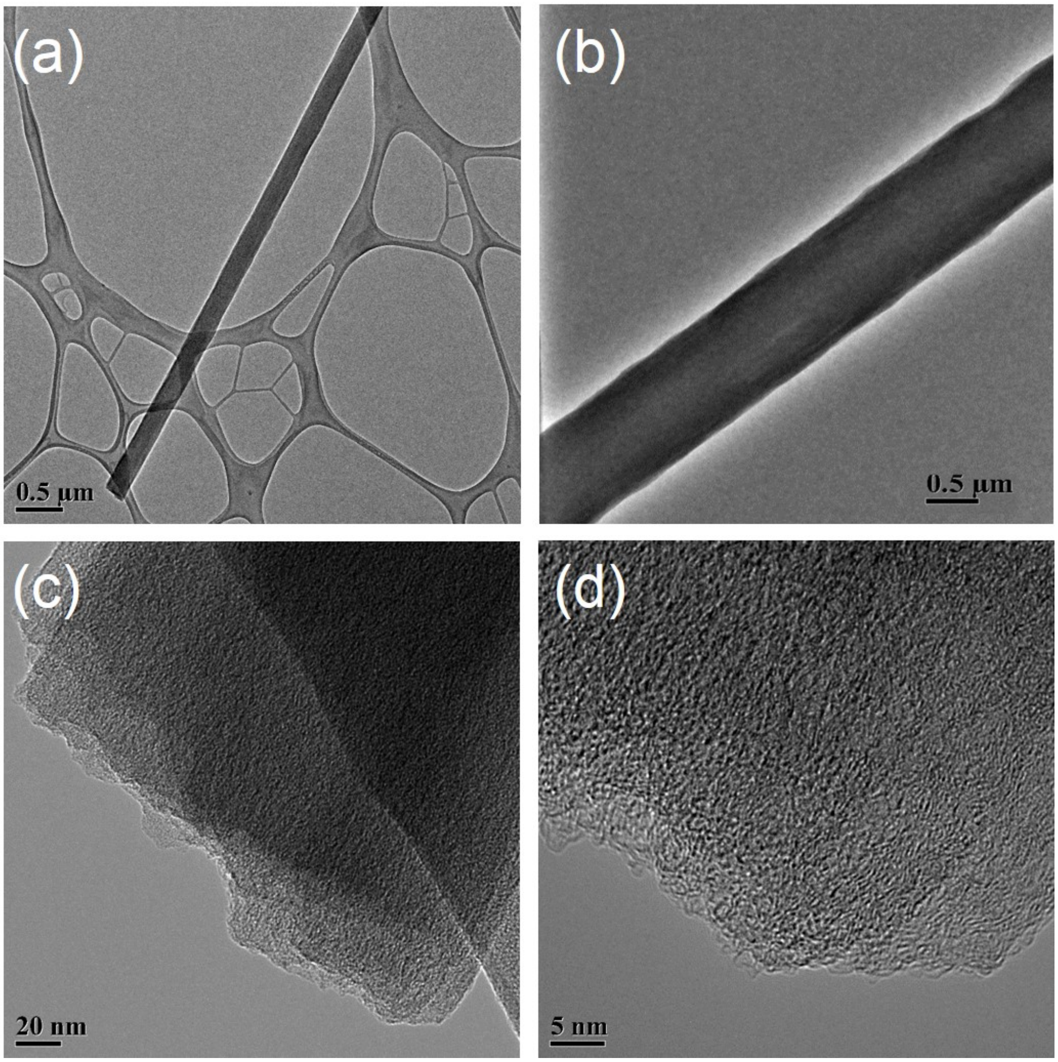

Figure 3.29: TEM image of 4x hot drawn CNF carbonized at 1100°C at magnification (a) 5x, (b) 38kx, (c) 97kx, (d) 450kx

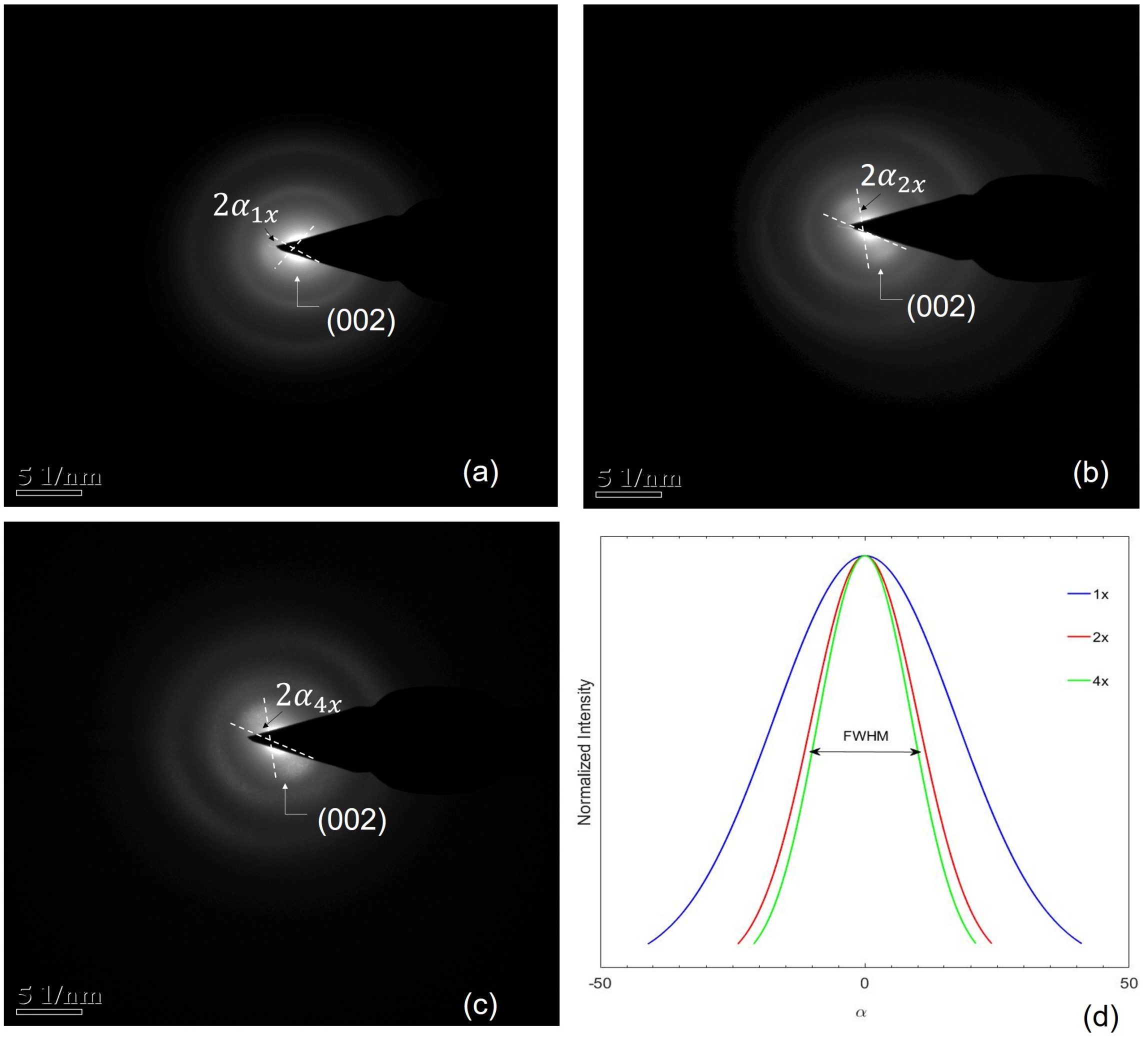

Figure 3.30: Diffraction patterns of (a) 1x, (b) 2x, (c) 4x CNF, (d) intensity plot of diffraction pattern at 0.34nm (002) plane

3.4 Conclusion

In this chapter, as-spun and hot drawn polymer nanofibers have been heat treated to convert them into carbon nanofibers. The heat treatment stages of stabilization and carbonization have been discussed in detail. Hot drawing alters the crystallinity of the nanofibers, thus playing a key role in the amount of cyclization that can take place in the nanofiber during the stabilization process. In order to optimize the stabilization conditions for the as-spun (1x), and hot drawn (2x and 4x) nanofibers, different stabilization cycles have been studied. The optimum stabilization of the nanofibers yielded relative cyclization index of above 85% for all nanofibers. After stabilization, the nanofibers were heated to higher temperatures of 1100°C in a nitrogen atmosphere in a tube furnace to convert them into their carbon forms. FTIR, TEM and XRD have been used for to evaluate the cyclization of the nanofibers and to study the orientation and spacing of the turbostratic domains respectively. The microstructure of the CNFs obtained from 1x, 2x and 4x cases of hot drawn fibers have been discussed in detail. Increase in turbostratic domains in the nanofiber as observed by TEM images have been shown. Using spectroscopic methods, improvements have been evaluated in the alignment and presence of turbostratic domains in the carbon nanofibers.

In the next chapter, the effect of this improvement in turbostratic domains on the mechanical strength and Young's modulus of single carbon nanofibers will be discussed. Single CNFs will be extracted from the CNF ribbon and tested for mechanical properties using a Microelectromechanical Systems (MEMS) device.

4. MECHANICAL TESTING OF SINGLE CARBON NANOFIBER

4.1 Introduction

One dimensional nanofibers are used primarily for their axial strength. Due to their small dimensions, the use of conventional tensile testing equipment to characterize their mechanical properties is not feasible. Over the years, researchers have developed methods for testing these nanofibers including the use of AFM cantilevers, 3-point bending tests [17, 92, 149, 150], nanoindentation [151, 152] and use of micro-electro-mechanical systems(MEMS) devices [153, 154, 155].

AFM cantilever tips of different stiffnesses are available allowing testing of nanofibers with different stiffnesses. Strength and modulus of nanofibers can be measured using this method. However, a prominent drawback of this method is the possibility of off-axis cantilever motion in tests involving large elongations. In addition, local bending of the fiber at grips can cause the fiber to fail prematurely at stress concentration end points, leading to erroneous values of strength. Zussman et. al. [156] were the first to perform mechanical tests on PAN derived single carbon nanofibers using the AFM method. They tested nanofibers with diameters of $\approx$ 200nm.

Nanoindentation is a fairly simple and straightforward method to provide mechanical properties of materials. In the past, researchers have used this method to test the elastic modulus of nanowires and nanofibers [149]. Although this method does not require relatively elaborate sample preparation, it presents its fair amount of drawbacks, rendering it inapplicable to provide tensile properties. Nanoindentation provides localized values of stress-strain and is highly dependent on location on in sample and surface morphology and curvature of the fiber. This method provides measurement of hardness and does not give direct results of strength.

Likewise, bending tests measure the flexural modulus and strength of nanofibers. Due to their small dimensions, it is difficult to prevent the sliding or rotating of nanofibers at the location of the grip, leading to inaccurate measurements.

These drawbacks paved the way for development of MEMS devices. Due to the planarity of the MEMS platform, off-axis bending is significantly suppressed. In addition, MEMS devices have the advantage of using symmetric loadcells and linear actuators to provide in plane testing platform for 1D nanostructures. MEMS devices are used in conjunction with SEM imaging or optical imaging to provide high level of resolution for the testing of nanofibers. Digital Image Correlation (DIC) [157] technique is used to measure the in plane movement of the load cell and elongation of the nanofibers. Using this method, force and displacement of the specimen are obtained, giving the tensile stress and modulus of 1D nanostructures.

In this chapter, mechanical testing of single CNFs were performed using a MEMS based platform to investigate their tensile strength and modulus. The device uses a compliant polysilicon beams as the loadcell, and the fiber elongation and tensile force were obtained using 2D DIC software from Correlated Solutions Inc. Results from these tests are discussed for the cases of CNFs obtained from four different precursor treatments: (a) as electrospun PAN nanofibers were ungripped during thermal stabilization (1xU), (b) as electrospun PAN nanofibers were gripped during thermal stabilization to minimize chain relaxation (1x), and PAN nanofibers hot-drawn to draw ratios of (c) 2x and (d) 4x nanofibers, gripped during stabilization. The results are discussed in the context of fiber surface morphology, fiber failure and failure surface studied via SEM imaging and electron diffraction.

4.2 Experimental Method

Mechanical characterization of individual CNFs was performed via micromachined devices which were equipped with compliant silicon beams with known stiffness and were actuated via a picomotor©actuator. Different parts of the device which facilitated mechanical characterization of nanofibers and our approach for data acquisition are described in details in this chapter. To perform the mechanical characterization, small sections ($\approx$a few millimeters) of the carbonized nanofiber ribbons were cut using a sharp razor blade and mounted on a glass slide. A sharp tungsten probe was used to separate the fibers under the microscope. A micro manipulator was used to place the probe in position to lift the fiber, and place it on the MEMS device. The MEMS device, seen in Figure 4.1, was one of several devices designed and fabricated on a chip. The device used for this test is configured for tensile testing, with the loadcell stiffness value appropriate to test a single carbon nanofiber. Employing stiffer loadcells will diminish force measurement resolution, while more compliant ones may break prior to the failure of the fiber. Tensile tests on CNFs were performed on a device with three folded beams in series, each folded beam with a stiffness of 46 N/m resulting in a total stiffness of 15.33N/m for the loadcell. The stiffness of the beam is calculated based on the geometry of the beam measured in SEM and known modulus of silicon. Individual nanofibers are mounted on the device between platforms marked U_1 and U_2 in Figure 4.1.

Initially, the fibers are mounted using epoxy droplets to hold them in place. However, epoxy does not possess enough stiffness and strength to keep a CNF in place during the tension test upto failure. To ensure a stronger grip on the fiber, blocks of Platinum were deposited on the fiber ends using Focused Ion Beam (FIB). The blocks are approximately 500nm - 800nm in height with in plane dimensions of 4μm $\times$ 4μm. Top and side views of the Pt blocks can be seen in Figure 4.2.

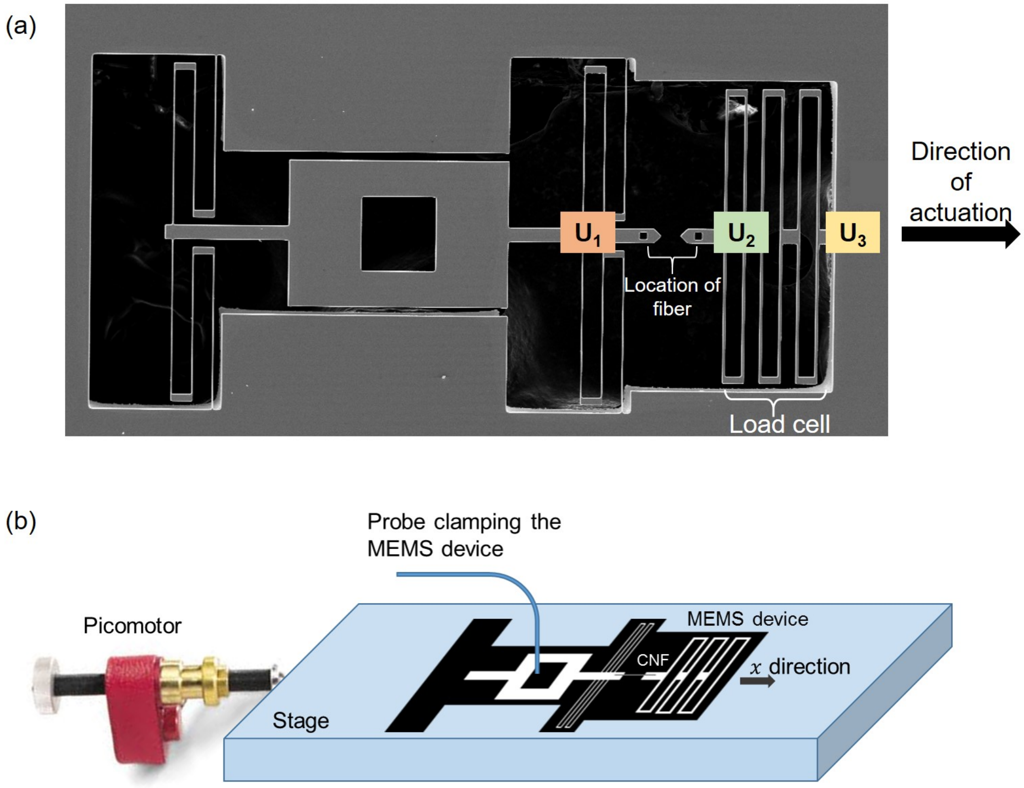

Figure 4.1: (a) MEMS device used for testing single nanofibers, (b) schematic of test setup using MEMS device and picomotor

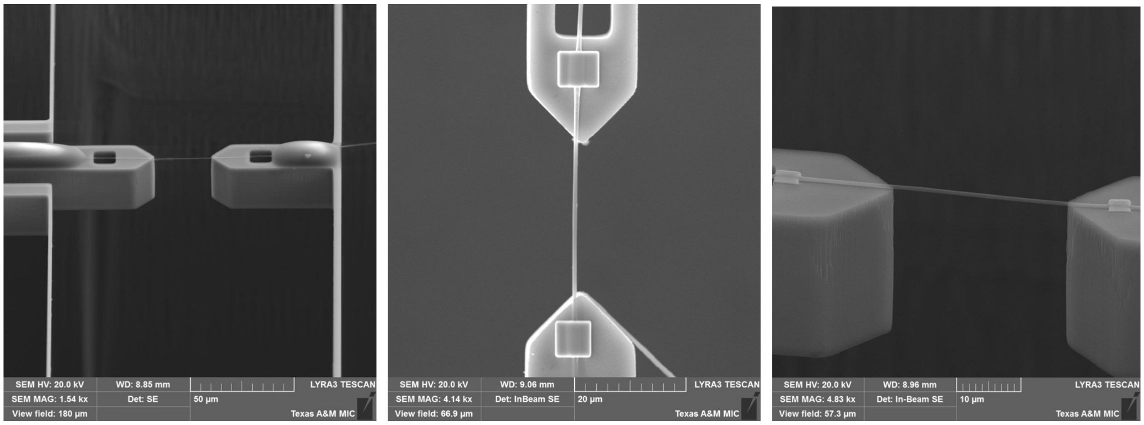

Figure 4.2: Top and side view of Pt blocks deposited using focused ion beam (FIB)

Tescan LYRA-3 Model GMH Focused Ion Beam is used for this purpose. Once the FIB blocks were deposited on the fiber, the fiber was ready for testing.

4.2.1 Testing Method

The MEMS device with the mounted fiber and Pt blocks was placed on a stage with motion in x-direction. The motion was applied and controlled by a picomotor from Newport Corporation. The stage with the MEMS device was placed under an optical microscope for testing.

One end of the MEMS device was held in place using a probe with adequate stiffness to constrain the device. As seen in the schematic in Figure 4.3, the picomotor applies displacement in the x-direction which was transferred onto the nanofiber through the load cells on the MEMS device. Using this method, a constant incremental strain was applied on the nanofiber though displacement of the stage using the picomotor actuator©, until the fiber failed.

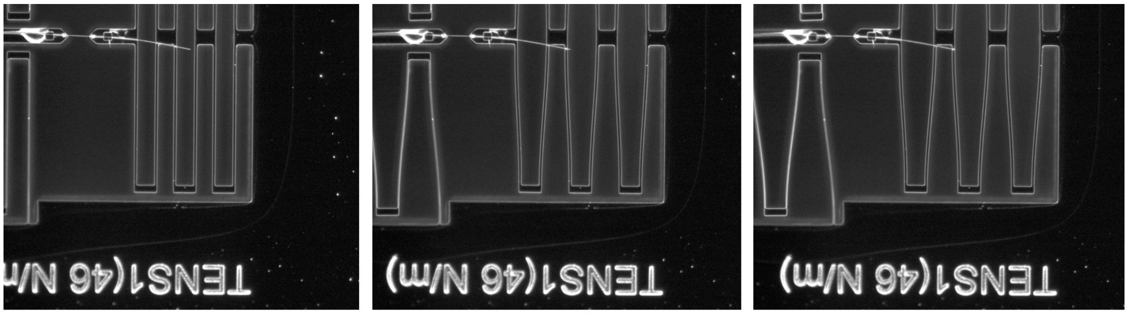

Initial position
$\varepsilon = 0\%$

$\varepsilon = 0.8\%$

Final position
$\varepsilon = 1.23\%$

Figure 4.3: Images at magnification 20x at three time steps during testing

The force applied on the nanofiber and the extension of the nanofiber were calculated by recording the optical images of the actuated device and nanofiber under an optical microscope, including the platforms onto which the fiber was anchored, followed by correlating the digital images via a commercial digital image correlation (DIC), vic2D. Images were taken at the rate of 1 image/second at magnification of 20x. This configuration allowed the device to have an extensional measurement resolution of 20nm (about 10% of the pixel size) without the use of a scanning electron microscope. The MEMS device used for these experiments had the ability to measure forces in the range of 300nN - 300μN and displacements in the range of 20nm - 100μm. The force resolution was estimated as the product of the stiffness and the extensional resolution. For a 25μm long and 300nm c/s nanofiber, this extensional resolution corresponds to better than 0.1% strain resolution. Moreover, the displacement resolution of 20nm corresponds to better than 0.3 μN force resolution (the product of the displacement resolution and loadcell stiffness), which is equivalent to $\approx$4 MPa. The strain and force resolution of respectively 0.1% and 4 MPa are suitable to capture the stiffness and strength of carbon nanofibers with strength exceeding 1GPa and strain to failure of over 1%. An example of the test at three time instants is shown in Figure 4.3.

$$u_l = U_3 - U_2 \tag{4.1}$$

$$u_f = U_2 - U_1 \tag{4.2}$$

The stiffness of the loadcell, k_l is 15.33 N/m. The applied force on the loadcell is calculated as the stiffness times the deflection of the loadcell, and the stress on the fiber is given by

$$\sigma = \frac{k_l u_l}{A_f} \tag{4.3}$$

The initial gage length of the fiber and the fiber diameter were measured using SEM.

The fiber has a nearly circular cross-section, and the cross-section area of the nanofiber is given by $A_f = \pi r^2$. Strain on the fiber is given as the ratio of the fiber extension over its initial length, l_0, as:

$$\epsilon = \frac{u_f}{l_0} \tag{4.4}$$

4.3 Results and Discussion

Using the method described in the previous sections, we studied the mechanical properties of single CNFs. We considered four types of CNFs mainly differing in their precursor treatment procedures, as listed below:

- 1xU: The precursors of these CNFs were the as-electrospun PAN nanofibers, and the samples were ungripped during thermal stabilization, allowing for entropic polymer chain recoiling and free shrinkage,
- 1x: The precursors of these CNFs were the as-electrospun PAN nanofibers, and the samples were gripped during thermal stabilization to limit polymer chain recoiling,
- 2x: As-electrospun PAN nanofibers were HOT drawn to a draw ratio of $\lambda = 2$ to enhance chain alignment, and the samples were gripped during thermal stabilization to limit polymer chain recoiling,
- 4x: Similar to 2x, except that the draw ratio of the precursor was $\lambda = 4$ to further enhance chain alignment.

As stated in Chapter 3, the stabilization conditions for different samples was a function of the precursor treatment, and it was set such that the ring cyclization index (RCI-a measure of degree of stabilization) for all samples are nearly identical. Since the carbonization temperature for all samples was the same (1100°C), the designated names of samples (1xU, 1x, 2x and 4x) which mainly represents the thermomechanical treatments on precursor nanofibers are also used to describe the end product, i.e., CNFs. Moreover, the 1xU samples are considered here to be the reference samples potentially with randomly oriented turbostratic domains as compared to 1x which have a preferential chain alignment with respect to fiber axis. The latter will be a consequence of electromechanical drawings imposed on the polymer solution during electrospinning. The diameter of fibers tested lies in the range of 100-800nm.

4.3.1 Mechanical Properties of Single Carbon Nanofibers

Examples of the stress-strain plot for representative tests of 1xU, 1x, 2x and 4x CNFs is shown in Figure 4.4. The curve for the 1xU fiber is highly linear at strains below 1%, while slight yielding and strain hardening can be observed at higher strains. In all cases, the linear (or nearly linear) stress-strain behavior continued until failure at strains of ≈1.5-2.5%, and the failure was abrupt brittle failure. The maximum strength observed is 5.4GPa, which is the highest reported to date of single CNFs fabricated from pure PAN precursor with gage length of ≈25μm or more.

Hot Draw Ratio	**Modulus (GPa)**	**Strength (GPa)**	**Strain to failure**
1xU	88 ± 18.9	1.3 ± 0.6	1.9 ± 0.6
1x	122 ± 11	1.8 ± 0.6	1.6 ± 0.5
2x	209 ± 33	3.6 ± 0.5	2.2 ± 0.5
4x	209 ± 47.7	3.8 ± 1.0	2.4 ± 0.3
%Improvement of 1x w.r.t 1xU	38.4%	36%	-12%
%Improvement of 2x w.r.t 1xU	137%	169%	16%
%Improvement of 4x w.r.t 1xU	137%	190%	30%

Table 4.1: Average values of modulus, strength and strain to failure obtained in tensile tests of 1xU, 1x, 2x and 4x single carbon nanofibers

The average and maximum values of single CNF strength and modulus for each precursor treatment case is presented in Table 4.1 and 4.2, respectively. The average values,

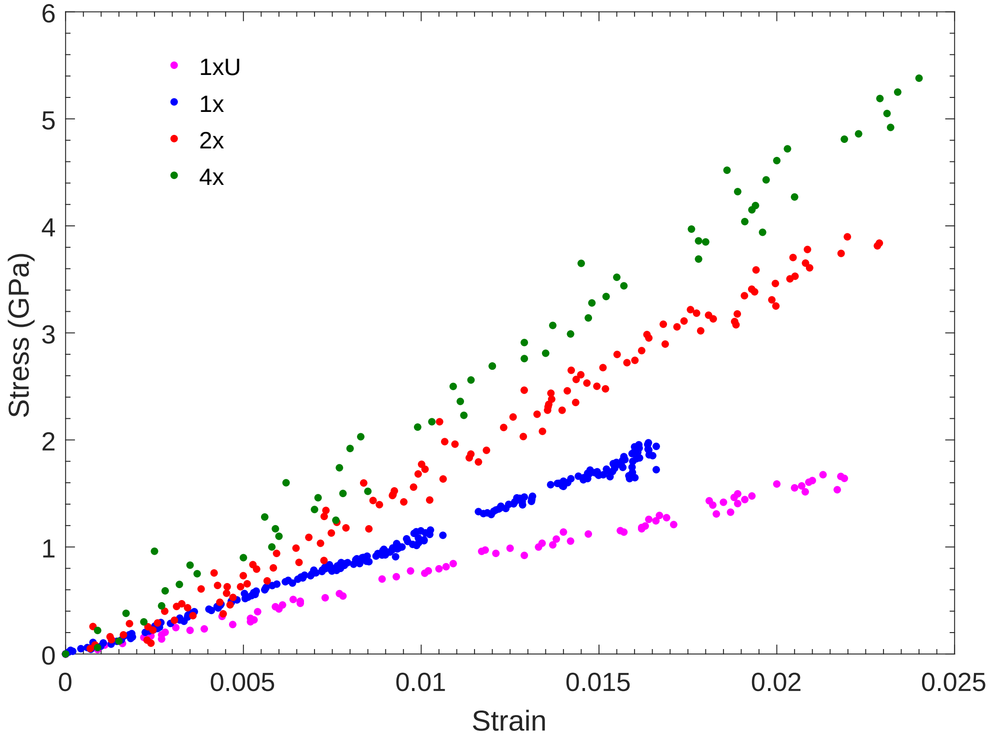

Figure 4.4: Stress strain plots of 1xU, 1x, 2x and 4x single CNF

as well as the maximum values in each case, point to a significant improvement in strength and modulus. It is such that the hot-drawing of the precursors to 4x has led to 137% and 190% increase in average modulus and strength. The improvement in properties in the 1x fibers compared to 1xU (as electrospun fibers, respectively gripped and ungripped during heat treatment) can be attributed to the orientation of PAN chains in the as electrospun fibers that is maintained in the gripped samples. This is in contrast to the ungripped samples which shrink significantly (30-40%) during thermal stabilization mainly due to entropic forces. The gripping of the sample will counter entropic chain relaxation during thermal stabilization, and as a result more aligned ladder structures will form, which leads to the alignment of turbostratic domains upon carbonization (Chapter 3).

The enhancement of strength and modulus in gripped samples by increasing the draw ratio from $\lambda = 1$ to $\lambda = 4$ can also be explained using similar arguments. In other words, hot drawing of the precursor increases the chain alignment in PAN nanofibers, as demonstrated and discussed in Chapter 2 from the polarized FTIR data. In the cases of 2x and 4x samples, part of the aligned chains are within the crystalline domains (Chapter 2), which can further assist with maintaining chain alignment during thermal stabilization (Chapter 3). The alignment of chains facilitates the formation of cross links and cyclization between chains, such that during carbonization they can more readily transform into turbostratic domains with their basal planes aligned with the fiber axis, in line with the electron diffraction pattern of CNFs and its dependence on precursor hot-drawing (Section 3.3.2). Thus, the stronger $C-C$ bonds in the basal planes of turbostratic domains translate into stronger and stiffer fibers in macroscale. Since the improvement in strength and modulus are both attributed to turbostratic domain alignment, it is not surprising that a one-to-one correspondence is observed between them (Figure 4.5).

Hot Draw Ratio	**Max Modulus(GPa)**	**Max Strength(GPa)**	**Max Strain to fail**
1xU	104	2.1	0.0241
1x	142	2.7	0.0244
2x	266	4.0	0.0295
4x	287	5.4	0.0295

Table 4.2: Maximum values of modulus, strength and strain to failure obtained from tensile tests of 1xU, 1x, 2x and 4x single carbon nanofibers

Among all the types of CNFs tested, the non-linear mechanical behavior (minor yielding followed by strain hardening) was more evident in the case of CNFs obtained from ungripped precursors with least oriented turbostratic domains. This trend suggests that the nonlinear behavior of the CNFs is rooted in the strain-induced reorientation of the domains, which is initiated at sufficiently high strains when the stress levels in the amorphous

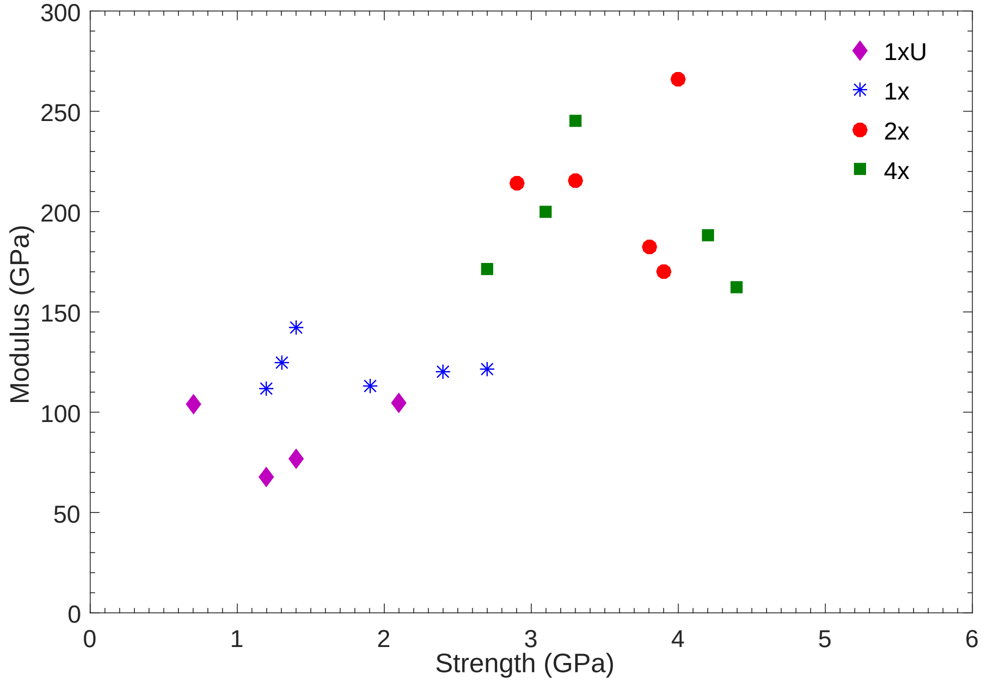

Figure 4.5: Strength and modulus of single CNF of 1xU, 1x, 2x and 4x

matrix reach a certain value. The reorientation of chains is a deformation mechanism in addition to bond stretching which can add to the compliance of the fibers.

It is also interesting to note that the improvements in mechanical properties of CNFs when the draw ratio of precursor is increased from $\lambda = 2$ to $\lambda = 4$ (2x and 4x samples, respectively), is rather marginal, as observed in Figure 4.6, 4.7, 4.8. Several factors can contribute to this effect. First, as shown in Chapter 2, the differences in degree of crystallinity and chain alignment between 2x and 4x samples is marginal when compared to changes in crystallinity and chain alignment achieved as a result of drawing the as electrospun samples to $\lambda = 2$ (Table 2.4, 2.6). This analysis suggests that no major chain alignment takes place at draw ratios larger than $\lambda = 2$, which could be explained by considering the loss of chain mobility as a result of orientation-induced crystallization at draw ratios of $\lambda = 2$ or below and the consequent loss in chain mobility. Assuming that the cause of turbostratic domain alignment in CNFs is the alignment of PAN chains in the precursor, the insignificant differences in the latter can lead to marginal changes in the former, as directly evidenced in the electron diffraction patterns of CNFs (Figure 3.30). Second, drawing the samples to $\lambda = 4$ may have led to chain scissor or other microscale defects such as void formation, partly due to orientation induced crystallization and consequent loss of chain mobility, which can lower the strength of the CNFs. While we did not directly detected these defects, we noticed that some of the PAN nanofibers among the bundles drawn to 4x were broken, indicating excessively drawn ribbons.

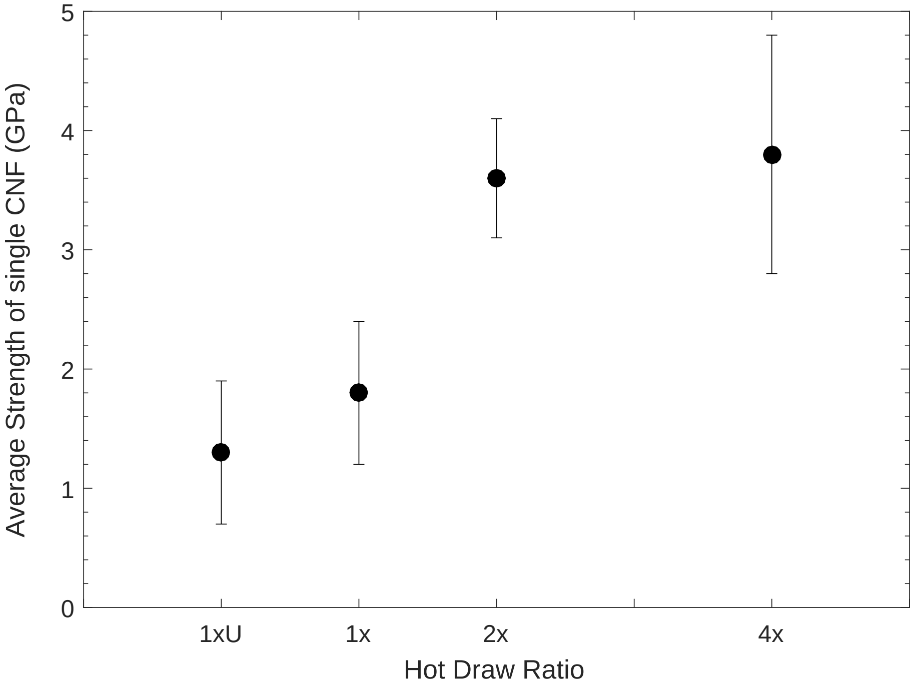

Figure 4.6: Average strength of 1xU, 1x, 2x and 4x single carbon nanofiber

It should be noted that while the modulus of the fiber is predominantly an intrinsic

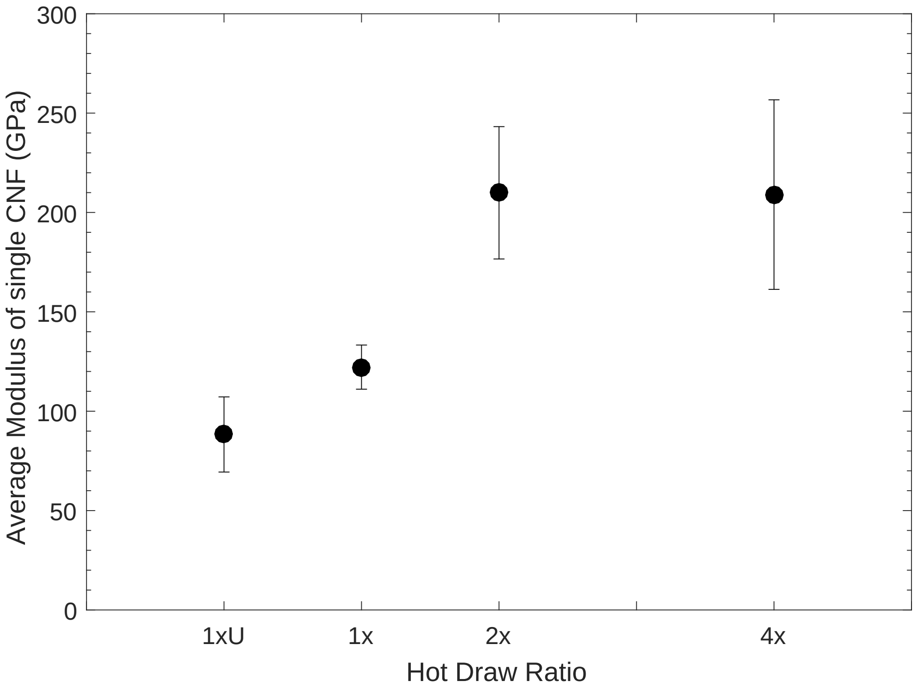

Figure 4.7: Average modulus of 1xU, 1x, 2x and 4x single carbon nanofiber

property of the material, reflecting mainly the alignment and concentration of the turbostratic domains, the strength of a nanofiber, in addition to the above microstructural features, is also governed by local defects such as surface flaws and pores in the fiber.

We studied the surface flaws of CNFs via direct SEM imaging. The SEM images of some of the 1x CNFs show the presence of pits on the surface. These flaws do not exist in as electrospun samples and become noticeable only after the heat treatment and conversion to CNFs. The origin of these flaws are not clear at this point, however, it is speculated that the generation of volatile species during thermal stabilization and carbonization increases the pressure inside the fiber, thus, surface holes will be generated through which the volatile species will leave surface pores behind as they leave the fiber. Interestingly, no such surface flaws were observed in hot-drawn nanofibers. This is likely due to higher

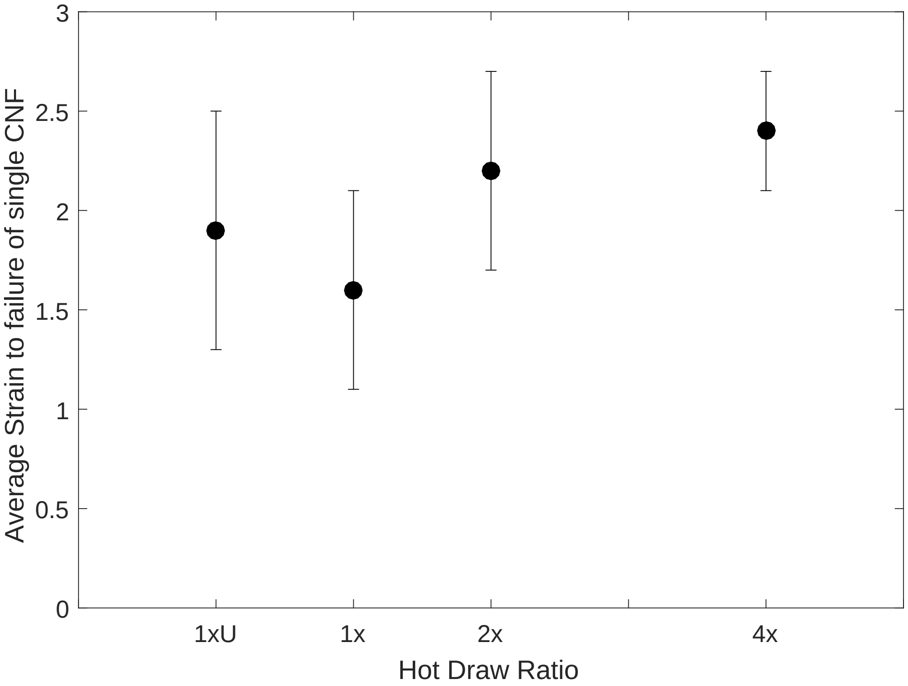

Figure 4.8: Average strain to failure of 1xU, 1x, 2x and 4x single carbon nanofiber

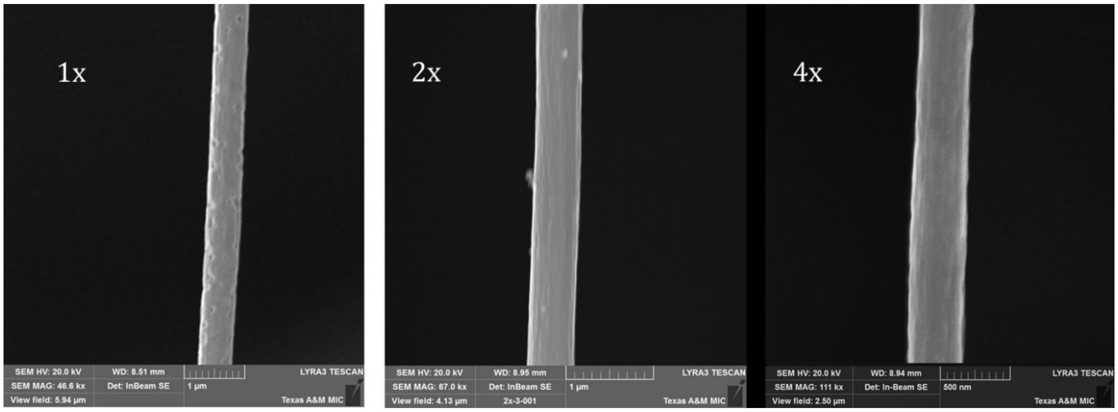

Figure 4.9: SEM image of 1x CNF with surface pores and 2x and 4x CNF with improved surface

degree of crystallinity and better packing of chains in hot-drawn fibers which enhances the interactions between chains. As a result, the volatile species may not generate enough pressure to move the chains aside and to generate surface pores with the dimensions observed in Figure 4.9, instead the volatile species may diffuse outward. On careful analysis of the strength data, it was found however that strength of the fibers does not show any correlation with the presence of the pores, suggesting that the critical flaw size which can lead to considerable reduction in strength is larger than the pore size (Figure 4.9).

4.3.2 Failure Mode of CNF

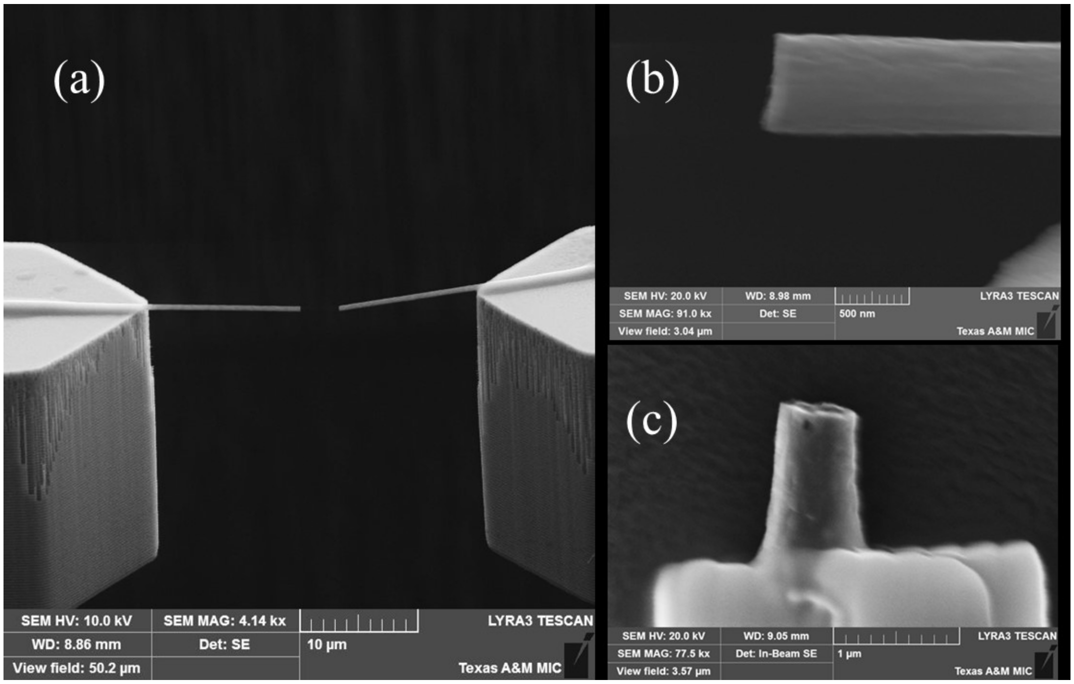

Figure 4.10: Single CNF failed in tension

Fractured CNFs were imaged in SEM to obtain more insight into fracture mechanisms as presented in Figure 4.10 (a-c). The failure of the nanofibers occurs within the gage length of the specimen. Moreover, as observed in Figure 4.10 (b-c), from previously discussed TEM images and also according to the stress-strain curves of CNFs, the failure

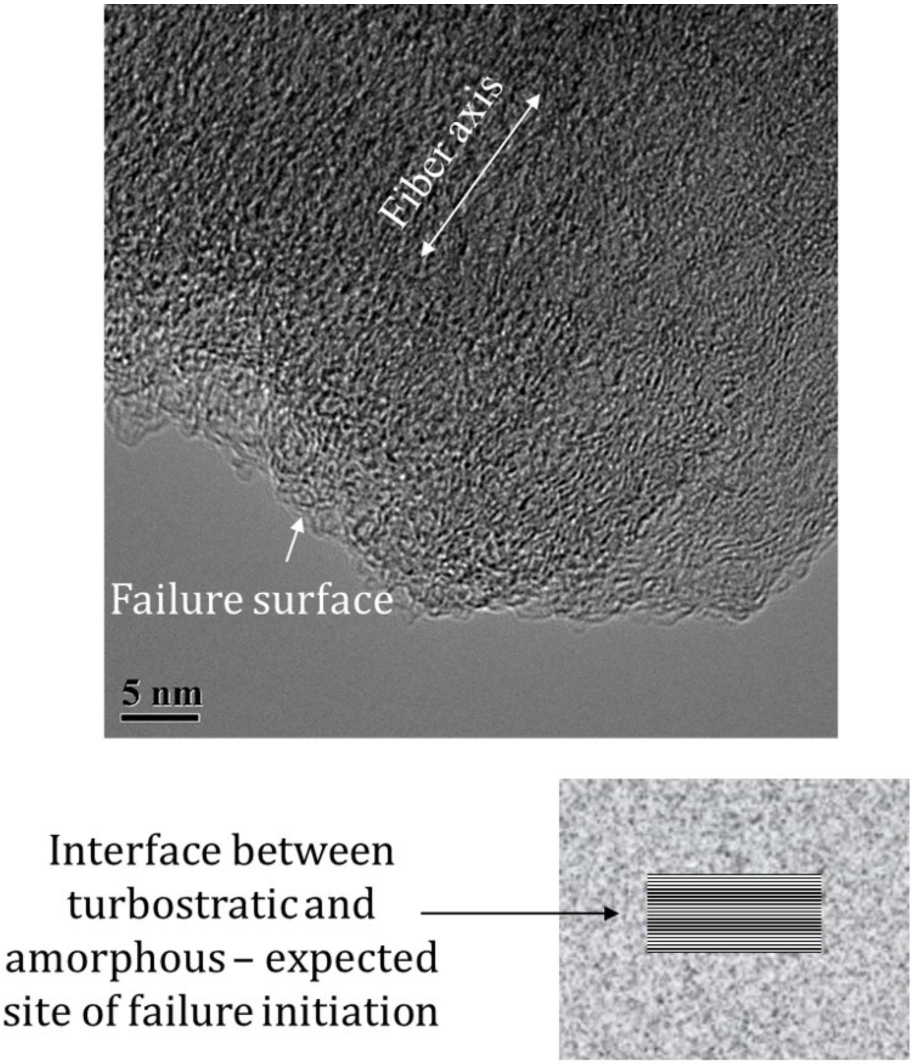

Figure 4.11: TEM image of 4x CNF indicating failure surface

appears to be brittle in nature, with the fracture surface being normal to the loading direction.

To further understand the failure mechanism of a single CNF, a CNF sample was prepared for observation in the TEM. CNFs were dissolved in ethanol and sonicated for 20 minutes in a water bath. On careful observation of the failure surface of the fiber, it appears that turbostratic domains are present along the fracture surface (Figure 4.11), suggesting that the interface of the turbostratic-amorphous regions is the location of failure, or failure has occurred by failure of turbostratic planes. However, since the in-plane strength of the turbostratic planes is higher than that of amorphous carbon, the former seems to be the main location of failure initiation.

4.4 Conclusion

In this chapter, the mechanical properties of CNF's were presented specifically the tensile strength and Young's modulus. Four cases of samples were tested 1xU, 1x, 2x and 4x. The lowest strength and modulus were achieved in the case of 1xU. This is likely due to a loss of PAN chain alignment during thermal stabilization and carbonization by entropic forces, which translates into poor turbostratic alignment in CNFs. On the other hand, the 1x nanofibers which were gripped during thermal stabilization, showed a $\approx$38% increase in modulus and 36% increase in strength of the nanofiber compared to 1xU samples. The increase in strength and modulus are both attributed to retaining PAN chain alignment which was achieved during electrospinning during subsequent thermal stabilization as a result of the applied force. The chain alignment translated into turbostratic domain alignment. The application of hot drawing to PAN and the resulting enhancement in PAN chain alignment was also demonstrated to lead to turbostratic domain alignment in CNFs and a considerable increase in both strength and modulus. It was such that hot-drawing the precursors to a draw ratio of 2 (2x) led to $\approx$170% and $\approx$137% increase in strength and modulus of the CNFs compared to the 1xU samples. Morever, further drawing the precursors to 4x did not demonstrate a considerable change in chain alignment and thus strength and modulus. The highest value of modulus obtained was 287GPa and highest tensile strength was 5.4GPa. It is important to note that the strength of the nanofiber obtained is the highest reported to date of carbon nanofibers fabricated from pure PAN homopolymer.

The surface morphology of the CNFs was also a function of the hot-drawing. While the 1x nanofiber surface showed a large number of pits and undulations on the surface, the hot drawn CNFs appeared to be smoother on the surface. The pits are likely the gateways of volatile species generated in the fiber during thermal stabilization and carbonization to the environment. This change in surface morphology can be attributed to the improved packing of chains in the hot drawn nanofibers, which resists the pressure built up by the volatile species and their sudden escape during heat treatment and the scission of chains.

Failure surfaces showed failure to occur in a direction perpendicular to the loading direction (brittle failure) and appears to have initiated and propagates along the short-side interface of the turbostratic and amorphous regions.

The next chapter discusses failure modes of the above mentioned nanofibers with the help of a simplistic representative model using ABAQUS. The relation between the strength and modulus of the nanofiber will be discussed as well as the effect of orientation on the von Mises stress in the fiber. The minimum proximity of turbostratic domains in the nanofiber to create local stress fields will also be discussed.

5. FINITE ELEMENT MODELING OF MECHANICAL BEHAVIOR OF SINGLE CARBON NANOFIBER

5.1 Introduction

Through the experimental work discussed in the preceding chapters, we have demonstrated that hot drawing of PAN nanofiber precursors has a substantial influence on the morphology, mechanical strength and modulus of subsequently formed carbon nanofibers. With the use of XRD, Raman and TEM microscopies, it has been shown that hot drawing of nanofibers leads to improvement in alignment of the turbostratic domains in the direction of fiber axis. On careful correlation of the results obtained from tensile tests of single nanofibers with the spectroscopy data, the improvement in strength and Young's modulus is attributed to the improvement in the orientation and alignment of these domains.

A rather simplified but effective continuum model, which relates the mechanical properties of CNFs to their microstructure, treats individual CNFs as a composite fiber composed of a matrix of amorphous carbon reinforced with anisotropic turbostratic domains [63]. The elastic modulus of turbostratic domains (especially the modulus along their basal planes) is significantly higher than amorphous carbon. Thus, it is intuitive to observe an improvement in the modulus of CNF obtained from hot drawing of the precursor nanofiber with alignment of these domains. In our research, we have also observed a significant enhancement in tensile strength of the CNFs. Strength of the nanofiber is an intrinsic property and is dependent on a number of factors like development of stress concentrations, morphology of the nanofiber surface, stress mismatch at the interface between particles of different stiffness. In order to explain the improvement in properties obtained and to identify the critical microstructural parameters influencing the mechanics of CNFs, a computational model has been developed. This model can be considered representative of CNFs, used predominantly for qualitative analysis to understand the effect of particle orientation, proximity of particles with respect to each other and buildup of local stresses and stress concentrations in the nanofiber.

5.2 Model Development

The TEM image of a CNF is shown in Figure 5.1. Turbostratic domains are marked with rectangles, bordering the domain. These domains/rectangular representations are observed through the entire cross section of the nanofiber. In order to model such a fiber with turbostratic domains embedded in an amorphous matrix, a portion of single CNF was modeled as a square object with dimensions of 20nm × 20nm.

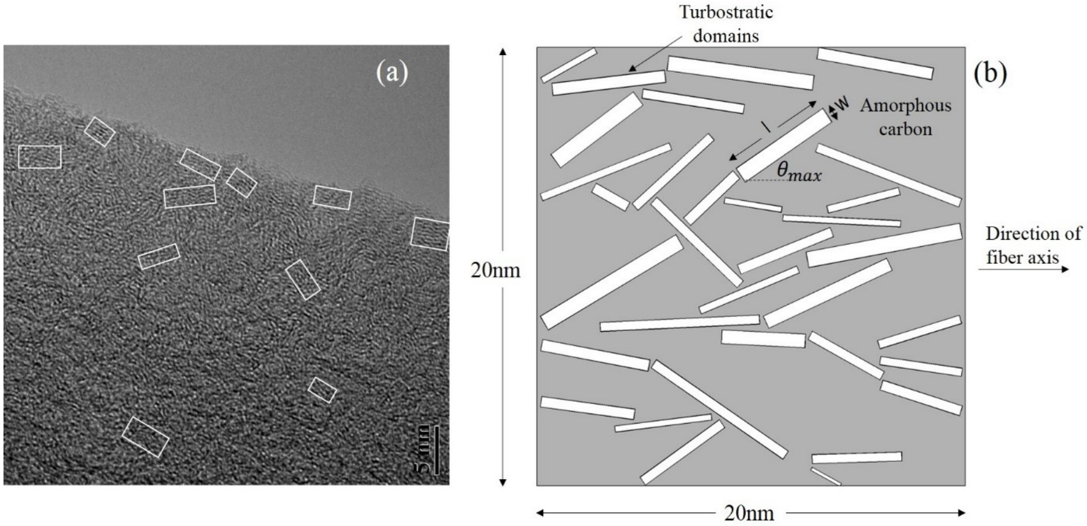

Figure 5.1: Schematic of model of carbon nanofiber

A 2D representative volume element of CNFs composed of turbostratic particles within an amorphous carbon matrix was generated and the locations of the particles were randomly selected. The particles were grown anisotropically with growth rates in two normal directions (one representing the basal plane of the turbostratic domains, which is the longer direction of the domains and the other normal to that) were selected, such that the average aspect ratio of the particles will represent the typical aspect ratio of the turbostratic domains observed in TEM images. Particle growth was in steps, and in general it was continued until the desired volume fraction of the particles (v_f), determined from TEM images, was reached. Inter-penetration of particles was avoided by modifying the growth rates of particles which have grown to contact. The angle of long-axis of particles with the fiber axis was selected to be a random value between zero and θ_{max}. A value of $\theta_{max} = 90^\circ$ and 0° correspond to entirely randomly and highly aligned turbostratic domains with respect to fiber axis. More details of the model can be found in [158].

The effect of hot drawing of PAN precursors can be replicated in this continuum model by modifying the alignment of turbostratic domains and the value of θ_{max}. In the model, volume fraction of approximately 20%±1% was maintained and the turbostratic particles were assigned an aspect ratio of 10:1 in the length:width dimension. Correlating with turbostratic particles in the TEM image, the length of the rectangle is the in-plane length of the graphene sheets in the particles, i.e. L_a and the width is the out-of-plane dimension of the particles L_c, as seen in Figure 5.2. Using these input parameters, the rectangular particles were of varying sizes were dispersed throughout the 20nm × 20nm model.

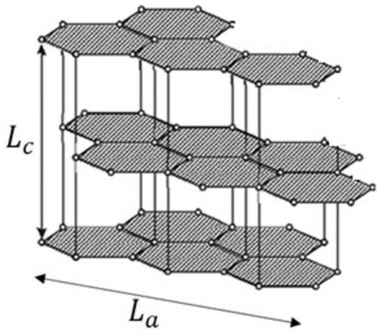

Figure 5.2: Schematic of turbostratic domain showing L_c and L_a

5.2.1 Material Properties

The two phases in the model are assigned different material properties, that of turbostratic carbon and amorphous carbon. Amorphous carbon is assumed to be isotropic. On the contrary, turbostratic carbon is transversely isotropic in nature, with the properties in directions 1 and 3 being same (the basal plane), and the direction 2 being the out-of-plane direction. Figure 5.3 shows the schematic of a turbostratic particle, depicting the directions of planes.

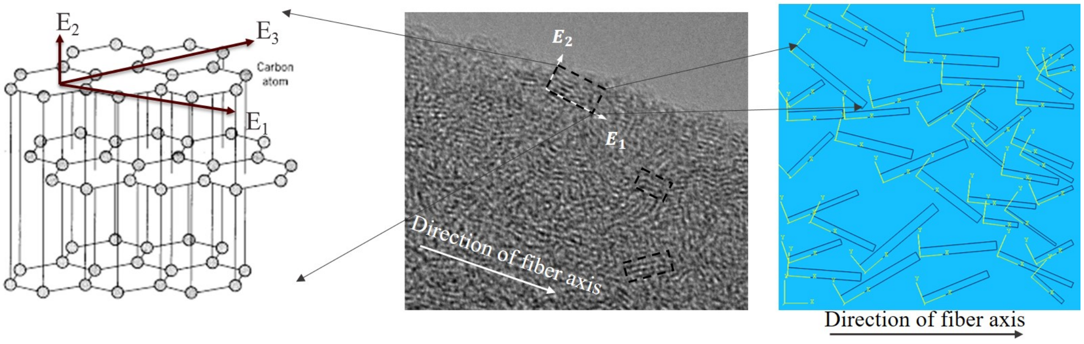

Figure 5.3: Schematic of turbostratic carbon depicting the 1, 2 and 3 directions

The properties used for the particles in ABAQUS are in Table 5.1.

Property	**Value**
$E_{1A} = E_{2A} = E_{3A}(GPa)$ [159]	140
$\nu_{12} = \nu_{23} = \nu_{13}$	0.3
E_{1TB} (GPa)	700
E_{2TB} (GPa) [160]	39.5
E_{3TB} (GPa)	700
$\nu_{12TB} = \nu_{32TB}$[160]	0.006
ν_{13TB}[160]	0.195
$\nu_{23TB} = \nu_{21TB}$	0.000339
G_{12TB} (GPa) [160]	4.6
G_{13TB} (GPa)	292.8
G_{23TB} (GPa)	4.6

Table 5.1: Material properties of amorphous carbon (A) and turbostratic carbon (TB) used in ABAQUS

The values of E_{1TB} and E_{3TB} are obtained from modulus of commercially available carbon fibers (T300). On account of the low carbonization temperatures of 1100°C, turbostratic carbon is in the form of misaligned graphitic planes making it inappropriate to use the in-plane modulus of graphite for our case of CNF. The skin of commercially available carbon fibers possess structure similar to that of the observed turbostratic domains, as discussed in Chapter 1. Thus, we took the in plane modulus of turbostratic domains to be the same as the modulus of carbon fibers. The values of $E_{2TB}, \nu_{12TB}, \nu_{13TB}$ are obtained from literature for graphite [160]. The shear modulus of the turbostratic domains G_{12TB} is also taken from literature for graphite [160]. As turbostratic particles are of the form of pyrolytic carbon with misaligned graphene sheets, the shear modulus of these were assumed to be the highest that has been observed in literature for graphite. Poisson's ratio ν_{21TB} and shear modulus G_{13TB} were calculated using Equation 5.1 and 5.2 respectively.

$$\frac{\nu_{12}}{E_1} = \frac{\nu_{21}}{E_2} \tag{5.1}$$

$$G_{13} = \frac{E_1}{2(1+\nu_{13})} \tag{5.2}$$

5.2.2 Boundary Conditions

The carbon nanofiber model represents tensile test performed on the nanofiber. To replicate the boundary conditions used in the test, nodes on the left boundary were assigned translational and rotational boundary conditions, i.e. $U_1 = UR_2 = UR_3 = 0$. To accommodate for contractions due to Poisson's effect, the node on the top left corner was given boundary condition of $U_2 = 0$, providing fixed boundary condition at this node, leaving the other nodes free to move in the U_2 direction. The boundary on the right edge is applied displacement boundary condition of 0.5nm, resulting in a strain of 2.5%. These boundary conditions are seen in Figure 5.4.

The boundary conditions applied to the model replicate those on the single CNF during the experimental tensile test performed using the MEMS device as discussed in Chapter 4. In each increment of strain, the total force applied to the fiber was calculated as the sum of the nodal forces, and the axial stress was calculated by normalizing the axial force with the fiber cross section area (with unit out of plane thickness). Moreover, in each step of loading the von Mises equivalent stress was calculated, and was used to make predictions about the onset of failure and the axial strength of the fiber.

5.2.3 Failure Criteria

In a real CNF, the failure can happen in the amorphous phase, in the turbostratic domain or at the interface between them, depending on the orientation, size, proximity and defect density within each region. However, in general, it is accepted that the turbostratic

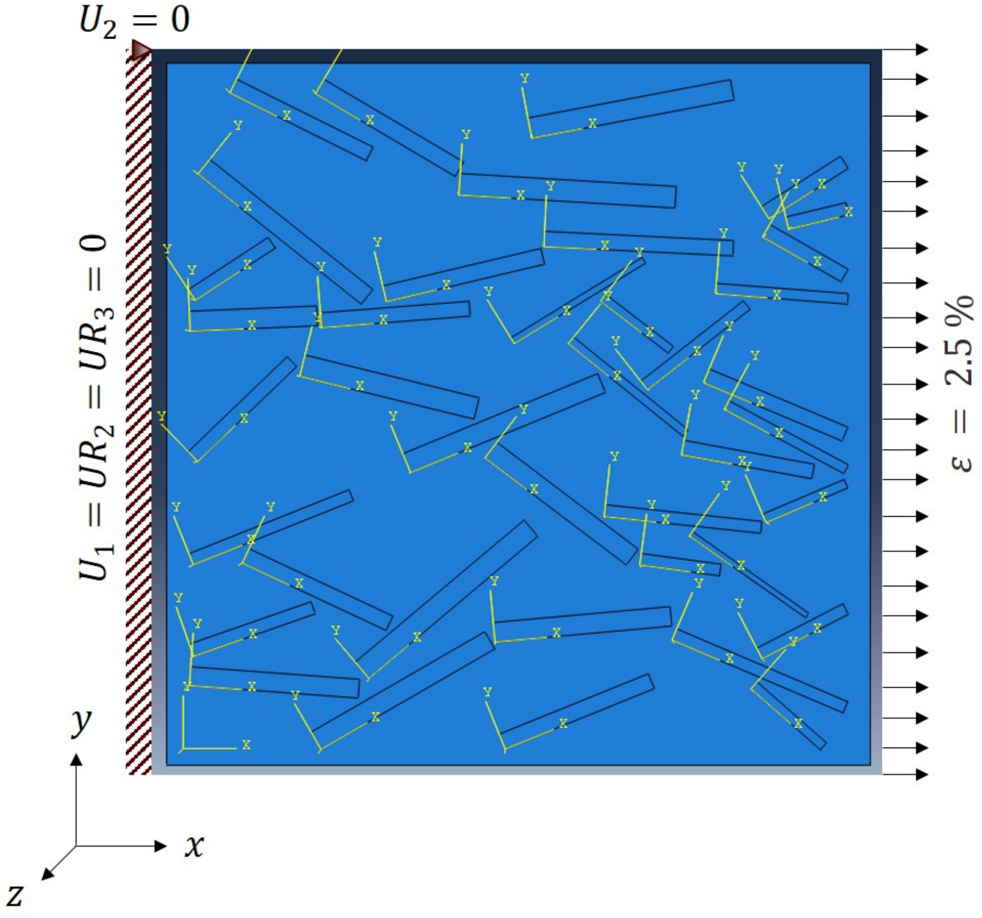

Figure 5.4: Boundary conditions applied to model of single CNF in ABAQUS

domains have higher strength and stiffness compared to amorphous phase due to more ordered structure of carbon atoms in the former which will enhance the C−C interactions. Therefore, in this study, we have assumed that the failure will initiate in the weaker phase, i.e., the amorphous phase. Moreover, we assumed that the failure will be initiated when the von Mises stress reaches a critical value. Given the considerable elastic mismatch between the amorphous and crystalline phase (turbostratic domains), strong biaxial stress states are expected to develop near the interfaces between the two, and that is a likely location for failure initiation.

5.2.4 Mesh Convergence

As the first step to obtain model predictions of the stress-strain relationships of the fibers, a mesh sensitivity analysis was carried out. To this end, four seed sizes on the

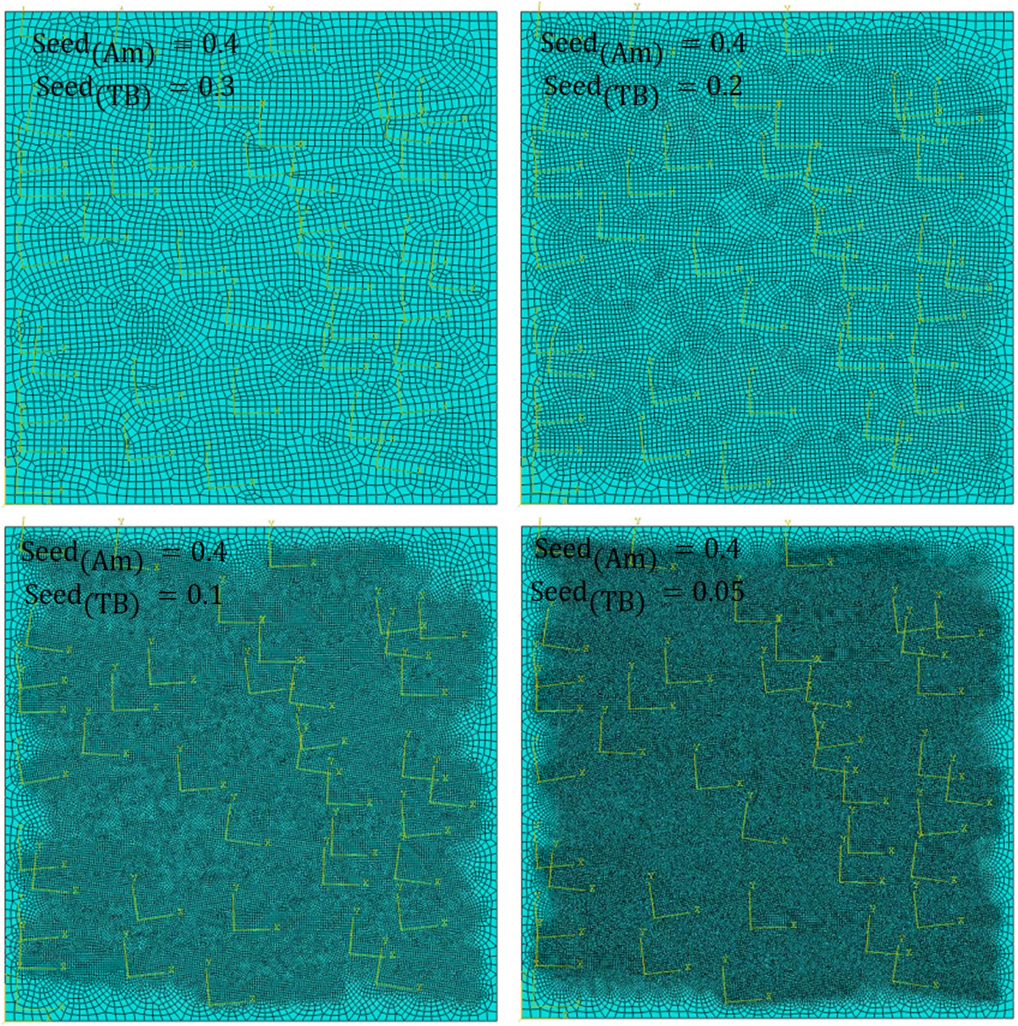

Figure 5.5: (a-d) show the seed size used to mesh the model of single CNF

turbostratic domains/particles were tested. The rectangles (turbostratic particles) are embedded in an amorphous matrix and the seed size of this amorphous boundary was fixed at 0.4nm, whereas the seed size of the outer boundary of turbostratic domains was varied from 0.4nm to 0.05nm. Mesh using four cases of seed sizes is shown in Figure 5.5. Analysis of the stresses in all cases was carried out and the maximum von Mises stress in the amorphous region, as an effective stress, in each case is plotted in Figure 5.6.

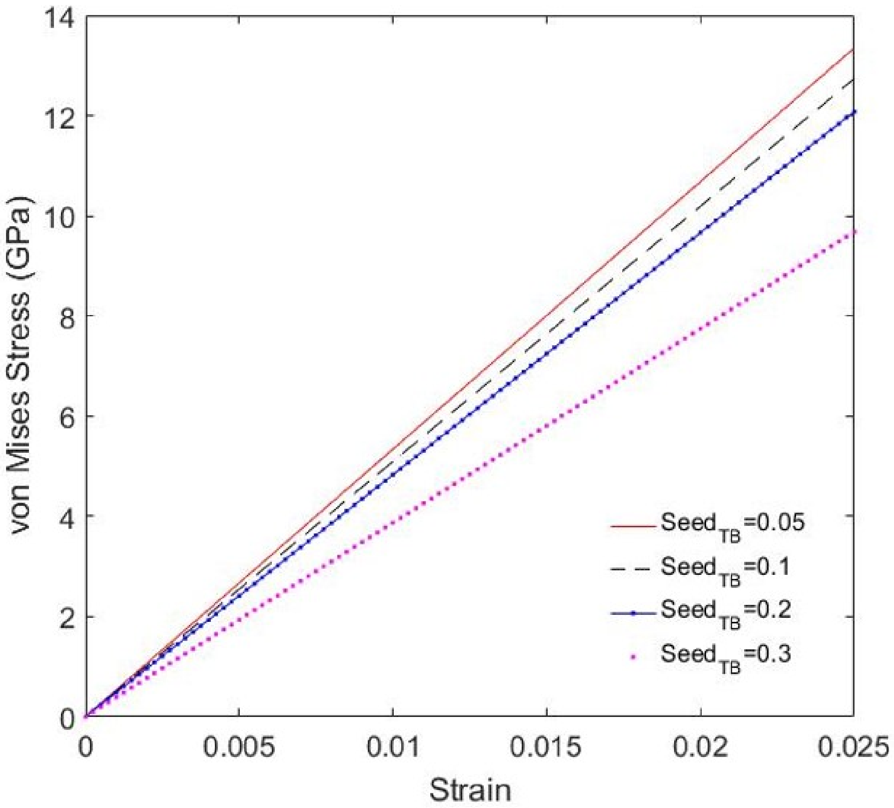

Figure 5.6: Maximum von Mises stress in the amorphous region in the CNF model plotted with respect to strain, for various seed sizes

As shown in Figure 5.6, reducing the seed size from 0.3nm to 0.2nm (increasing the number of elements by 111.3%) leads to ≈25% change in the calculated value of the maximum von Mises stress. However, further reducing the seed size from 0.2nm to 0.1nm results in significantly lower changes in the Von Misses stress (≈5.5%), suggesting mesh convergence. For the case of seed size 0.05nm, there was 4.6% error in the maximum von Mises stress as compared to seed size 0.1nm. The analysis time for the case of 0.1nm seed size was significantly lower, and hence seed size of 0.1nm was selected as the seed size for turbostratic particles and 0.4nm for amorphous boundary, resulting in 41,556 plane stress quadrilateral quadratic elements for subsequent analyses.

5.2.5 Effect of Orientation of Turbostratic Particles on Mechanical Properties of CNFs

With the optimum mesh size and properties determined, a study was carried out on the effect of orientation of the turbostratic particles on the local von Mises stress observed in the fiber, as well as on the tensile stress S_{11} in the fiber. The orientation of turbostratic particles was random, limited by the maximum possible orientation of the particles, θ_{max}, as an input parameter.

Discussions in Chapters 2, 3, 4 have shown that the orientation and alignment of turbostratic domains in the fiber increase with hot drawing ratio, which leads to improvement of mechanical modulus of the fiber. To understand the evolution of local stresses and failure initiation in the fiber, four cases of maximum angle of turbostratic domains were selected: $\theta_{max} = 90°, 45°, 30°, 10°$. While it is not trivial to directly relate these values to experimental cases of alignment, it is to be noted that the reduction in θ_{max} represents an improvement in particle alignment, as it was comparatively observed between the cases of 1xU, 1x, 2x and 4x fibers in previous chapters. The effect of orientation on the stresses in the fiber, distance between particles and local stress evolution have been studied using this model. Given the randomness in the particle alignment and location of the model, for each case of particle volume fraction, particle aspect ratio (a_r) and θ_{max}, five independent representative volume elements of CNFs were generated, and the average values of stress and strain in each case were reported.

The average tensile stress of the CNF, σ_{11} (also referred to as S_{11}), at each increment of strain was calculated using Equation 5.3,

$$\sigma_{11} = \frac{1}{n}\sum_{i=1}^{n} RF_i \tag{5.3}$$

where RF_i is the reaction force on node i on the right vertical boundary (Figure 5.4) and n is the total number of nodes.

5.3 Results and Discussion

To predict the dependence of CNF strength on particle alignment and aspect ratio, the following procedure was employed. For each microstructural representation of CNFs corresponding to a specific volume fraction of particles, average particle aspect ratio and θ_{max}, the stress distribution, average axial stress (σ_{11}) and the maximum von Mises stress in the amorphous phase (VMS_{max}) were calculated from the model as a function of applied average axial strain. Since the model only considers elastic properties of the constituents, in the limit of small deformations, the two stress parameters (average axial and maximum von Mises stress) should scale linearly with strain. Therefore, the ratio of the two stress measures, as defined in Equation 5.4, should be independent of tensile strain.

$$\alpha = \frac{VMS_{max}}{\sigma_{11}} \tag{5.4}$$

Moreover, as stated earlier in this chapter (Section 5.2.3), the failure is assumed to occur in the amorphous phase when the maximum von Mises stress reaches a critical value, i.e., when $VMS_{max} = VMS_{critical}$. Thus, the axial strength of the CNF model can be expressed as $\sigma_{11} = \dfrac{VMS_{critical}}{\alpha}$. Hence, assuming that the value of $VMS_{critical}$ is a property of the amorphous phase and not dependent on orientation of the particles, the parameter α will be a measure of fiber strength (inversely correlated with that). Therefore,

α was calculated for cases with different average particle aspect ratio and θ_{max} to make predictions about the dependence of fiber strength on these parameters. It is to be noted that this comparative analysis is qualitative, and does not provide us with the value of axial stress unless the value for $VMS_{critical}$ is assumed.

5.3.1 Overall Stress Distribution as a Function of θ_{max}

Distribution of von Mises stress across the CNF is shown in Figures 5.8 - 5.11 for cases of $\theta_{max} = 90°, 45°, 30°, 10°$.

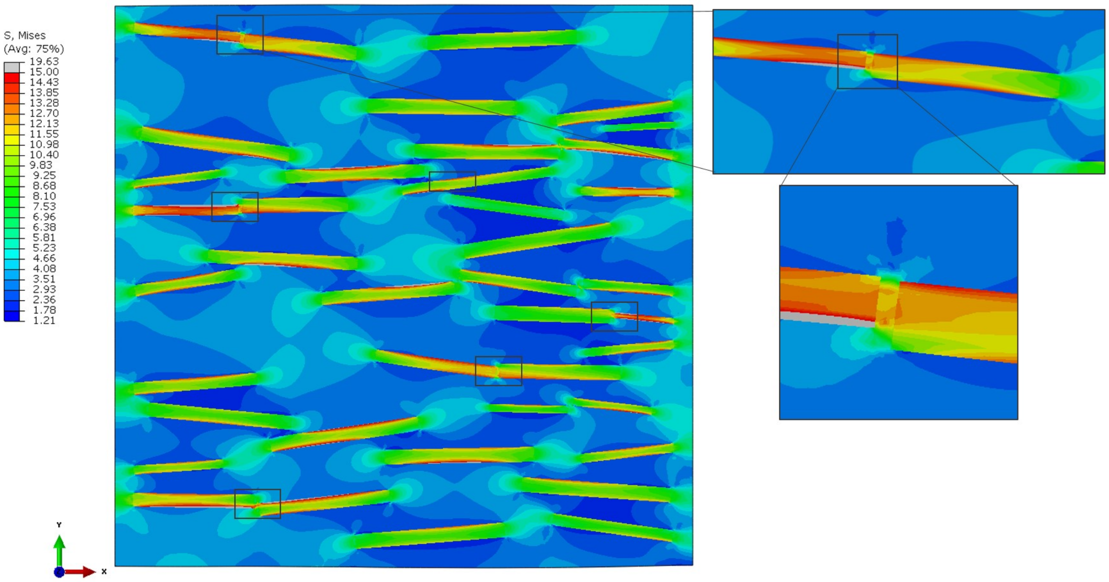

Figure 5.7: Distribution of von Mises stress seen in turbostratic particles and amorphous domain obtained from ABAQUS

As seen in Figure 5.7, the stresses experienced by the turbostratic particles in the model are higher as compared to those in the amorphous regions due to higher modulus of the domains. From Figure 5.7, a few pertinent observations can be made which applies to all cases of particle orientation:

- Von Mises stress in the amorphous regions near the particle ends are higher than those in the regions along the particle. That is likely because the stiffer than matrix particles will prevent lateral shrinkage of the matrix, leading to higher stress biaxiality,
- In most cases, local stress concentrations observed on one particle do not affect the stresses seen on another particle, unless the distance between two adjacent particles is less than $\approx$0.2nm.

The maximum von Mises stress in the amorphous region of the CNF extracted from ABAQUS as a function of strain for different values of θ_{max} is plotted in Figure 5.12. For each θ_{max} five different randomly generated microstructure was studied all corresponding to the same values of average particle aspect ratio and volume fraction. The von Mises stress in all cases varies linearly with strain, as expected due to the fact that FEA only considers linear elastic material behavior and small deformations. A fair amount of scatter in the data for each value of θ_{max} is observed, such that no clear trend in the von Mises stress can be realized. This is not surprising since the local stress components is highly dependent on the distance between particles, particle size and aspect ratio, the angle between neighboring particles, and orientation of individual particles while these parameters do not have identical distributions among different realizations of a microstructure. That is partly due to size of the representative volume element which was selected with the consideration of computational costs.

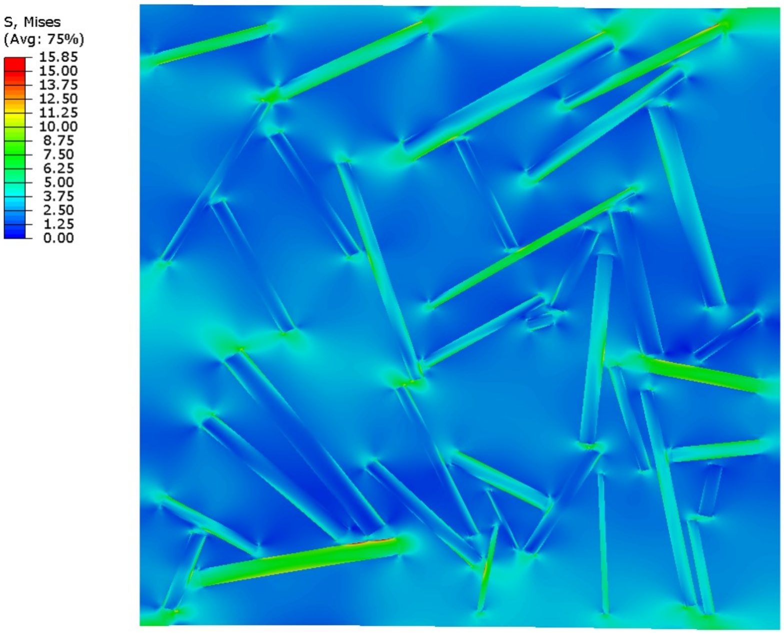

Figure 5.8: Distribution of von Mises stress in the model of a single CNF using ABAQUS for orientation $\theta_{max} = 90°$

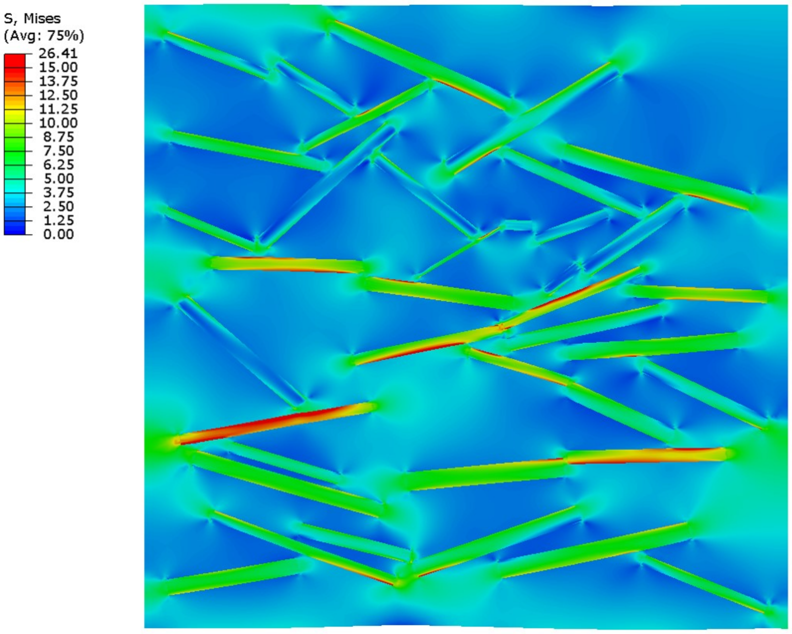

Figure 5.9: Distribution of von Mises stress in the model of a single CNF using ABAQUS for orientation $\theta_{max} = 45°$

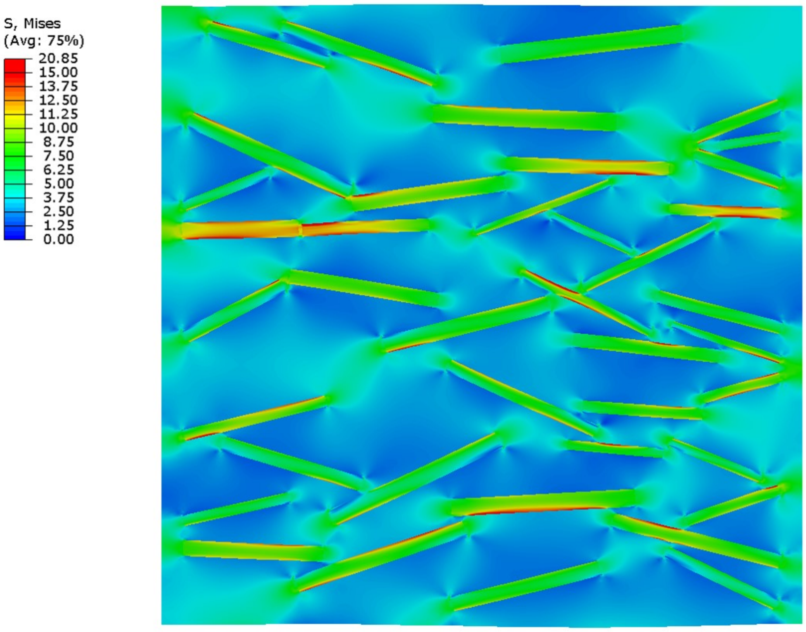

Figure 5.10: Distribution of von Mises stress in the model of a single CNF using ABAQUS for orientation $\theta_{max} = 30°$

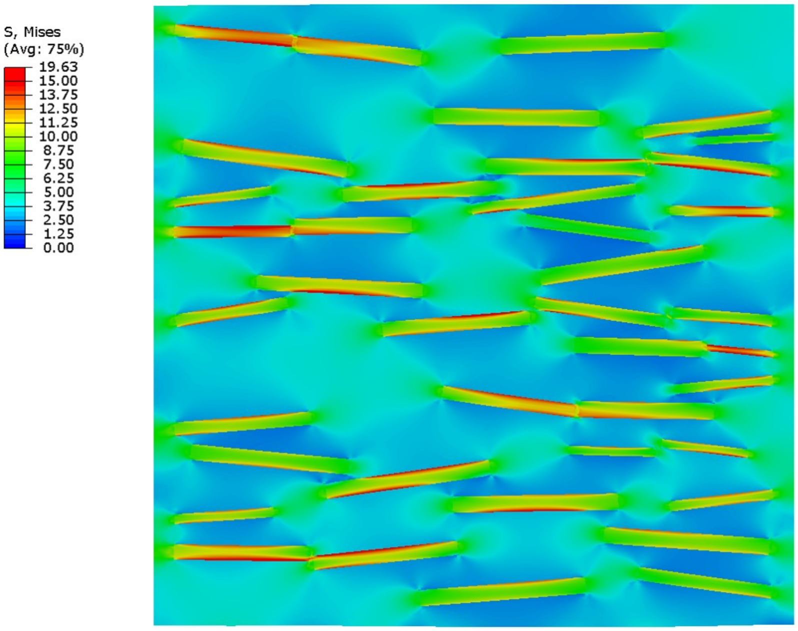

Figure 5.11: Distribution of von Mises stress in the model of a single CNF using ABAQUS for orientation $\theta_{max} = 10°$

It is to be emphasized here that in our model, the input parameters were the volume fraction (v_f) and the aspect ratio (a_r) of the particles, and maximum angle of orientation θ_{max}. The reason for the selection of the above mentioned input parameters is rooted in our ability to control the microstructure of CNFs in the experiments and observation of TEM images. That is, the volume fraction (v_f) and the aspect ratio (a_r) of the particles is governed by the temperature of carbonization and molecular orientation of precursor fiber. The orientation of the particles θ_{max} in the fiber is determined by the molecular orientation of precursor fiber obtained during fabrication (electrospinning), hot drawing ratio and tension applied during heat treatment. The other factors such as proximity of particles to each other, relative orientation etc. were not controlled in our experiments and hence have been randomly assigned in the model.

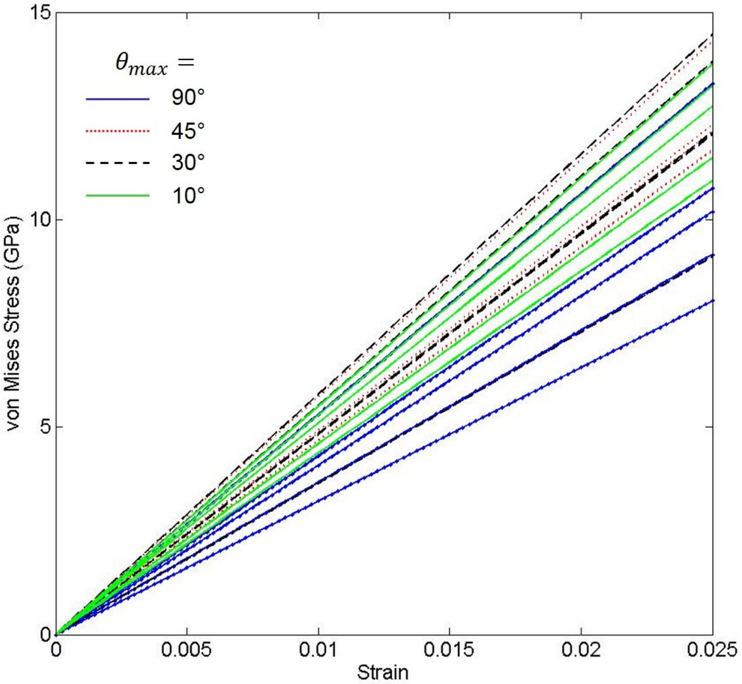

Figure 5.12: Max von Mises stress in amorphous region plotted with respect to strain for cases of $\theta_{max} = 90°, 45°, 30°, 10°$

In order to understand qualitatively the effect of orientation of particles on the overall strength and modulus of the CNF, average tensile stress obtained from ABAQUS at each strain increment was plotted for all cases of θ_{max} (Figure 5.13)

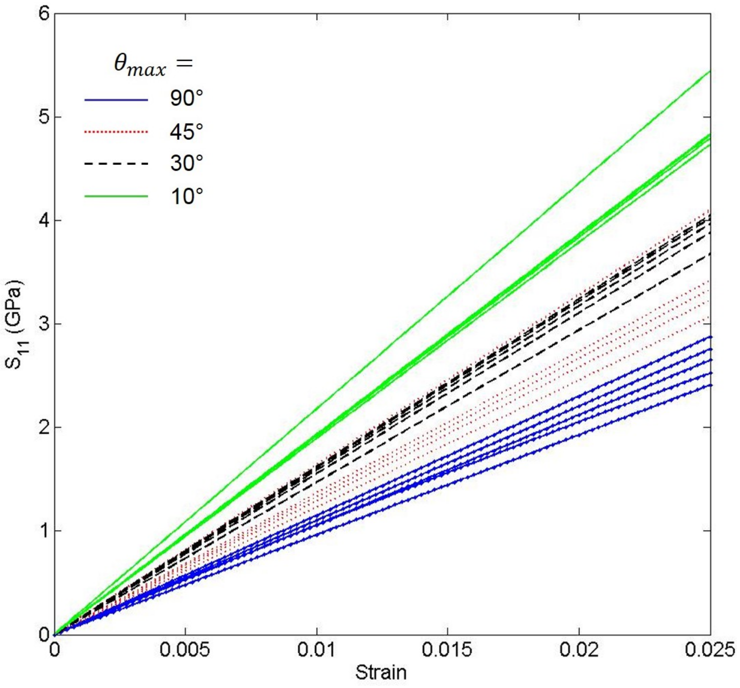

Figure 5.13: Tensile strength plotted with respect to strain for cases of $\theta_{max} = 90°, 45°, 30°, 10°$

5.3.2 Variation of Elastic Modulus with Particle Alignment

The elastic modulus, calculated directly from Figure 5.13, using the linear relation between stress and strain showed an increase in the modulus with increase in particle alignment. This data, calculated from the model is compared to the modulus of the single CNF obtained from experiments in Table 5.2.

As expected, the modulus of the nanofibers increases with the increase in alignment of the particles, i.e with more particles providing in-plane stiffness component in the direction

θ_{max}	**Estimated Modulus from ABAQUS (GPa)**
90°	105.8 ± 7.1
45°	137.2 ± 15.8
30°	156.8 ± 6.1
10°	197 ± 11.9

Table 5.2: Average values of strength and modulus of 1xU, 1x, 2x and 4x single carbon nanofibers

of fiber axis. It is however to be pointed out that with hot drawing, along with increase in alignment, an increase in the particle size has also been observed experimentally. As this factor is not taken into account in the model it is not surprising that the model under predicts the modulus of the nanofiber. Moreover, in the experiments, a big jump in the modulus of 2x fibers was observed as compared to the case of the 1x, and beyond this hot draw ratio, limited improvements were observed in the modulus. This is likely due to accumulation of damage in the PAN nanofibers (such as chain scisson) at draw ratios above 2x which leads to defects in CNFs. The accumulation of defects are not taken into consideration in the model.

5.3.3 Variation of Axial Strength on Particle Alignment

As stated earlier in this section, the ratio of the maximum von Mises stress to average axial stress, α, is considered to be a measure of strength in the material such that microstructural representations of CNFs with higher values of α will distribute stresses less uniformly, thus will have lower strength. We calculated the value of α for different values of θ_{max} and several realization of each θ_{max}, as presented in Table 5.3 and Figure 5.14.

From the models of microstructures with different particle orientation, we observed that the ratio increases with an increase in the misalignment of the turbostratic particles,

θ_{max}	α
$90°$	3.88 ± 0.52
$45°$	3.63 ± 0.11
$30°$	3.15 ± 0.52
$10°$	2.52 ± 0.16

Table 5.3: Value of α with θ_{max}

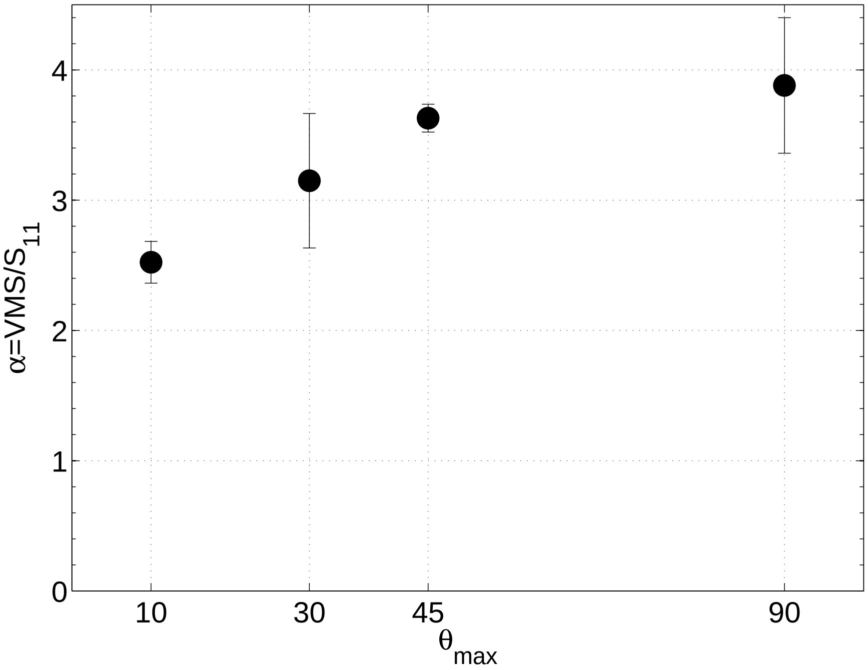

Figure 5.14: Change in α with increase in misalignment of turbostratic particles

i.e with increase in θ_{max}. Hence,

$$\alpha_{\theta(90°)} > \alpha_{\theta(45°)} > \alpha_{\theta(30°)} > \alpha_{\theta(10°)} \tag{5.5}$$

Thus, assuming the critical von Mises stress at which failure will be started is independent of particle alignment, we will have:

$$\sigma_{11(90^{\circ})} < \sigma_{11(45^{\circ})} < \sigma_{11(30^{\circ})} < \sigma_{11(10^{\circ})} \tag{5.6}$$

The value of α obtained from ABAQUS results is seen in Figure 5.14.

Although no direct comparisons can be made between the model and experiment in terms of turbostratic domain alignment, the trends observed in the model has striking similarities (although more qualitatively) with the experimental results presented in Chapter 4. For instance, according to the modeling work, the strength of the CNFs initially increases as the θ_{max} is reduced from 90° (randomly oriented particles) to 45° (partial alignment), while in the experiments, we observed an increase in strength with enhanced particle alignment from 1.3 ± 0.6 (1xU) to 3.8 ± 1.0 (2x) samples. On the other hand, further enhancement in alignment did not lead to further increase in strength in either the model or the experiments.

However, quantitatively, the model is under-predicting the effect of particle alignment on CNF strength as it was measured from the experiments. For instance, from the model, the maximum improvement in the strength compared to the case of CNFs with randomly oriented particles was 56% $(\frac{\alpha_{90^{\circ}}}{\alpha_{10^{\circ}}} - 1)$. On the other hand, in the experiment, we observed more than 192$\%$ improvement in strength (strength of 4x over 1xU).

This quantitative discrepancy can be attributed to several parameters. For instance, the material properties of constituents used are obtained from literature for similar material systems and no direct measurement of their properties can be made. More importantly, with an increase in hot drawing ratio, there is an increase in crystallinity of the PAN nanofiber which may lead to improvement in the mechanical properties of the turbostratic domains created on carbonization. In contrast, in the model used, these properties remain constant with change in orientation. Another factor not included in the model is that the aspect ratio of the turbostratic domains in the model is assumed to remain constant even though it is observed with TEM and through literature that through the process of hot drawing, the turbostratic domains increase in size as chains can get packed more readily. Despite the use of this simplistic model, qualitative analyses of the failure of carbon nanofibers have been possible.

5.4 Conclusion

This chapter has discussed development of a simplified 2D continuum model in order to shed light on the relations between mechanical properties of CNFs and their microstructure. In the model, we assumed that the failure of the CNFs is initiated in the amorphous phase where the von Mises stress exceeds a critical value. By proper normalization of stress parameters, we managed to related strength to particle alignment without making any assumptions about the value of the critical von Mises stress. The model showed that if the failure strength of amorphous carbon is assumed to remain the same in the cases of different orientations of turbostratic domains, the tensile strength of the carbon nanofiber will increase with an enhancement in particle alignment. With an improvement in alignment of the particles, the spacing between adjacent particles increases which reduces the stress concentrations between the particles, giving rise to higher failure strength of the fiber. On the contrary, in the case of misaligned particles, the lateral stress in the fibers is higher at a given strain, giving rise to higher von Mises stress in the amorphous region of fibers with greater θ_{max}.

As turbostratic particles have higher failure strength in the direction of their planes, it is intuitive that increase in the alignment of these particles will give rise to increase in the Young's modulus of the carbon nanofiber. Experimental results pointing to the same conclusion have been discussed in Chapter 4.

Experimentally, it is cumbersome and expensive to carry out tensile tests using in-situ TEM in which the failure initiation of the nanofibers can be visually observed. The aim of the model used in this work was to provide an insight into the effect of different particle-amorphous configurations (v_f, a_r, θ_{max}) on the development of stresses and stress concentrations to guide the experiments. The next chapter will discuss the conclusions of this research work and present some directions for future work in order to produce carbon nanofibers with further improved mechanical properties.

6. SUMMARY AND FUTURE DIRECTIONS

6.1 Summary

The goal of the presented work was to study the processing-microstructure-mechanics relationships in carbon nanofibers with an emphasis on controlling the graphitic alignment and radial homogeneity in them.

The nanofibers used in this study were fabricated using homopolymer Polyacrylonitrile (PAN) dissolved in a solution of dimethylformamide (DMF). This solution was electrospun using a setup designed and fabricated in house to obtain polymer nanofibers. The nanofibers obtained had diameters below 1μm with millions of fibers together in the form of a ribbon. A number of factors played a role in the formation of nanofibers used in this study. While voltage applied, distance between collector and infusion rate defined the formation of beadless fibers and fibers with a smooth surface, the speed of rotation of the collector disc was altered to obtain desired molecular orientation in the fibers. Chapter 2 discusses the electrospinning technique used in detail for the formation of the nanofibers. Fourier Transform Infrared Spectroscopy (FTIR) was used to determine the level of molecular orientation in the nanofiber ribbon obtained during electrospinning. Herman's orientation factor f was used to quantify the orientation of the molecular chains in the nanofiber. Limited amount of orientation was attained through electrospinning due to fast solvent evaporation in this method which lowers chain mobility. In order to achieve additional orientation of the molecules, the nanofiber ribbon was subjected to hot drawing in which the nanofibers were placed vertically in an oven and drawn using a weight that was applied at one end of the ribbon. The hot drawing process was carried out at temperature above the Tg of PAN (95°C) at 135°C. Using this method, stretch ratios of 2x and 4x were achieved for the ribbons. The molecular orientation of the PAN nanofiber ribbons were measured using FTIR and X-Ray diffraction (XRD) techniques. Herman's orientation factor (f) using this technique increased to 0.4, and PAN crystals were formed.

After confirming that the proposition of increased molecular orientation and crystallinity of polymer nanofibers via the hot drawing process proved successful, in Chapter 3 heat treatment of the polymer nanofibers to convert them into carbon nanofibers. In this chapter, the process of stabilization of nanofibers was discussed. The stabilization process creates a ladder-like structure of PAN, preparing the nanofiber for conversion to its carbon form. Stabilization is carried out between temperatures of 200°C-300°C in an oxidizing atmosphere. Chapter 3 explains the role of time and temperature on the stabilization process, and the effect of hot drawing of the nanofibers, i.e. the effect of crystallinity of the nanofibers on the cyclization of the polymer chains. Digital Scanning Calorimeter (DSC) was used to calculate the temperature of decomposition, and FTIR was used for the analysis of amount of cyclization (referred to as RCI) of the nanofibers. The reference sample '1x' and hot drawn samples '2x' and '4x' that were stabilized to an RCI of over 90% were then carbonized and converted to carbon nanofibers. The carbonization process, carried out at temperatures $>$ 1000°C, converts the stabilized PAN nanofiber into carbon nanofiber with the crystalline regions of the nanofiber transforming to turbostratic regions, through in-plane bonds being formed between adjacent, aligned molecular chains. The turbostratic domains are dispersed in an amorphous matrix with the entire structure forming the carbon nanofiber. The carbon nanofibers formed by this method were imaged using Transmission Electron Microscopy (TEM) to visually analyze the amount and alignment of turbostratic particles in an amorphous matrix. Diffraction patterns using the TEM were employed to quantify the alignment in the hot drawn CNFs as compared to the reference specimen (1x). The results indicated an improvement in turbostratic domain alignment with an improvement in the chain alignment of the precursors.

The CNFs fabricated as in Chapters 2 and 3 were tested to find the correlation between their mechanical properties and turbostratic domain alignment. For the purpose of tensile testing of single CNF, a MEMS device was used and the test was carried out under an optical microscope. Microscopy images taken during the test were analyzed using Digital Image Correlation (DIC) technique. In this study, in addition to the test cases of 1x, 2x and 4x, an additional case of 1xU was also tested. 1xU is the as-spun nanofiber ribbon i.e. not hot drawn, considered to be the case with highest randomness of the chain molecular orientation. In this case, the molecular alignment that was obtained from electrospinning was erased by the free stabilization of the nanofiber ribbon, i.e. no constraints were applied on the ribbon ends and the ribbon was allowed to shrink freely, thus randomizing the molecular chains. From the tests, a 137% improvement was observed in the Young's modulus, 190% in the tensile strength and 30% in the strain to failure.

In addition to the tensile properties, a discussion on the possible causes of failure initiation were also discussed. SEM images showed the elongation, reduction or even elimination of surface pores on the surface of the CNFs whose precursor fibers had been hot drawn. It was realized that the annealing process that takes place during drawing of nanofibers permits some of the trapped gases to escape before the highly exothermic stabilization stage that follows hot drawing.

At present, the carbon fiber industry manufactures carbon fibers for commercial purposes such as aerospace applications. The carbon fibers available are approximately 5-10μm in diameter, and made from a precursor of co-polymer PAN. Carbon fibers are divided into high strength and high modulus categories. According to properties published by a leading carbon fiber manufacturer, Toray, the highest strength, standard modulus T700S carbon fibers with diameter of 7μm have tensile strength of 4.9GPa and a Young's modulus of 230GPa. These fibers are sized and spooled to prevent damage and allow ease of handling. In some cases of reported fiber properties, the published values are of sized fibers.

The properties presented in this research work are of nanofibers fabricated from homopolymer PAN, and the fibers are tested in their ‘raw’ form. That means, no sizing or post processing of the CNFs has been carried out. Using this basic approach, this research has presented improvement in mechanical strength and modulus of the CNFs that has arisen purely due to the hot drawing process on the precursor nanofibers. The maximum strength of the tested nanofibers was 5.4 GPa, and maximum modulus 287 GPa. It is of vital importance to realize that these tests were carried out on pure, unaltered CNFs. In addition, these nanofibers were fabricated using the minimum carbonization temperature required for their conversion to carbon form. According to work published in literature, the maximum tensile strength of carbon nanofibers is obtained at carbonization temperatures of 1400°C [68], and the modulus increases with increase in carbonization temperatures, with higher temperatures converting turbostratic domains to graphitic domains at temperatures higher than 2000°C.

In order to analyze the failure mechanisms of the nanofibers used in this study, a simplified continuum 2D linear model was developed in ABAQUS based on the microstructure of the CNFs imaged in TEM. Failure was assumed to initiate in the amorphous regions at the boundary between the turbostratic matrix and the amorphous domains, based on failure stress theory. Effect of orientation of turbostratic particles with respect to fiber axis and proximity of particles on stress concentrations were discussed. This model provided further insight the effect of hot drawing on the tensile strength and Young’s modulus of carbon nanofibers.

6.2 Future Directions

Through the discussions in the chapters and the summary presented above, a few immediate directions of the work in this thesis are presented below. They include fabrication of smaller diameter nanofibers, addition of CNTs to enhance graphitic templating, use of copolymers of PAN and reduction of surface defects. These three directions have been proposed below for future work.

6.2.1 Use of Copolymers

Polyacrylonitrile molecule consists of $C \equiv N$ bonds, giving rise to strong dipole-dipole interactions in the molecule. These interactions between the positive and negative charges of the molecule limit the ability of PAN to stretch. In the research presented here, heat is used to enhance chain mobility and permit stretching of PAN. In industry however, often comonomers are added to PAN to reduce the interactions between the nitrile groups.

Apart from the interaction of the nitrile groups, comonomers are beneficial to overcome another difficulty in the use of PAN precursor. The initial oxidation of PAN involves sudden and rapid evolution of heat. This rapid exothermic process cannot be controlled easily. The initial oxidation of PAN also occurs at high initiation temperature. Sudden evolution of heat can cause chain scission during the conversion of PAN to cyclized PAN. Also due to the sudden evolution of heat, the fiber experiences a thermal shock. This can lead to poor thermal properties in the fiber. Commercial carbon fiber is rarely made of homopolymer PAN. Industrially, the comonomers used with PAN precursors are acrylic acid, methacrylic acid, itaconic acid, ethyl acrylate, and various other vinyl esters and vinyl amides. Studies have found that the comonomers are effective in the order: itaconic acid >methacrylic acid >acrylic acid >acrylamide [161]. Itaconic acid contains two carboxylic acid groups. The chance that a carboxylic acid group would react with a nitrile group is higher since if one carboxylic acid group was to move away, due to the dipole-dipole moment in the nitrile groups, another carboxylic acid group would move in the vicinity of the nitrile group. This chemical reaction would weaken the nitrile bonds and aid the cyclization process [162, 163].

The addition of comonomers reduces the initiation temperature of the cyclization process, as in Figure 6.1. The figure shows, qualitatively, the effect of comonomers on stabilization. The acidic comonomers increase the spinnability of the solution, enhance chain mobility, improve solubility of the polymer and alter fiber morphology. During heat treatment, effects of comonomers can be realized in lowering the glass transition temperature and lowering the initiation of the cyclization process. As a result, the stabilization process is more controlled, which permits cyclization of a higher proportion of PAN molecules and allows better molecular orientation.

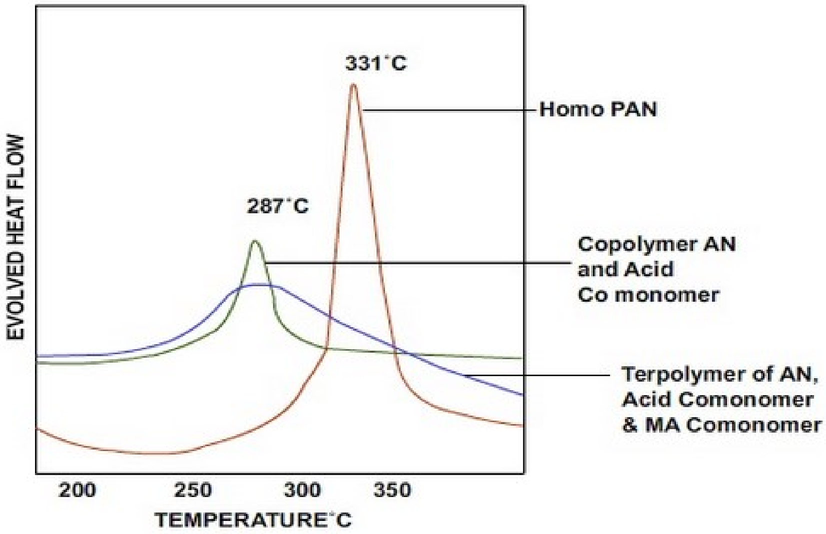

Figure 6.1: Effect of comonomers on structure stabilization [32]

6.2.2 Controlling Surface Defects

As seen in the previous chapters, while carbon nanofibers are able to achieve excellent modulus improvements through processes like hot drawing and carbonization temperatures, additional processing must be carried out to improve their surface by removal of irregularities and defects in order to improve the fiber strength.

Research by Ko et. al [164] on the influence of pre-carbonization on tensile strength of the fibers studied pre-carbonization at temperatures of 500°C, 550°C and 600°C. The results showed that the pre-carbonization treatment on the stabilized PAN fibers had a noticeable effect on the carbon fibers formed. The tensile strength of the fibers increased initially for treatment at all temperatures, but decreased rapidly thereafter. Fiber failure occurs at location of flaws either on the fiber surface or internally. It was found that during the air oxidation, the oxygen caused removal of surface structures and formed pits on the surface. The basal planes and imperfections in the basal planes were attacked by the oxygen. These disordered structures were removed by the oxygen, leaving behind a more ordered structure. This leads to improvement in modulus of the carbon fibers. In addition, because of removal of the disordered structures on the surface, failure initiation sites are reduced, leading to fibers with higher tensile strength.

Another commonly used method of surface treatment is the treatment by HNO_3. Bahl et. al. [165] compared surface treatment of carbon fibers by HNO_3 and air. Their findings showed an improvement of tensile strength of the fibers by 50%-60% irrespective of the method used. The surface treatment smoothens the surface of the fiber by etching away the outer layer which has pits and surface irregularities. This causes an increase in the strength of the fiber. After the removal of the surface, it starts to etch the lower surface, which is comparatively better ordered than the outer layer. Since HNO_3 is a stronger reactant than oxygen, this stage was observed at a faster time than in air oxidation. In air oxidation, the main reactions took place at the surface slowly etching away the irregularities. After prolonged treatment in both conditions, surface functional groups are introduced on the surface of the fiber.

The surface functionalization such as acid treatment is mainly done to enhance the fiber-matrix interactions. However, they also eliminate surface defects of carbon fibers, which leads to significant improvements in strength. CNFs have 10-100 times more surface for a given volume. As such, their surface defects are very important to be studied and eliminated.

6.2.3 Addition of Carbon Nanotubes (CNT's)

A common method to induce graphitic alignment in carbon nanofibers is by embedding carbon nanotubes in the polymer nanofiber during the electrospinning process, thus creating PAN/CNT composite nanofibers. The studies thus far have concentrated their efforts on the improvement in quantity of turbostratic/graphitic domains forming around the CNTs, or on the use of nanotubes as seeding point for creation of turbostratic domains in the fiber core [65, 66]. The addition of CNTs in the nanofiber creates seeding sites for the formation of graphitic domains around the CNT, by aligning the molecular chains of PAN along the surface of the CNT during the electrospinning process. During the spinning, the CNTs attain partial alignment along the direction of fiber axis, thus creating partially aligned graphitic domains in their subsequent nanofibers. The purpose of using CNTs to induce graphitic domains in the core of the nanofiber and to obtain a homogeneous dispersion of domains across the nanofiber cross section, as opposed to the traditional sheath-core structure seen in which the core consists mainly of amorphous or misaligned graphitic domains. Prilutsky et. al. [65] showed that an increase in the volume fraction of CNTs led to an increase in the graphitic domains in the carbon nanofiber. Papkov et. al. [67] showed that the addition of a small amount of CNTs improved the graphitic structure and crystal orientation dramatically in CNFs. Their study revealed an interesting analysis showing that the templating effect observed with the incorporation of 1.2wt% DWNTs, was at par with that obtained at carbonization temperatures of 1850°C of pristine PAN nanofibers.

Addition of CNTs to PAN nanofibers in the fabrication stage (i.e during electrospinning) have been done by a number of authors as seen above. However, combining the effects of CNT addition with the benefits of hot drawing is an area that no one has attempted to date. Research carried out by Jizhe et. al [166] on mechanical properties of PAN nanofiber ribbons embedded with CNTs showed $\approx$400% improvement in the tensile strength and Young's modulus of the nanofiber ribbons. This shows immense potential for conversion to high strength and modulus CNT-embedded carbon nanofibers, obtaining properties not seen to date.

The work here presents itself as a stepping stage for future modifications to be implemented in the fibers to obtain CNFs without skin-core structures providing extraordinary properties of CNFs.

REFERENCES

[1] T. Kowalewski, E. Kim, J. McGann, and K. Matyjaszewski, "Procedures for development of specific capacitance in carbon structures," August 2012. US Patent App. 13/390,470.

[2] C. W. LeMaistre and R. J. Diefendorf, "The origin of structure in carbonized pan fibres," *Composites*, vol. 5, no. 1, p. 45, 1974.

[3] R. H. Knibbs, "The use of polarized light microscopy in examining the structure of carbon fibres," *Journal of Microscopy*, vol. 94, no. 3, pp. 273–281, 1971.

[4] F. Barnet and M. Norr, "A three-dimensional structural model for a high modulus pan-based carbon fibre," *Composites*, vol. 7, no. 2, pp. 93 – 99, 1976.

[5] S. C. Bennett, D. J. Johnson, and W. Johnson, "Strength-structure relationships in pan-based carbon fibres," *Journal of Materials Science*, vol. 18, no. 11, pp. 3337–3347, 1983.

[6] R. Perret and W. Ruland, "The microstructure of PAN-base carbon fibres," *Journal of Applied Crystallography*, vol. 3, pp. 525–532, Dec 1970.

[7] R. J. Diefendorf and E. Tokarsky, "High-performance carbon fibers," *Polymer Engineering and Science*, vol. 15, no. 3, pp. 150–159, 1975.

[8] S. Bennett and D. Johnson, "Electron-microscope studies of structural heterogeneity in pan-based carbon fibres," *Carbon*, vol. 17, no. 1, pp. 25 – 39, 1979.

[9] J. Liu, Z. Yue, and H. Fong, "Continuous nanoscale carbon fibers with superior mechanical strength," *Small*, vol. 47, pp. 536–542, 2009.

[10] T. Tagawa and T. Miyata, "Size effect on tensile strength of carbon fibers," *Materials Science and Engineering: A*, vol. 238, no. 2, pp. 336 – 342, 1997.

[11] D. J. Johnson, "Structure-property relationships in carbon fibres," *Journal of*

Physics D: Applied Physics, vol. 20, no. 3, p. 286, 1987.

[12] H. Wang, Y. Wang, T. Li, S. Wu, and L. Xu, "Gradient distribution of radial structure of pan-based carbon fiber treated by high temperature," *Progress in Natural Science: Materials International*, vol. 24, no. 1, pp. 31–34, 2014.

[13] C. M. Haslauer, A. K. Moghe, J. A. Osborne, B. S. Gupta, and E. G. Loboa, "Collagenpcl sheathcore bicomponent electrospun scaffolds increase osteogenic differentiation and calcium accretion of human adipose-derived stem cells," *Journal of Biomaterials Science, Polymer Edition*, vol. 22, no. 13, pp. 1695–1712, 2011.

[14] W. E. Teo, "Introduction to electrospinning parameters and fiber control," *Electrospin Tech*, pp. 7–9, 9 March 2015.

[15] D. Li, Y. Wang, and Y. Xia, "Electrospinning nanofibers as uniaxially aligned arrays and layer-by-layer stacked films," *Advanced materials*, vol. 16, no. 4, pp. 361–366, 2004.

[16] P. Katta, M. Alessandro, R. D. Ramsier, , and G. G. Chase, "Continuous electrospinning of aligned polymer nanofibers onto a wire drum collector," *Nano Letters*, vol. 4, no. 11, pp. 2215–2218, 2004.

[17] E. Zussman, X. Chen, W. Ding, L. Calabri, D. Dikin, J. Quintana, and R. Ruoffs, "Mechanical and structural characterization of electrospun pan-derived carbon nanofibers," *Carbon*, vol. 49, pp. 1710–1719, 2011.

[18] M. Richard-Lacroix and C. Pellerin, "Orientation and partial disentanglement in individual electrospun fibers: Diameter dependence and correlation with mechanical properties," *Macromolecules*, vol. 48, no. 13, pp. 4511–4519, 2015.

[19] S. Moon and R. J. Farris, "Strong electrospun nanometer-diameter polyacrylonitrile carbon fiber yarns," *Carbon*, vol. 47, no. 12, pp. 2829 – 2839, 2009.

[20] H. Kobayashi, K. Sasaguri, Y. Fujisaki, and T. Amano, "Effect of molecular weight and its distribution on stretching of polyacrylonitrile gel," *Journal of Polymer Sci-*

ence Part A: General Papers, vol. 2, no. 1, pp. 313–331, 1964.

[21] K. Yang, S. Lee, H. Chae, and D. Lee, "Method for preparing polyacrylonitrile-based polymer for preparation of carbon fiber using microwave and method for preparing carbon fiber using the same." `https://www.google.com/patents/US20120288434`, November 2012. US Patent App. 13/461,241.

[22] K. B. Wiles, "Determination of reactivity ratios for acrylonitrile/methyl acrylate radical copolymerizatioin via nonlinear methodologies using real time ftir," 2002.

[23] C. David and J. Rabek, *Comprehensive chemical kinetics*. No. 14 in Comprehensive Chemical Kinetics, Elsevier Pub. Co., 1975.

[24] L. Manocha and O. Bahl, "Role of oxygen during thermal stabilisation of pan fibres," *Fibre Science and Technology*, vol. 13, no. 3, pp. 199 – 212, 1980.

[25] W. Watt, *Strong Fiber*, vol. 1. Elsevier Science Publishers, 1985.

[26] Cryolife, "On - x pyrolytic carbon," 2007.

[27] E. Fitzer, W. Frohs, and M. Heine, "Optimization of stabilization and carbonization treatment of pan fibres and structural characterization of the resulting carbon fibres," *Carbon*, vol. 24, no. 4, pp. 387–395, 1986.

[28] O. Bahl and L. Manocha, "Characterization of oxidised pan fibres," *Carbon*, vol. 12, no. 4, pp. 417–423, 1974.

[29] M. Sliwinska-Bartkowiak, H. Drozdowski, M. Kempinski, M. Jazdzewska, Y. Long, J. C. Palmer, and K. E. Gubbins, "Structural analysis of water and carbon tetrachloride adsorbed in activated carbon fibres," *Physical Chemistry Chemical Physics*, vol. 14, pp. 7145–7153, 2012.

[30] S. N. Arshad, M. Naraghi, and I. Chasiotis, "Strong carbon nanofibers from electrospun polyacrylonitrile," *Carbon*, vol. 49, pp. 1710–1719, 2011.

[31] Y. Xue, J. Liu, and J. Liang, "Correlative study of critical reactions in polyacrylonitrile based carbon fiber precursors during thermal-oxidative stabilization," *Polymer*

Degradation and Stability, vol. 98, no. 1, pp. 219 – 229, 2013.

[32] N. Grassie and M. Zulfiqar, *Developments in Polymer Stabilization*, vol. 1. 1979.

[33] S. Ramakrishna, K. Fujihara, W.-E. Teo, T.-C. Lim, and Z. Ma, *An Introduction to Electrospinning and Nanofibers*. World Scientific Publishing Company, 2012.

[34] J. B. Donnet, T. K. Wang, J. M. Peng, and S. Rebouilla, *Carbon Fibers*. Marcel Dekker, 3rd edition ed., 1998.

[35] J. G. Morley, *High Performance Fiber Composites*. Academic Press, 1987.

[36] W.-X. Zhang, Y.-Z. Wang, and C.-F. Sun, "Characterization on oxidative stabilization of polyacrylonitrile nanofibers prepared by electrospinning," *Journal of Polymer Research*, vol. 14, no. 6, pp. 467–474, 2007.

[37] X.H.Qin, "Structure and property of electrospinning pan nanofibers by different preoxidation temperature," *Journal of Thermal Analysis and Calorimetry*, vol. 99-2, pp. 571–575, 2010.

[38] M. Wu and Q. Wang, "Optimization of stabilization conditions for electrospun polyacrylonitrile nanofibers," *Polymer Degradation and Stability*, vol. 97-8, pp. 1511–1519, 2012.

[39] T. Ko, "Raman spectrum of modified pan-based carbon fibers during graphitization," *Journal of Applied Polymer Science*, vol. 59, no. 4, pp. 577–580, 1996.

[40] M. Yu, O. Lourie, M. Dyer, K. Moloni, T. Kelly, and R. Ruoff, "Strength and breaking mechanism of multiwalled carbon nanotubes under tensile load," *Science*, vol. 287, pp. 637–640, 2000.

[41] C. Lee, X. Wei, J. Kysar, and H. J, "Measurement of the elastic properties and intrinsic strength of monolayer graphene," *Science*, vol. 321, pp. 385–388, 2008.

[42] "Toray carbon fibers, data sheet, t1000g." `http://www.toraycfa.com/pdfs/T1000GDataSheet.pdf`.

[43] B. Peng, M. Locascio, P. Zapol, S. Li, G. S. S. Mielke, and H. Espinosa, "Measure-

ments of near-ultimate strength for multiwalled carbon nanotubes and irradiation-induced crosslinking improvements," *Nature Nanotechnology*, vol. 3, pp. 626–631, 2008.

[44] T. Ichikawa, T. Ochi, A. Kishiro, Y. Kato, T. Shibata, and M. Ise, "Polyacrylonitrile fiber manufacturing method and carbon fiber manufacturing method." `https://www.google.com/patents/US20130264733`, October 2013. US Patent App. 13/990,540.

[45] R. Mathur, D. Gupta, O. Bahl, and T. Dhami, "Infrared spectral studies of preoxidized pan fibres incorporated with cuprous chloride additive," *Fibre Science and Technology*, vol. 20, no. 3, pp. 227 – 234, 1984.

[46] J. Chen and I. Harrison, "Modification of polyacrylonitrile (pan) carbon fiber precursor via post-spinning plasticization and stretching in dimethyl formamide (dmf)," *Carbon*, vol. 40, no. 1, pp. 25 – 45, 2002.

[47] T. Kobashi and S. Takao, "Polyacrylonitrile fiber with high strength and high modulus of elasticity." `https://www.google.com/patents/US4658004`, April 1987. US Patent 4,658,004.

[48] J. Paul, "Method of manufacturing carbon fiber using preliminary stretch." `https://www.google.com/patents/CA1327258C?cl=en`, March 1994. CA Patent 1,327,258.

[49] E. A. Morris, M. C. Weisenberger, S. B. Bradley, M. G. Abdallah, S. J. Mecham, P. Pisipati, and J. E. McGrath, "Synthesis, spinning, and properties of very high molecular weight poly(acrylonitrile-co-methyl acrylate) for high performance precursors for carbon fiber," *Polymer*, vol. 55, no. 25, pp. 6471 – 6482, 2014.

[50] W. Watt and W. Johnson, "The effect of length changes during the oxidation of polyacrylonitrile fibers on the young's modulus of carbon fibers," *Applied Polymer Symposium*, vol. 9, pp. 215–227, 1969.

[51] D. J. Johnson and C. N. Tyson, “The fine structure of graphitized fibres,” *Journal of Physics D: Applied Physics*, vol. 2, no. 6, p. 787, 1969.

[52] W. Johnson and W. Watt, “Structure of high modulus carbon fibers,” *Nature*, vol. 215, pp. 384–386, 1967.

[53] D. V. Badami, J. C. Joiner, and G. A. Jones, “The microstructure of intercalated graphite fibers,” *Nature*, vol. 215, pp. 386–387, 1967.

[54] P. Kwizera, M. Dresselhaus, D. Uhlmann, J. Perkins, and C. Desper, “The microstructure of intercalated graphite fibers,” *Carbon*, vol. 20, no. 5, pp. 387–394, 1982.

[55] J. A. Hugo, V. A. Phillips, and B. W. Roberts, “The microstructure of intercalated graphite fibers,” *Nature*, vol. 226, p. 144, 1970.

[56] M. Yu, Y. Xu, C. Wang, X. Hu, B. Zhe, K. Qiao, and H. Yuan, “Heredity and difference of multiple-scale microstructures in pan-based carbon fibers and their precursor fibers,” *Journal of Applied Polymer Science*, vol. 125, pp. 3159–3166, 2012.

[57] B. J. Wicks and R. A. Coyle, “Microstructural inhomogeneity in carbon-fibers,” *Journal of Material Science*, vol. 11, pp. 376–383, 1976.

[58] LeMaistre and Diefendorf p. 77, 1972.

[59] J. A. Griffoths and H. Marsh p. 316, Extended Abstracts of the 12th Biennial Conference on Carbon, 1981.

[60] J. Johnson, W. Watt, L. N. Phillips, and R. Moreton, “Improvements in or relating to carbonisable fibre and carbon fibre and their production,”

[61] X. Huang, “Fabrication and properties of carbon fibers,” *Materials*, vol. 2, no. 4, pp. 2369–2403, 2009.

[62] B. Saha and G. C. Schatz, “Carbonization in polyacrylonitrile (pan) based carbon fibers studied by reaxff molecular dynamics simulations,” *Journal of Physical*

Chemistry, vol. 116, no. 15, p. 46844692, 2012.

[63] M. Naraghi, T. Ozkan, I. Chasiotis, S. S. Hazra, and M. P. D. Boer, "Mems platform for on-chip nanomechanical experiments with strong and highly ductile nanofibers," *Journal of Micromechanics and Microengineering*, vol. 20, no. 12, 2010.

[64] E. Penev, V. Artyukhov, and B. Yakobson, "Basic structural units in carbon fibers: Atomistic models and tensile behavior," *Carbon*, vol. 85, pp. 72–78, 2015.

[65] S. Prilutsky, E. Zussman, and Y. Cohen, "The effect of embedded carbon nanotubes on the morphological evolution during the carbonization of poly(acrylonitrile) nanofibers," *Nanotechnology*, vol. 19, no. 16, p. 165603, 2008.

[66] S. Prilutsky, E. Zussman, and Y. Cohen, "Carbonization of electrospun poly(acrylonitrile) nanofibers containing multiwalled carbon nanotubes observed by transmission electron microscope with in situ heating," *Journal of Polymer Science Part B: Polymer Physics*, vol. 48, no. 20, pp. 2121–2128, 2010.

[67] D. Papkov, A. M. Beese, A. Goponenko, Y. Zou, M. Naraghi, H. D. Espinosa, B. Saha, G. C. Schatz, A. Moravsky, R. Loutfy, S. T. Nguyen, and Y. Dzenis, "Extraordinary improvement of the graphitic structure of continuous carbon nanofibers templated with double wall carbon nanotubes," *ACS Nano*, vol. 7, no. 1, pp. 126–142, 2013.

[68] S. N. Arshad, "High strength carbon nanofibers derived from electrospun polyacrylonitrile," *University of Illinois at Urbana-Champaign*, 2010.

[69] S. Aldrich. `http://www.sigmaaldrich.com/materials-science/material-science-products.html?TablePage=16376687`.

[70] M. Gagliardi, "Global market and technologies for nanofibers," tech. rep., BCC Research, Market Forecasting, May 2013.

[71] W. J. Li, C. T. Laurencin, E. J. Caterson, R. S. Tuan, and F. K. Ko, "Electrospun nanofibrous structure: A novel scaffold for tissue engineering," *Journal of Biomed-*

ical Materials Research, vol. 60, no. 4, pp. 613–621, 2002.

[72] X. Wang, C. Drew, S.-H. Lee, K. J. Senecal, J. Kumar, , and L. A. Samuelson, "Electrospun nanofibrous membranes for highly sensitive optical sensors," *Nano Letters*, vol. 2, no. 11, pp. 1273–1275, 2002.

[73] L. Nair, S. Bhattacharyya, J. D. Bender, Y. E. Greish, P. W. Brown, H. R. Allcock, and C. T. Laurencin, "Fabrication and optimization of methylphenoxy substituted polyphosphazene nanofibers for biomedical applications," *Biomacromolecules*, vol. 5, no. 6, pp. 2212–2220, 2004.

[74] X. H. Qin and S. Y. Wang, "Filtration properties of electrospinning nanofibers," *Journal of Applied Polymer Science*, vol. 102, no. 2, pp. 1285–1290, 2006.

[75] K. M. Yun, C. J. H. Jr., Y. Matsubayashi, M. Kawabe, F. Iskandar, and K. Okuyama, "Nanoparticle filtration by electrospun polymer fibers," *Chemical Engineering Science*, vol. 62, no. 17, pp. 4751 – 4759, 2007.

[76] A. Luzio, E. V. Canesi, C. Bertarelli, and M. Caironi, "Electrospun polymer fibers for electronic applications," *Materials*, vol. 7, no. 2, pp. 906–947, 2014.

[77] L. Zhang, A. Aboagye, A. Kelkar, C. Lai, and H. Fong, "A review: carbon nanofibers from electrospun polyacrylonitrile and their applications," *Journal of Materials Science*, vol. 49, no. 2, pp. 463–480, 2014.

[78] C. Kim and K. S. Yang, "Electrochemical properties of carbon nanofiber web as an electrode for supercapacitor prepared by electrospinning," *Applied Physics Letters*, vol. 83, no. 6, pp. 1216–1218, 2003.

[79] D. Li and Y. Xia, "Electrospinning of nanofibers: Reinventing the wheel?," *Advanced Materials*, vol. 16, no. 14, pp. 1151–1170, 2004.

[80] F. Béguin, K. Szostak, G. Lota, and E. Frackowiak, "A self-supporting electrode for supercapacitors prepared by one-step pyrolysis of carbon nanotube/polyacrylonitrile blends," *Advanced Materials*, vol. 17, no. 19, pp. 2380–

2384, 2005.

[81] S. H. Park, C. Kim, Y. I. Jeong, D. Y. Lim, Y. E. Lee, and K. S. Yang, "Activation behaviors of isotropic pitch-based carbon fibers from electrospinning and meltspinning," *Synthetic Metals*, vol. 146, no. 2, pp. 207 – 212, 2004.

[82] C. Boys, "On the production, properties, and some suggested uses of the finest threads," *Proceedings of the Physical Society*, vol. 9, pp. 8–19, 1887.

[83] J. F. Cooley, "Improved methods of and apparatus for electrically separating the relatively volatile liquid component from the component of relatively fixed substances of composite fluids," 1900.

[84] J. Cooley, "Apparatus for electrically dispersing fluids." `http://www.google.com/patents/US692631`, 1902. US Patent 692,631.

[85] J. Cooley, "Electrical method of dispersing fluids." `http://www.google.com/patents/US745276`, 1903. US Patent 745,276.

[86] F. Anton, "Process and apparatus for preparing artificial threads," 1934. US Patent 1,975,504.

[87] F. Anton, "Method and apparatus for spinning," 1944. US Patent 2,349,950.

[88] S. Theron, E. Zussman, and A. Yarin, "Experimental investigation of the governing parameters in the electrospinning of polymer solutions," *Polymer*, vol. 45, no. 6, pp. 2017–2030, 2004.

[89] A. L. Yarin, S. Koombhongse, and D. H. Reneker, "Bending instability in electrospinning of nanofibers," *Journal of Applied Physics*, vol. 89, no. 5, pp. 3018–3026, 2001.

[90] I. Demir, M. M.and Yilgor, E. Yilgor, and B. Erman, "Electrospinning of polyurethane fibers," *Polymer*, vol. 43, pp. 3303–3309, 2002.

[91] T. Jarusuwannapoom, S. W. L. N. M. P. C. Hongrojjanawiwat, W.and Jitjaicham, P. Koombhongse, R. Rangkupan, and P. Supaphol, "Effect of solvents on electro-

spinnability of polystyrene solutions and morphological appearance of resulting electrospun polystyrene fibers," *European Polymer Journal*, vol. 41, pp. 409–421, 2005.

[92] S. H. Lee, C. Tekmen, and W. M. Sigmund, "Three-point bending of electrospun tio2 nanofibers," *Materials Science and Engineering: A*, vol. 398, no. 12, pp. 77 – 81, 2005.

[93] J. Deitzel, S. T. N. Kosik, W.and McKnight, J. DeSimone, and S. Crette, "Electrospinning of polymer nanofibers with specific surface chemistry," *Polymer*, vol. 43, pp. 1025–1029, 2002.

[94] H. Fong, I. Chun, and D. Reneker, "Beaded nanofibers formed during electrospinning," *Polymer*, vol. 40, no. 16, pp. 4585 – 4592, 1999.

[95] T. Wang and S. Kumar, "Electrospinning of polyacrylonitrile nanofibers," *Journal of Applied Polymer Science*, vol. 102, no. 2, pp. 1023–1029, 2006.

[96] C. J. Buchko, L. C. Chen, Y. Shen, and D. C. Martin, "Processing and microstructural characterization of porous biocompatible protein polymer thin films," *Polymer*, vol. 40, no. 26, pp. 7397 – 7407, 1999.

[97] J. Kameoka, R. Orth, Y. Yang, D. Czaplewski, R. Mathers, G. W. Coates, and H. G. Craighead, "A scanning tip electrospinning source for deposition of oriented nanofibres," *Nanotechnology*, vol. 14, no. 10, p. 1124, 2003.

[98] C. Mit-uppatham, M. Nithitanakul, and P. Supaphol, "Ultrafine electrospun polyamide-6 fibers: Effect of solution conditions on morphology and average fiber diameter," *Macromolecular Chemistry and Physics*, vol. 205, no. 17, pp. 2327–2338, 2004.

[99] P. K. Baumgarten, "Electrostatic spinning of acrylic microflbers," *Journal of Colloid and Interface Science*, vol. 36, pp. 75–79, 1971.

[100] S. Megelski, D. Stephens, J.S.and Chase, and J. Rabolt, "Micro- and nanostruc-

tured surface morphology on electrospun polymer fibers," *Macromolecules*, vol. 35, pp. 8456–8466, 2002.

[101] J. I. Kim, T. I. Hwang, L. E. Aguilar, C. H. Park, and C. S. Kim, "A controlled design of aligned and random nanofibers for 3d bi-functionalized nerve conduits fabricated via a novel electrospinning set-up," *Scientific Reports*, vol. 6, 2016.

[102] S. Theron, E. Zussman, and A. Yarin, "Experimental investigation of the governing parameters in the electrospinning of polymer solutions," *Polymer*, vol. 45, no. 6, pp. 2017 – 2030, 2004.

[103] R. Jaeger, H. Schönherr, and G. Vancso, "Chain packing in electro-spun poly (ethylene oxide) visualized by atomic force microscopy," *Macromolecules*, vol. 29, no. 23, pp. 7634–7636, 1996.

[104] J. Johnson, L. N. Phillips, and W. Watt, "The production of carbon fibers," no. Britain Patent 1110790, 1965.

[105] Z. Xie, H. Niu, and T. Lin, "Continuous polyacrylonitrile nanofiber yarns: preparation and dry-drawing treatment for carbon nanofiber production," *RSC Adv.*, vol. 5, pp. 15147–15153, 2015.

[106] Z. Song, X. Hou, L. Zhang, and S. Wu, "Enhancing crystallinity and orientation by hot-stretching to improve the mechanical properties of electrospun partially aligned polyacrylonitrile (pan) nanocomposites," *Materials*, vol. 4, no. 4, p. 621, 2011.

[107] S. A. Hosseini Ravandi, E. Hassanabadi, H. Tavanai, and R. A. Abuzade, "Mechanical properties and morphology of hot drawn polyacrylonitrile nanofibrous yarn," *Journal of Applied Polymer Science*, vol. 124, no. 6, pp. 5002–5009.

[108] E. Frank, F. Hermanutz, and M. R. Buchmeiser, "Carbon fibers: Precursors, manufacturing, and properties," *Macromolecular Materials and Engineering*, vol. 297, no. 6.

[109] Hou, X. Yang, L. Zhang, E. Waclawik, and S. Wu, "Stretching-induced crystallinity

and orientation to improve the mechanical properties of electrospun pan nanocomposites," *Materials & Design*, vol. 31, no. 4, pp. 1726–1730, 2010.

[110] R. D. B. Fraser, "Interpretation of infrared dichroism in fibrous proteins the 2 region," *The Journal of Chemical Physics*, vol. 24, no. 1, pp. 89–95, 1956.

[111] Z. Bashir, "A critical review of the stabilisation of polyacrylonitrile," *Carbon*, vol. 29, pp. 1081–1090.

[112] J. Liu, P. Wang, and R. Li, "Continuous carbonization of polyacrylonitrile-based oxidized fibers:aspects on mechanical properties and morphological structure," *Applied Polymer Science*, vol. 52, no. 7, pp. 945–950, 1994.

[113] J. Liu, P. Zhoua, L. Zhang, Z. Ma, J. Liang, and H. Fong, "Thermo-chemical reactions occurring during the oxidative stabilization of electrospun polyacrylonitrile precursor nanofibers and the resulting structural conversions," *Carbon*, vol. 47, pp. 1087–1095, 2009.

[114] R. Setnescu, S. Jipa, T. Setnescu, W. Kappel, S. Kobayashi, and Z. Osawa, "Ir and x-ray characterization of the ferromagnetic phase of pyrolysed polyacrylonitrile," *Carbon*, vol. 37, no. 1, pp. 1–6, 1999.

[115] P. Sànchez-Soto, M.A.Avileès, J. del Rìo, J. Ginès, J. Pascual, and J. Perèz-Rodrìguez, "Thermal study of the effect of several solvents on polymerization of acrylonitrile and their subsequent pyrolysis," *Journal of Analytical and Applied Pyrolysis*, vol. 58-59, pp. 155–172, 2001.

[116] S.C.Martin, J. Liggat, and C.E.Snape, "In-situ nmr investigation into the thermal degradation and stabilization of pan," *Polymer Degradation and Stability*, vol. 74, no. 3, pp. 407–412, 2001.

[117] D.D.Edie, "The efffect of processing on the structure and properties of carbon fiber," *Carbon*, vol. 36, no. 4, pp. 345–262, 1998.

[118] H. Ogawa and K. Saito, "Oxidation behavior of polyacrylonitrile fibers evaluated

by new stabilization index," *Carbon*, vol. 33, no. 6, pp. 783–788, 1995.

[119] A. Shindo, "Studies on graphite fiber," *Journal of the Ceramic Society of Japan, Report No. 317 of the Government Industrial Research Institute, Osaka*, vol. 69, p. 195, 1961.

[120] S. Dalton, F. Heatley, and P. M. Budd, "Thermal stabilization of polyacrylonitrile fibres," *Polymer*, vol. 40, p. 55315543, 1999.

[121] P. Rangarajan, V. Bhanu, D. Godshall, G. Wilkes, J. McGrath, and D. Baird, "Dynamic oscillatory shear properties of potentially melt processable high acrylonitrile terpolymers," *Polymer*, vol. 43, pp. 2699–2709, 2002.

[122] E. Fitzer and M. Heym, "Carbon fibres–the outlook," *Chem. Ind.*, no. 16, pp. 663–676, 1976.

[123] E. Fitzer and D. J. Muller, "Zur bildung von gewinkelten leiterpolymeren in polyacrylnitril-fasern," *Die Makromolekulare Chemie*, vol. 144, no. 1, pp. 117–133, 1971.

[124] L. Peebles, P. Peyser, A. Snow, and W. Peters, "On the exotherm of polyacrylonitrile: Pyrolysis of the homopolymer under inert conditions," *Carbon*, vol. 28, no. 5, pp. 707 – 715, 1990.

[125] N. Grassie and R. McGuchan, "Pyrolysis of polyacrylonitrile and related polymers: Vi, acrylonitrile copolymers containing carboxylic acid and amide structures," *European Polymer Journal*, vol. 8, no. 2, pp. 257–269, 1972.

[126] E. V. Thompson, "The thermal behavior of acrylonitrile polymers. i. on the decomposition of polyacrylonitrile between 250 and 325řc.," *Journal of Polymer Science Part B: Polymer Letters*, vol. 4, no. 5, pp. 361–366, 1966.

[127] J. Shurz, "Discoloration effects in acrylonitrile polymers," *Journal of Polymer Science*, vol. 28, pp. 438–439, 1958.

[128] H. N. Friedlander, L. H. P. Jr., J. Brandrup, and J. R. Kirby, "On the chromophore

of polyacrylonitrile. vi. mechanism of color formation in polyacrylonitrile," *Macromolecules*, vol. 1, no. 1, pp. 79–86, 1968.

[129] W. W. Wright, "Development in polymer degradation-1," *British Polymer Journal*, vol. 11, no. 4, p. 184, 1977.

[130] N. Grassie and R. McGuchan, "Pyrolysis of polyacrylonitrile and related polymers - ix," *European Polymer Journal*, vol. 9, no. 6, pp. 507 – 517, 1973.

[131] D. A. Grove and A. Abhiraman, "A mathematical model of solid-state thermo-oxidative stabilization of acrylic fibers," *Carbon*, vol. 30, no. 3, pp. 451 – 457, 1992.

[132] G. K. Laydex, "Tensile response of polyacrylonitrile fibers during air heating," *Journal of Applied Polymer Science*, vol. 15, no. 7, pp. 1709–1715, 1971.

[133] D. Muller, E. Fitzer, and A. K. Fiedler p. 2, Proceedings of the International Conference on Carbon Fibres, their Composites and Applications, 1971.

[134] O. Bahl and L.M.Manocha, "Surface topology and mechanical properties of carbon fibers," *Die Angewandte Makremolekulare Chemie*, vol. 75, pp. 137–152, 1979.

[135] E. Zussman, X. Chen, W. Ding, L. Calabri, D. A. Dikin, J. P. Quintana, and R. S. Ruoff, "Mechanical and structural characterization of electrospun pan-derived carbon nanofibers," *Carbon*, vol. 43, pp. 2175–2185, 8 2005.

[136] Z. Zhou, C. Lai, L. Zhang, Y. Qian, H. Hou, D. H. Reneker, and H. Fong, "Development of carbon nanofibers from aligned electrospun polyacrylonitrile nanofiber bundles and characterization of their microstructural, electrical, and mechanical properties," *Polymer*, vol. 50, no. 13, pp. 2999 – 3006, 2009.

[137] K. Saito and H. Ogawa, "Process for producing carbon fibers," no. United States Patent 4,069,297, 1978.

[138] T. Ko, "The influence of pyrolysis on physical properties and microstructure of modified pan fibers during carbonization," *Applied Polymer Science*, vol. 43, no. 3,

pp. 589–600, 1991.

[139] D. Zhu, C. Xu, N. Nakura, and M. Matsuo, "Study of carbon films from pan/vgcf composites by gelation/crystallization from solution," *Carbon*, vol. 40, pp. 363–373, 2002.

[140] L. Laffont, M. Monthioux, V. Serin, R. Mathur, C. Guimon, and M. Guimon, "An eels study of the structural and chemical transformation of {PAN} polymer to solid carbon," *Carbon*, vol. 42, no. 1213, pp. 2485 – 2494, 2004.

[141] W. Watt, "Pyrolysis of polyacrylonitrile," *Nature*, vol. 222, p. 265, 1969.

[142] T.-H. Ko, S.-C. Liau, and M.-F. Lin, "Preparation of graphite fibres from a modified pan precursor," *Journal of Materials Science*, vol. 27, no. 22, pp. 6071–6078, 1992.

[143] J. Rafique, J. Yu, X. Zha, and K. Rafique, "Fabrication of ultra thin and aligned carbon nanofibres from electrospun polyacrylonitrile nanofibres," *Bulletin of Materials Science*, vol. 33, no. 5, pp. 553–559, 2010.

[144] K. Molnár, B. Szolnoki, A. Toldy, and L. M. Vas, "Thermochemical stabilization and analysis of continuously electrospun nanofibers," *Journal of Thermal Analysis and Calorimetry*, vol. 117, no. 3, pp. 1123–1135, 2014.

[145] Y. Liu, "Stabilization and carbonization studies of polyacrylonitrile/carbon nanotube composite fibers," 2010.

[146] B. A. Newcomb, P. V. Gulgunje, K. Gupta, M. G. Kamath, Y. Liu, L. A. Giannuzzi, H. G. Chae, and S. Kumar, "Processing, structure, and properties of gel spun pan and pan/cnt fibers and gel spun pan based carbon fibers," *Polymer Engineering & Science*, vol. 55, no. 11.

[147] K. Sahin, N. A. Fasanella, I. Chasiotis, K. M. Lyons, B. A. Newcomb, M. G. Kamath, H. G. Chae, and S. Kumar, "High strength micron size carbon fibers from polyacrylonitrile-carbon nanotube precursors," *Carbon*, vol. 77, pp. 442–453, 2014.

[148] C. R. Houska and B. E. Warren, "X-ray study of the graphitization of carbon black,"

Journal of Applied Physics, vol. 25, no. 12, 1954.

[149] E. Tan and C. Lim, “Mechanical characterization of nanofibers a review,” *Composites Science and Technology*, vol. 66, no. 9, pp. 1102 – 1111, 2006.

[150] E. Zussman, M. Burman, A. L. Yarin, R. Khalfin, and Y. Cohen, “Tensile deformation of electrospun nylon-6,6 nanofibers,” *Journal of Polymer Science Part B: Polymer Physics*, vol. 44, no. 10, pp. 1482–1489, 2006.

[151] J. Lee and Y. Deng, “Nanoindentation study of individual cellulose nanowhisker-reinforced pva electrospun fiber,” *Polymer Bulletin*, vol. 70, no. 4, pp. 1205–1219, 2013.

[152] F. Ko, Y. Gogotsi, A. Ali, N. Naguib, H. Ye, G. Yang, C. Li, and P. Willis, “Electrospinning of continuous carbon nanotube-filled nanofiber yarns,” *Advanced Materials*, vol. 15, no. 14, pp. 1161–1165, 2003.

[153] Y. Zhu, N. Moldovan, and H. D. Espinosa, “A microelectromechanical load sensor for in situ electron and x-ray microscopy tensile testing of nanostructures,” *Applied Physics Letters*, vol. 86, no. 1, 2005.

[154] B. A. Samuel, M. A. Haque, B. Yi, R. Rajagopalan, and H. C. Foley, “Mechanical testing of pyrolysed poly-furfuryl alcohol nanofibres,” *Nanotechnology*, vol. 18, no. 11, p. 115704, 2007.

[155] S. Lu, Z. Guo, W. Ding, and R. S. Ruoff, “Analysis of a microelectromechanical system testing stage for tensile loading of nanostructures,” *Review of Scientific Instruments*, vol. 77, no. 5, 2006.

[156] E. Zussman, M. Burman, A. L. Yarin, R. Khalfin, and Y. Cohen, “Tensile deformation of electrospun nylon-6,6 nanofibers,” *Journal of Polymer Science Part B: Polymer Physics*, vol. 44, no. 10, pp. 1482–1489, 2006.

[157] G. Vendroux and W. G. Knauss, “Submicron deformation field measurements: Part 2. improved digital image correlation,” *Experimental Mechanics*, vol. 38, no. 2,

pp. 86–92, 1998.

[158] J. Cai and M. Naraghi, “Computational analysis of electrical conduction in hybrid nanomaterials with embedded non-penetrating conductive particles,” *Modelling and Simulation in Materials Science and Engineering*, vol. 24, no. 6, p. 065004, 2016.

[159] A. M. Ito, A. Takayama, Y. Oda, and H. Nakamura, “The first principle calculation of bulk modulus and young’s modulus for amorphous carbon material,” *Journal of Physics: Conference Series*, vol. 518, no. 1, p. 012011, 2014.

[160] J. Cho, J. Luo, and I. Daniel, “Mechanical characterization of graphite/epoxy nanocomposites by multi-scale analysis,” *Composites Science and Technology*, vol. 67, no. 1112, pp. 2399 – 2407, 2007.

[161] N. Grassie and R. McGuchan, “Pyrolysis of polyacrylonitrile and related polymers:vi, acrylonitrile copolymers containing carboxylic acid and amide structures,” *European Polymer Journal*, vol. 8, no. 2, pp. 257 – 269, 1972.

[162] A. K. Gupta, D. K. Paliwal, and P. Bajaj, “Acrylic precursors for carbon fibers,” *Journal of Macromolecular Science, Part C*, vol. 31, no. 1, pp. 1–89, 1991.

[163] R. Devasia, C. R. Nair, and K. Ninan, “Copolymerization of acrylonitrile with itaconic acid in dimethylformamide: effect of triethylamine,” *European Polymer Journal*, vol. 39, no. 3, pp. 537 – 544, 2003.

[164] T. Ko and C. Li, “The influence of pre-carbonization on the properties of pan-based carbon fibers developed by two-stage carbonization and air oxidation,” *Polymer Composites*, vol. 16, no. 3, pp. 224–232, 1995.

[165] O. P. Bahl, R. B. Mathur, and T. L. Dhami, “Effects of surface treatment on the mechanical properties of carbon fibers,” *Polymer Engineering & Science*, vol. 24, no. 7, pp. 455–459, 1984.

[166] J. Cai, S. Chawla, and M. Naraghi, “Microstructural evolution and mechanics of hot-drawn cnt-reinforced polymeric nanofibers,” *Carbon*, vol. 109, pp. 813–822,

2016.